NOTE TO USERS

NANOTRIBOLOGICAL CHARACTERIZATION OF DYNAMIC SURFACES

A

DISSERTATION

Presented to the Faculty

of the University of Alaska Fairbanks

in Partial Fulfillment of the Requirements

for the Degree of

DOCTOR OF PHILOSOPHY

By

Sudeep Prabhakar Ingole, M.E.

Fairbanks, Alaska

May 2005

NANOTRIBOLOGICAL CHARACTERIZATION OF DYNAMIC SURFACES

By

Sudeep Prabhakar Ingole

RECOMMENDED:

Advisory Committee Chair

Chair, Department of Mechanical Engineering

APPROVED:

Dean, College of Engineering and Mines

Dean of the Graduate School

May 6, 2005

Date

Abstract

This dissertation research includes three fundamental areas: utilizing an atomic force microscope (AFM) to study the nanomechanical and tribological properties, to understand friction and wear at nanometer length, and to study wear mechanisms of boride coatings for biological applications.

This was the first time that an AFM was used to study the nanomechanical and tribological properties and the performance of the materials. The AFM enables detailed investigation of the wear modes at multi-length scales as well as the surface mechanical properties. Surface analysis using an AFM included the surface texture, profile of indents, wear tracks, and wear scars. The friction force microscope (FFM) revealed the relationship between surface texture and frictional properties, thus contributing to the fundamental understanding of nanotribology. A new wear model was proposed. Also, hardening was discovered under the indents.

The multi-scale wear study was focused on fundamental wear mechanisms. New wear modes, different than the traditional ones, were proposed. In this research, nano-cracks and other damage (hardening and plastic flow) were found at different scales.

Boride coatings on refractory metals were investigated for biological applications. Tribological performance of these coatings was studied in dry and wet (biofluid) conditions. It was found that boron plays an important role in forming amorphous and crystalline wear debris.

Table of Contents

List of Figures

List of Tables

Acknowledgements

I would like to express my deep gratitude to my advisor Prof. Hong Liang who gave me this precious opportunity to be her research group member. She was a constant source of inspiration throughout this investigation. Her encouragement and valuable suggestions are greatly appreciated. I would like to acknowledge my committee members Prof. Ataur Chowdhury and Prof. Lutfi Raad at University of Alaska, Fairbanks, AK and Prof. Thomas Dickinson at Washington State University, Pullman, WA for providing me guidance from different areas of expertise.

I am grateful to Prof. Metin at Gebze Institute of Technology, Gebze/Kocaeli Turkey for providing the samples and his timely suggestions.

I would like to thank Dr. Zhiping Luo and Tom Stephens at Microscopy and Imaging Centre, Texas A & M University, College Station for their assistance in TEM and FE-SEM, respectively.

I would like to thank Prof. Liang's research group, Helen Xu, Bing Shi, Juan Ortiz, Rahul Reibeiro, Guruzu Srinivas, Milind Kulkarni, Pranay Asthana, Dedy, and Jee Tae Kwon, for helpful discussions and assistance in different stages of the project.

At last but not the least, I would like to thank my family without whom this destination was impossible.

Chapter 1

Research Objectives

The major goal of this research is to obtain a fundamental understanding of engineering materials in order to improve their tribological performance. This dissertation research applies experimental approaches to reach this goal.

The first objective of this research is to gain insight into the deformation of materials with wear. An atomic force microscope in combination with a transmission electron microscope was used in this research. Various techniques such as a friction force microscopy, a close-contact analysis of roughness surfaces, and digital image analysis were utilized.

The second objective of this research is to understand the basics of materials science in tribological testing. This research focuses on phase transformation, material flow, and work-hardening effects under stress.

The third objective of this research is to investigate the tribological performance of boron coatings for biological applications. Through experimental investigation, it is desired to understand the effects of coatings and identify key elements to improve their performance.

Chapter 2

Introduction

2.1 A Brief History of Friction

2.2 Wear

2.3 Surface Modification Through Coating

2.4 Nanotribology

2.5 References

Tribology has contributed to human culture over hundreds of years. It was not studied systematically, however, until Sir Leonardo da Vinci's precious work gave direction to the scientific study of tribology. Various sources have described tribology as:

"The science of mechanisms of friction, lubrication, and wear of interacting surfaces that are in relative motion" [1].

"A branch of mechanical engineering that deals with the design, friction, wear, and lubrication of interacting surfaces (as bodily joints) in relative motion" [2].

"The branch of engineering that deals with the interaction of surfaces in relative motion (as in bearings or gears): their design and friction and wear and lubrication" [3].

In general, the application of tribological research is to design surfaces to reduce friction or to regulate it. Even today, there is a need to develop fundamental knowledge about frictional force and the coefficient of friction, a constant given by the basic law.

According to this law, frictional force is directly proportional to the applied load. The constant of proportionality is known as the coefficient of friction and is written as:

$$\mu = \frac{F}{P} \qquad (1)$$

Where μ is the coefficient of friction, F is frictional force, and P is applied load.

Understanding of friction involves many experimental difficulties such as changing surface roughness and scales. The development of techniques using the atomic force microscope (AFM) [4, 5], the surface force apparatus [6], and the quartz crystal balance [7, 8] enable surface engineers to study surface forces and friction at the atomic level. The following sections will throw more light on chronological developments in the study of the science of tribology.

2.1 A Brief History of Friction

Friction is the fundamental surface response of a material. The concept of friction was used in ancient times. Much evidence strongly supports the use of this concept. The scientific study of friction was first reported by a painter-turned-engineer, Sir Leonardo da Vinci. He was born in Italy and worked as painter, engineer, and architect, but he was a philosopher as well. He studied very important aspects of tribology, such as friction, wear, bearing materials, plain bearings, lubrication systems, gears, screw-jacks, and rolling-element bearings [9]. One hundred fifty years later, Amonton's laws of friction

were introduced. These laws were actually explained by Leonardo da Vinci, but his manuscripts were hidden or lost for centuries. Amonton and Charles-Augustin Coulomb both made valuable contributions to tribology. Their findings are still applicable to engineering problems today. Some of them, which are applicable to dry friction, are listed here.

1. The force of friction is directly proportional to the applied load. (Amonton's 1st Law)

2. The force of friction is independent of the apparent area of contact. (Amonton's 2nd Law)

3. Kinetic friction is independent of the sliding velocity. (Coulomb's Law)

Though there was a wide impact of lubrication in everyday life at that time, it took many years for scientists to consider lubrication in friction.

Osborne Reynolds recognized the hydrodynamic nature of lubrication, and introduced a theory of fluid-film lubrication. He philosophically mentioned, "*The general character of the motion of the fluids in contact with solid surfaces depends on the relation between a physical constant of the fluid and the product of the linear dimensions of the space occupied by the fluid and the velocity.*" In other words, frictional force is proportional to sliding velocity and bulk fluid viscosity, and inversely proportional to film lubricant thickness [10,11]. This theory is not valid below a critical thickness threshold, explained by Stribeck as today's Stribeck-Curve [12, 13].

The adhesion concept for dry friction was first proposed by Desanguliers [9] and was applied with great success by Bowden and Tabor to metal-metal interfaces [14]. They explained that the force of static friction between two sliding surfaces is strongly dependent on the real area of contact. Their valuable work is known today as the Adhesive Wear Theory, which is applicable for elastic solids. Adhesion is the force required to separate two bodies in contact. The concept of a real contact area was introduced in this theory. The real contact area is the sum of all large numbers of small regions of contacts. In this theory, asperity junctions plastically deform above a critical shear strength, which depends on the adhesive forces of the two mating surfaces.

Tabor [15] also formulated the single-asperity model of contact based on the Hertzian elastic theory [16] for elastic sliding surfaces. They found the non-linear friction-load dependence, which contradicts Amonton's first law.

Archard (1953), a British scientist, explained that there was no difference between Bowden and Tabor's explanation of single asperity model and Amonton's first law [17]. He assumed a load-dependent number of asperities. Greenwood and Williamson [18, 19] further improved the method with a Gaussian and exponential distribution of asperities.

2.2 Wear

"Wear" is defined as a process of material removal from the solid surface by means of mechanical, thermal, or chemical action. It has advantages as well as disadvantages: writing with pencil on paper is one example of useful wear, whereas wear of machines is not useful wear. There are different types of wear modes. They are:

Adhesive wear
Sliding (Delamination)
Fretting wear
Abrasive wear
Erosive wear
Fatigue wear
Corrosive wear

Most of the above-mentioned wear involves the adhesion mechanism, which results in wear. Adhesive wear is the most common wear found in metals and alloys and is discussed here in more detail. During sliding, materials from one sliding surface are transferred to another material's surface due to the adhesive forces between two surfaces. After that, this transfer stays on the same surface or detaches from the surface as debris [20].

Wear in tribology is the surface damage due to the relative motion of two surfaces, the bombardment of one surface on the other, or the reaction between two surfaces or with the surroundings. The science behind these failures is explained by wear mechanisms. Even today different wear mechanisms are reported. Most metals and alloys wear by adhesive interaction. When two surfaces slide together, shearing occurs at the junction. The shear strength of the interface (S_{int}) and the metals (S_1 and S_2) involved in sliding determine the possibility of fragmentation. Bowdon and Tabor [14] explained four different instances in which shearing occur. They are:

a) When the interface is slightly weaker than both the mating surfaces, shearing occurs at the interface ($S_{int} < S_1$ and $S_{int} < S_2$).

b) When the interface is stronger than one of the mating surface and weaker than the other, shearing occurs within the softer metal and the detached fragment adheres to the harder sliding metal ($S_2 < S_{int} < S_1$).

c) When the interface is stronger than the mating surface but slightly harder than one of the mating surface, severe shearing occurs on the softer metal, and a significant amount of metal transfers to the harder metal. Shearing of the harder metals also occasionally occurs ($S_2 \leq S_{int} < S_1$).

d) When the interface is significantly stronger than both the sliding metals, shearing occurs at some distance from the interface. In such a situation, transfer of metals occurs from both the surfaces and the surface damage encountered in this situation increases ($S_{int} > S_1$ and $S_{int} > S_2$).

The schematic of all these possibilities is shown in Figure 2.1 [14].

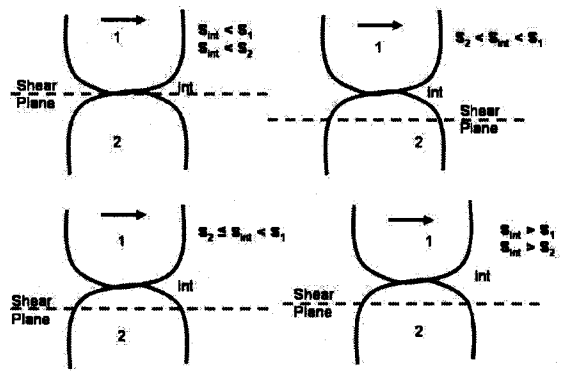

Figure 2.1: Shearing and wear of metals [14].

N. P. Suh [21, 22] developed the delamination theory to explain adhesive wear. According to him, adhesive wear occurs when cracks formed under the surface propagate under continuous load conditions. This leads to failure of the surface. With continuous sliding, the dislocations pile up at a finite distance from the surface. As the sliding goes on, voids are formed at the pile-up region. The rate of void formation is more if the material contains a hard second phase for dislocations to pile against. When there are large secondary phase particles in the metal, voids are formed by a plastic flow of matrix around hard particles. Clustering these voids results in a crack which propagates parallel to the wear surface. The separated particle is a plate-like structure. The formation of the void at a distance from the surface is shown in Figure 2.2 [21].

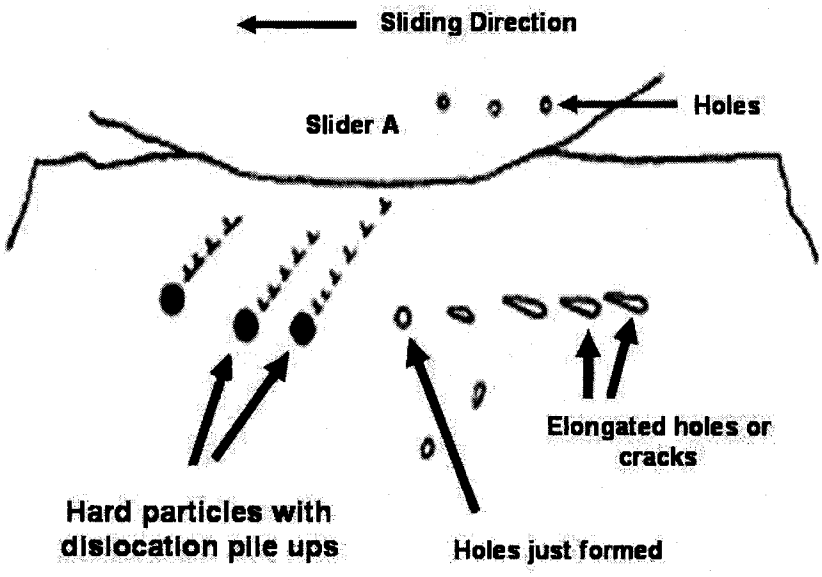

Figure 2.2: Formation of debris by shear deformation [21].

Adhesive wear can be expressed quantitatively. Holms in 1946 [23] and then Archard in 1953 [24] explained the volume worn by adhesion. The amount of wear is dependent on load, sliding distance, and hardness of the surface. The wear volume is given by:

$$V = \frac{cLx}{p} \qquad (2)$$

where c is a nondimensional constant, L is the load, x is the sliding distance, and p is the hardness of the surface.

2.3 Surface Modification Through Coating

Surface science is the study of surface morphology, forces, and their interactions. Its applications include, but are not limited to, engineering, nanotechnology, MEMS, meso-manufacturing, medical sciences, agriculture, and drug delivery. The modification of the surfaces to meet the application demand has always been challenging for surface scientists. The advancements in coating technology have made the development of superior quality surfaces easy. Today, tribological coatings are developed over a wide range.

High wear resistance and low friction surfaces are in everlasting demand for tribological applications. Materials with superior properties are being developed by alloying and thereafter by heat treatments. The performance of the surfaces can be further improved by modification techniques. Modifying the surface properties is one approach.

Surface modification technologies have been in development over the past decade, and they were always points of attention for tribologists and lubrication engineers.

Coatings can be divided into five categories: gaseous state, solution state, solid state, molten, and semi-molten state processes [25]. Each process has its own advantages and disadvantages. It is not within the scope of the present study to discuss these processes in detail, but the coatings are described here in brief.

Gaseous state processes are divided into two subcategories: chemical vapor deposition (CVD) and physical vapor deposition (PVD). In the CVD process, the target element is introduced into the chamber in a volatile form, which then condenses on the substrate, forming a uniform coating. The CVD technique has different derivatives, which depend on various means of introduction of the target element. The target element can be induced to form a coating with pressure, temperature [26], electrons, or a laser [27]. The pressure in pressure assisted CVD ranges from atmospheric to 1 Pa or less. The schematic of a typical CVD process is shown in Figure 2.3 [28].

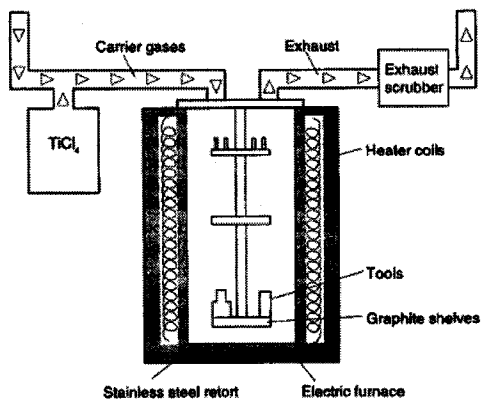

Figure 2.3: A typical CVD process layout [26].

Thermally activated CVD can be used to deposit wear resistant coatings like borides, carbides, nitrides, oxides, and transition metals [29]. The reaction zones in thermally activated CVD are shown in Figure 2.4 [30].

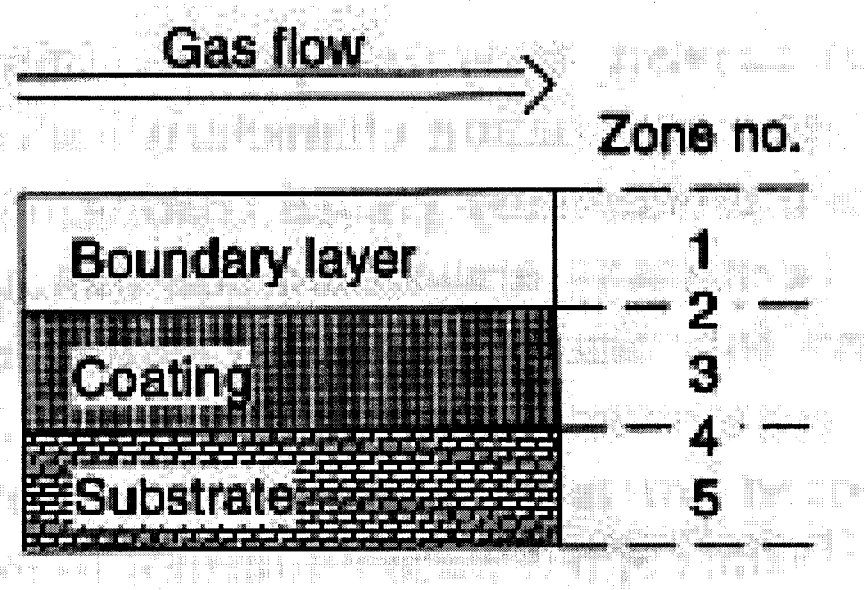

Figure 2.4: The reaction zones in thermally activated CVD [30].

In the physical vapor deposition process, the target metal is vaporized to form a coating on the substrate. Berghaus patented this process in 1938 in the United Kingdom [31]. The plasma assisted pressure vapor deposition (PAPVD) has been developed recently and is widely used over the PVD. PAPVD is also known as ion plating. The mechanisms of ion bombardments are shown in Figure 2.5 [32]. The sputtering mechanism in PAPVD helps cleaning of the surface before formation of the coating on the substrate. It also forms the pseudo-diffusion layer between the substrate and the coating. This also helps in redistributing the atoms on the surface during film growth [28].

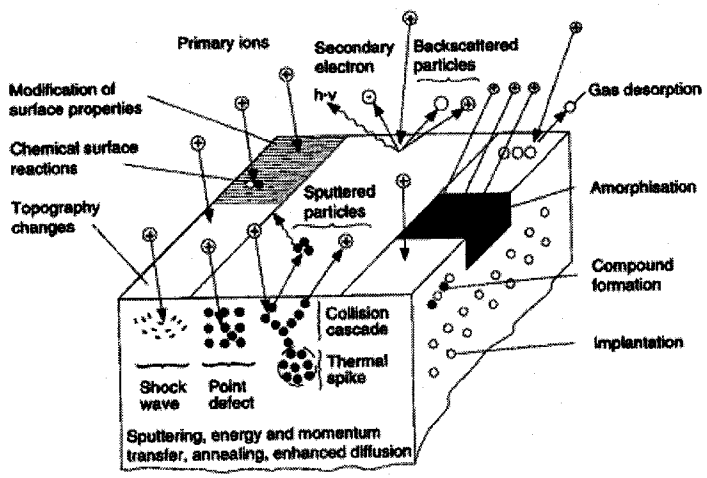

Figure 2.5: Different mechanisms in ion bombardment [32].

The solution state process can be subdivided into two broad categories: electroplating and electroless plating. The aqueous solution of a target element can be deposited on metallic or non metallic substrate [28]. This process may be divided into chemical and electrochemical processes. However, according to Lowenheim [33], some reactions that appear to be chemical in actuality may be electrochemical. In chemical solution deposition, a uniform coating is formed by reduction of a metal ion in the solution by a reducing agent, by auto catalytic deposition, or by a reagent in solution that reacts with a substrate to form a compound. In electrochemical deposition, the target elements are deposited by electrolysis and the substrate acts as an electrode [28].

The molten and/or semi molten state processes include laser surface treatment, thermal spraying, and welding. Laser surface treatment can coat the surface in a focused area. The details of the laser surface treatment are explained elsewhere [34]. The laser surface treatment can change the properties of the surface. The laser can be used to heat the surface for structural transformations and other heat treatments. The microstructural

changes can also be made using the laser heat to improve the performance. To form the coating, in the thermal spraying technique, the target material is heated in a gaseous medium and projected on the substrate at a very high velocity [35].

2.4 Nanotribology

Microelectromechanical systems (MEMS), meso-manufacturing, nanotechnology, and biotechnology are recent advancements in engineering, science, and technology. They have been attracting the attention of scientists for over a decade. MEMS involve devices at the micro level, which are mostly made by micro machining. Nanotechnology has a strong impact on areas such as engineering, biology, biomedical, computing, communications, and drug delivery. It involves materials at very small dimensions, i.e., less than 100nm. Manufacturing at such a miniature level requires knowledge of materials behavior at that scale. There has been exhaustive study of the behavior of various materials at nano levels. As we reduce the size, the surface-to-volume ratio increases. At nano levels, surface properties are very important because these properties dominate the surface performance. The failure of the materials at any level is a critical issue; hence, reliability of the materials is very important at every scale. Among various failure modes, wear is one crucial mode to be considered. Thus, it is essential to study the wear and friction behavior of materials at the miniature level.

Development of scanning probe microscopy has provided a valuable tool to study behavior of materials at micro and nano levels. Various techniques have been developed to measure the mechanical properties of the materials at such miniature levels. These

techniques include surface force measurement [6], atomic force microscopy [4, 5], friction force microscopy [36], nano indentation, and nano scratching.

The scanning probe microscope (SPM) has opened up research in material science, biology, drug delivery, and many other areas. Scanning force microscopy is a standard characterization tool in polymers and semiconductor studies. Magnetic force microscopy (MFM) has become a tool for routine analysis, enabling fundamental research. The friction force microscope has opened broad areas in the tribological research. The atomic force microscope (AFM) can image bio-systems in a near-natural state [37]. Scott S. Perry has given an overview of the use of a scanning probe microscopy (SPM) in the measurement of friction [38]. The development of the first friction force microscope in 1987 by C. Mathew Mate and co-workers at IBM opened the door for atomic level friction measurement. They reported interfacial friction measurements performed at the nanometer length scale between a tungsten tip and a graphite surface [39]. Following that, many investigations were conducted in these areas on different materials.

AFM has emerged as a powerful tool to study surface properties at micro and nano levels [40, 41, 42]. The friction force microscope [43], atomic force microscope [44], and scratch test [45] have been used to measure micro and nano scale friction, and wear behavior. Scratching, wear properties, hardness, and Young's modulus of polycarbonate (PC) polymer were investigated by AFM and nano indentation [46]. AFM was used to measure the adhesion and frictional properties of the outermost surfaces of a

variety of human hairs [47]. Nanotribological study of cluster assembled carbon films [48], diamond and hard carbon films [49] have been conducted.

The study of nanotribology is important in biomedical applications as well. Submicron wear debris particles of ultra high molecular weight polyethylene (UHMWPE) used in total joint replacement (TJR) prostheses have been clinically observed to cause osteolysis. Therefore, the knowledge of the wear behavior of UHMWPE at nano levels is essential. Such a study was conducted using contact mode atomic force microscopy [50].

Wear can occur by means of different mechanisms, or a combination of them. Most studies of wear mechanisms were observed using conventional imaging techniques. Wear mechanisms at nano levels cannot be observed using these techniques, but AFM has enabled such studies. The details of AFM imaging principles are discussed in Chapter 4.

2.5 References

1 The American Heritage® Dictionary of the English Language, Fourth Edition Published by Houghton Mifflin Company.

2 Merriam-Webster Medical Dictionary, © 2002 Merriam-Webster, Inc.

3 WordNet ® 2.0, © 2003 Princeton University.

4 G. Binning, H. Rohrer, Ch. Gerber, E. Weibel, "Surface studies by scanning tunneling microscopy" Physical Review Letters 49 1982 p57.

5 G. Binning, C. F. Quate, "Atomic force microscope" Physical Review Letters 56 1986 p930–933.

6 J. N. Israelachvili, Chemtracts-Analytical and Physical Chemistry 1 1989 p1-12.

7 J. Krim A. Widom, "Damping of a crystal oscillator by an adsorbed monolayer and its relation to interfacial viscosity" Physical Review Letters B 38 1998 p12184.

8 J. Krim, D. H. Solina, R. Chiarello, "Nanotribology of a Kr monolayer: A quartz-crystal microbalance study of atomic-scale friction" Physical Review Letters 66 1991 p181.

9 D. Dowson, "History of Tribology" Professional Engineering Publishing, London, UK, 1998.

10 O. Reynolds, "An experimental investigation of the circumstances which determine whether the motion of the water shall be direct or sinuous and of the law of resistance in parallel channels" Philosophical Transactions of the Royal Society of London, 174 1883 p935-982.

11 O. Reynolds, "On the theory of lubrication and its application to Mr. Beauchamp's experiments, including an experimental determination of the viscosity of olive oil" Philosophical Transactions of the Royal Society of London 177 1886 p157.

12 R. Stribeck, "Kugellager für beliebige Belastungen" Zeitschrift des Vereines deutscher Ingenieure 45 3 1901 p73–79.

13 R. Stribeck, "Die wesentlischen Eigenschaften der Gleit- und Rollenlager" Zeitschrift des Vereines deutscher Ingenieure 1902 46(37) p1341-1348 (part I), 46(38) p1432-1438 (part II) and 46 (39) p1463-1470 (part III).

14 F. P. Bowden, D. Tabor, "The Friction and Lubrication of Solids, Parts I, II" Clarendon Press, Oxford 1964.

15 D. F. Tabor, "Friction, lubrication and wear" In: E. Matijevic, Editor, Surface and Colloid Science vol. 5, Wiley-Interscience Publishers, New York 1972.

16 K. L. Johnson, Journal of the Mechanics and Physics of Solids 18 115 1970.

17 G. Amonton, Memoires de l'Academie Royale 1699 p206.

18 J. A. Greenwood, J. B. P. Williamson, "Contact of nominally flat surfaces" In: (2nd edn), Proceedings of the Royal Society of London, Series A 295 1966 p300–319.

19 J. A. Greenwood, J. H. Tripp, "The contact of two nominally flat rough surfaces" In: (2nd edn. ed.), Proceedings of the Institution of Mechanical Engineers 185 1971 p625–633.

20 E. Rabinowicz, "Friction and Lubrication of Materials" John Wiley & Sons, Inc. 1995.

21 N. P. Suh, "The delamination theory of wear" Wear 25 p111-124.

22 N. P Suh, "Tribophysics" Prentice-Hall, Englewood Cliffs, NJ 1986 .

23 R. Holm, "Electric Contacts" Almquist and Wiksells, Stockholm 1946.

24 J. F. Archard, "Contact and rubbing of flat surfaces" Journal of Applied Physics 24 1953 p.981-988.

25 D. S. Rickerby, A. Matthews [Eds] "Advanced Surface Coatings, A Handbook of Surface Engineering" Blackie, Glasgow 1991.

26 J. Thornton, "Influence of apparatus geometry and deposition conditions on structure and topology of thick sputtered coatings" Journal of Vacuum Science and Technology 11 1974 p666.

27 R. D'Agostinov, P. Favia, F. Fracassi, R. Lamendola, "Plasma enhanced chemical vapor deposition" In: Advanced Techniques for Surface Engineering, W. Gissler, H. A. Jehn [Eds], Kluwer Academic Publishers, Dordrecht, The Netherlands, 1992 p105-133.

28 K. Holmberg, A. Matthews, "Coatings Tribology" Elsevier 1994.

29 T. S. Sudarshan, "Wear Resistant coatings" Tech Trends, International Reports on Advanced Technologies, Innovation 128, S.A. Paris 1992 p195.

30 P. Carlsson, "Thermally activated chemical vapor deposition" In: Advanced Surface Coatings, A Handbook of Surface Engineering, D. S. Rickerby, A. Mathews [Eds], Blackie, Glasgow 1991.

31 B. Berghaus, "Improvements in and related to the coatings of articles by means of thermally vaporized materials" UK patent Specification 510992 1938.

32 C. Weissmantel, "Application of ion beams for the preparation of thin films" Proceeding IX IVC-VICES, Madrid, Spain, 1983 p300.

33 F. R. Lowenheim, "Deposition of inorganic film from solution" In: Thin Film Processes, J. L. Vossen, W. Kern [Eds], New York, USA, Academic Press, 1978 p209-256.

34 F. C. J. Fellowes, W. M. Steen, "Laser surface treatment" In: Advanced Surface Coatings, A Handbook of Surface Engineering, D. S. Rickerby, A. Mathews [Eds], Blackie, Glasgow 1991.

35 K. T. Scott, R. Kingwell, "Thermal spraying" In: Advanced Surface Coatings, A Handbook of Surface Engineering, D. S. Rickerby, A. Mathews [Eds], Blackie, Glasgow 1991.

36 C. M. Mate, G. M. McClelland, R. Erlandsson, S. Chiang, "Atomic scale friction of a tungsten tip on a graphite surface" Physical Review Letters 59 1987 p1942.

37 E. Meyer, S. P. Jarvis, N. D. Spencer [Eds] "Scanning probe microscopy in materials science" MRS Bulletin July 2004 p443-448.

38 S. S. Perry "Scanning probe microscopy measurements of friction" MRS Bulletin, July 2004 p478-483.

39 C.M. Mate, G.M. McClelland, R. Erlandsson, S. Chiang, "Atomic scale friction of a tungsten tip on a graphite surface" Physical Review Letters 59 1987 p1942.

40 B. Bhushan [Eds] "Handbook of Micro/Nano Tribology" CRC Press, New York 1995.

41 L. G. Hector, S. R. Schmid, "Simulation of asperity plowing in an atomic force microscope Part 1: Experimental and theoretical methods" Wear 215 (1-2) 1998 p247-256.

42 S. R. Schmid, L. G. Hector, "Simulation of asperity plowing in an atomic force microscope Part II: Plowing of aluminum alloys" Wear 215 (1-2) 1998 p257-266.

43 H. Schonherr, G.J. Vancso, "Molecular resolution imaging and friction anisotropy of highly oriented polyethylene and poly(tetrafluoroethylene) by scanning force microscopy with chemically modified probes" Macromolecules 30 1997 p6391.

44 B. Bhushan, C. Dandavate, "Thin-film friction and adhesion studies using atomic force microscopy" Journal of Applied Physics 87 2000 p1201.

45 C. Charitidis, S. Logothetidis, M. Gioti, "A comparative study of the nanoscratching behavior of amorphous carbon films grown under various deposition conditions" Surface & Coatings Technology 125 2000 p201.

46 T. Fang, W. Chang, S. Tsai, "Nanomechanical characterization of polymer using atomic force microscopy and nanoindentation" Microelectronics Journal, 36 (1) 2005 p55-59.

47 S. Breakspear, J. R. Smith, G. Luengo, "Effect of the covalently linked fatty acid 18-MEA on the nanotribology of hair's outermost surface" Journal of Structural Biology, In Press, Corrected Proof, Available online 15 December 2004.

48 R. Buzio, C. Boragno, U. Valbusa, "Nanotribology of cluster assembled carbon films" Wear 254 (10) 2003 p981-987.

49 I. S. Forbes, J. I. B. Wilson, "Diamond and hard carbon films for microelectromechanical systems (MEMS)—a nanotribological study" Thin Solid Films, 420-421 2002 p508-514.

50 S. P. Ho, R. W. Carpick, T. Boland, M. LaBerge, "Nanotribology of CoCr–UHMWPE TJR prosthesis using atomic force microscopy" Wear 253 (11-12) 2002 p1145-1155.

Chapter 3

Materials

3.1 Materials Selection

This research study encompasses fundamental aspects of tribology. It includes friction induced phase transformation, hardening and oxidation during sliding, nano tribology, and biotribology. The materials used in this investigation are categorized into two major types: active metals and refractory borides. The active metals are copper, aluminum, and silicon. Silicon was used in two different forms (single-crystal and amorphous) in this investigation. Silicon was used to study the feasibility of using an atomic force microscope (AFM) for phase detection. A wide range of standard data is available for this metal. Aluminum and copper with a purity of 99.99% were used for this study. The different properties of metals and borides used are discussed later. A solid

reaction process called "boronizing" formed refractory borides. Boronizing was conducted at the Gebze Institute of Technology, Department of Materials Science and Engineering, Gebze / Kocaeli, Turkey.

3.2 Active Metals

Over the years, copper and aluminum have been used in many engineering applications. Their properties are well studied and documented, and are available in many handbooks and on the Internet as well. Some of the important properties of these metals are reported here.

3.2.1 Chemical Properties

Aluminum forms a continuous oxide coating on its surface, which hinders further oxidation of the aluminum underneath. Copper also forms the oxide layer, but the copper oxide layer is porous and further oxidizes the underlying copper. The chemical properties of Al and Cu are listed in Table 3.1 [1, 2].

3.2.2 Physical and Mechanical Properties

The physical and mechanical properties are very important when a metal is considered for its alloy development or for selection of particular applications. These properties play a vital role in designing the mechanical components. These properties are also helpful in forecasting the service life of the component and its failure modes.

Unalloyed aluminum is designated by the code 10XX. The last two digits of the four digits indicate the minimum percentage of Al. Physical properties of annealed aluminum are listed in Table 3.2 [3]. Mechanical properties of annealed aluminum are listed in Table 3.3 [3]. The density of annealed aluminum is 2.705 g/cm^3.

Oxygen free electronic copper is designated as C10100. It has a very high conductivity and ductility. The density of copper is 8.96 g/cm^3. Physical properties of copper (C10100) are listed in Table 3.4 [3]. Mechanical properties of copper (C10100) are listed in Table 3.5 [3].

Al and Cu together form a binary alloy, containing 33 Wt% of Cu, with an eutectic reaction at 548.2°C. Figure 3.1 shows Al rich portion of the Al-Cu binary phase diagram [3]. Copper has a maximum solubility of 5.65% in Al at the eutectic temperature.

3.3 Refractory Metals

Non-ferrous refractory metals (transition metals) such as tungsten, chromium, niobium, and tantalum are used as substrate materials for boronizing. The metals used were annealed. These metals were obtained from Alfa Aesar®.

3.3.1 Chemical Properties

Refractory metals have very high melting points and good corrosion resistance. These metals also have favorable mechanical properties. Due to their high corrosion

resistance and biocompatibility, these metals attract great attention as bio materials. Some of the chemical properties of pure refractory metals are listed in 3.6 [1, 2].

3.3.2 Physical and Mechanical Properties

The physical and mechanical properties of the pure refractory metals (W, Nb, Ta and Cr) are listed in Table 3.7 [3].

3.4 Boronized Refractory Metals

There are few data available on the properties of boronized refractory metals. Some of the properties of the boronized refractory metals used in the present investigation are listed in Table 3.8 [1, 2].

3.5 Materials Synthesis

As discussed in previous sections, there are two different categories of metals used in this investigation. The refractory metals were boronized to form a hard and wear-resistant coating on their surfaces. This coating process is a solid-state process. The process is discussed in detail in this section.

Boron atoms, owing to their relatively small size and high mobility, can diffuse easily into metals, forming intermetallic, non-oxide borides. Boronizing is a thermo-chemical diffusion surface treatment in which boron atoms diffuse into the surface of the specimen to form hard borides with the base materials [4, 5, 6, 7]. The resultant boronized coating gives their surfaces a very high hardness and wear resistance. A wide

range of steel alloys including carbon steel, low alloy steel, tool steel, and stainless steel can be boronized. Additionally, nonferrous metals and alloys such as nickel base alloys, cobalt base alloys, molybdenum, and titanium can also be boronized. The strong covalent bonding in most transition metal diborides is largely responsible for their high melting points, high mechanical strength, elastic moduli, hardness values, and chemical inertness [8]. Dzyadykevich and Kytskay reported that successive treatment of niobium and tantalum samples with boron and silicon can lead to a diffusion coating. During this boro-siliconizing process, a double-layer coating consisting of a refractory metal (M), an outer layer (MSi_2), and a boride phase inner layer (MB_2) were formed [9].

In the present study, boronizing was performed in a solid medium by using EKabor® powder, which has a nominal chemical composition of 90% SiC, 5% B_4C, and 5%KBF_4. The pre-polished refractory metal specimens to be coated were placed in contact with EKabor® powder. The size and shape of these specimens were different for chromium compared with the rest of the refractory metals. The boronizing agents are available in different grain sizes and pastes. The EKabor® boronizing agents are listed in Table 3.9. The main constituents of these agents are the boron donor, the activator, and the filler [10]. The boronizing experiment was conducted at 940°C for 2, 4, 6 and 8 hours. Following boronizing, the specimens were air cooled. A schematic of the boronizing experimental setup using a chamber furnace is shown in Figure 3.2 [7].

Borides formed on the metallic surface were characterized by a scanning electron microscope, X-ray diffraction, and hardness measurements.

Table 3.1: Chemical properties of active metals [1, 2].

Materials	**Atomic radius (nm)**	**Ionic radius (nm)**	**Atomic Number**	**Crystal Structure**	**Electronic configurations**
Aluminum	0.143	0.057	13	FCC	$1s^2\ 2s^2\ 2p^6\ 3s^2\ 3p^1$
Copper	0.128	0.096	29	FCC	$1s^2\ 2s^2\ 2p^6\ 3s^2\ 3p^6\ 3d^{10}\ 4s^1$

Table 3.2: Physical properties of annealed Al [3].

Properties		**1060**
Average coefficient of thermal expansion (a) μm/m ^{O}C		23.6
Approximate melting range, ^{O}C		645-655
Thermal conductivity at 25 ^{O}C (W/m ^{O}C)		234
Electrical Conductivity at 20 ^{O}C	Equal volume	62
	Equal weight	204

Table 3.3: Mechanical properties of Al [3].

Properties	**1050**	**1060**	**99.999+ % Pure**
Tensile strength (MPa)	76	69	40-50
Yield strength (MPa)	28	28	15-20
Elongation (%)	39	43	50-70
Shear strength (MPa)	62	48	--
Hardness HB(b)	--	19	--

Table 3.4: Physical properties of Cu (C10100) [3].

Properties	**C10100**
Average coefficient of thermal expansion μm/m ^{O}C	17.0
Melting point, ^{O}C	1083
Thermal conductivity at 25 ^{O}C (W/m ^{O}C)	391

Table 3.5: Mechanical properties of Cu (C10100) [3].

Properties	**C10100**
Tensile strength (MPa)	221-455
Yield strength (MPa)	69-365
Elongation (2 in.) %	55-4
Shear strength (MPa)	~150-200
Hardness HB(b)	~45-95

Table 3.6: Chemical properties of pure refractory metals [1, 2].

Metals	**Atomic radius (nm)**	**Ion**	**Ionic radius (nm)**	**Atomic number**	**Crystal structure**	**Electronic configurations**
Cr	0.125	Cr^{3+} Cr^{5+}	0.064 0.03-0.04	24	BCC	[Ar] $3d^5$ $4s^1$
Nb	0.143	Nb^{4+}	0.074	41	BCC	[Kr] $4d^4$ $5s^1$
Ta	0.147	Ta^{5+}	0.068	73	BCC	[Xe] $4f^{14}$ $5d^3$ $6s^2$
W	0.137	W^{4+} W^{6+}	0.068 0.065	74	BCC	[Xe] $4f^{14}$ $5d^4$ $6s^2$

Table 3.7: Physical and mechanical properties of pure refractory metals [3].

Property	Niobium	Tantalum	Tungsten	Chromium
Atomic Weight	92.9064	180.95	183.85	51.966
Density at 2 °C, g/cm3	8.57	16.6	19.25	7.19
Crystal Structure	Bcc	Bcc	Bcc	Bcc
Lattice constants nm	0.3294	0.3303	0.3165	0.28844-0.28848
Slip plane at RT	110	110	--	--
Melting point	2468	2996	3410	1875
Coefficient of thermal expansion μm/m K	7.3	6.5	4.6	6.2
Thermal conductivity at RT w/m.K	52.7	54.4	155	67
Elastic modulus, GPa	103	185	400	248
DTB transition temp	<147	<25	250	--

Table 3.8: Properties of refractory borides [1, 2].

Materials	Molecular weight	Melting point	Crystal structure	Lattice parameters (Å)	X-ray density gm/cm^3
NiB	103.73	>2000	Orthorhombic	a = 3.298 b = 8.724 c = 3.137	-- -- --
NiB_2	114.55	2900	Hexagonal AlB_2 type	a = 3.086 c = 3.306	7.21
TaB	191.77	>2000	Orthorhombic	a = 3.276 b = 8.669 c = 3.157	14.29
TaB_2	202.59	3000	Hexagonal AlB_2 type	a = 3.088 c = 3.241	12.60
CrB_2	73.65	1850	Hexagonal AlB_2 type	a = 2.969 c = 3.066	5.16
WB	194.65	2860	Tetragonal	a = 3.115 c = 16.92	16.0
W_2B	378.54	2770	Tetragonal $CuAl_2$ type	a = 5.564 c = 4.740	16.72

Table 3.9: EKabor® boronizing agents [7].

Boronizing agents	**Grain size, μm**	**Compacted density, g/cm^3**	**Comments**
EKabor® 1	≤ 150	Approx. 1.8	Highest quality surface layer; tends to bond together.
EKabor® 2	≤ 850	Approx. 1.5	Excellent surface layer; simple unpacking of the part after treatment.
EKabor®3	≤ 1400	Approx. 0.95	Very good surface layer; flowability of the powder still good after treatment.
EKabor® HM	≤ 150	Approx. 0.95-1.50	For hard metal, small bore size and thick boride layers; very good surface layers.
EKabor® Paste		Approx. 1.90	Applicable universally; immersion, brushing, spraying (inert gas necessary).
EKabor® WB	200-400	Approx. 0.95	Designed for boronizing in a fluidized bed in oxygen-free gas atmospheres.
EKrit	≤ 420	Approx. 1.55	Cover material; prevents oxygen penetration during boronizing with solid boronizing agents.

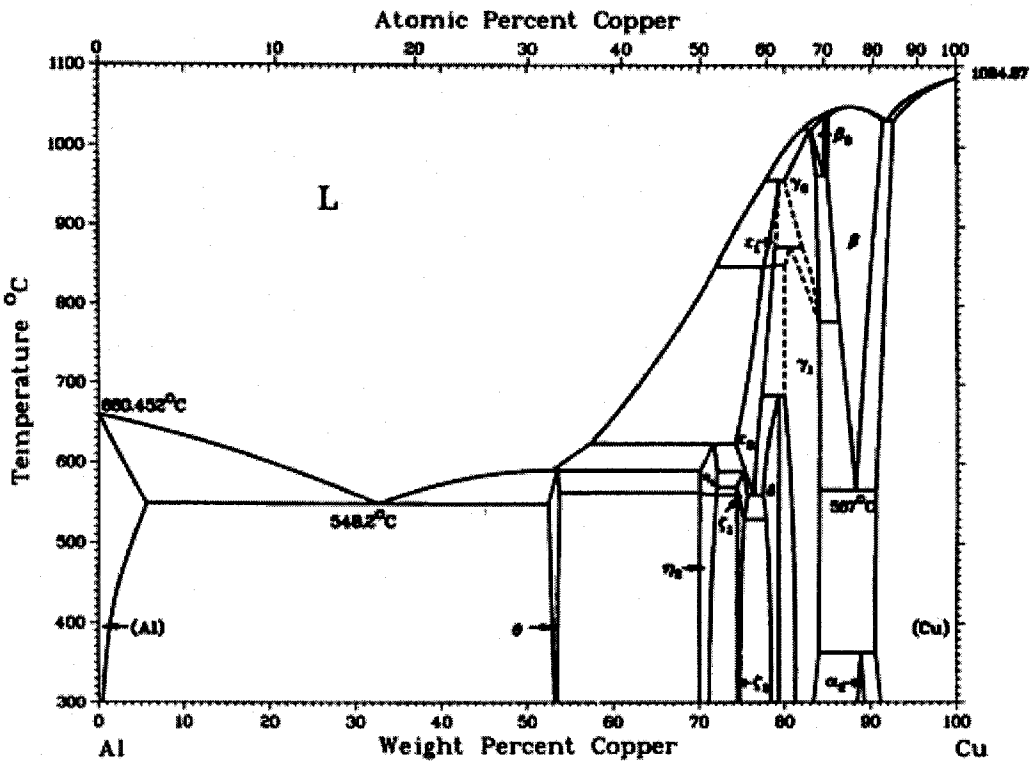

Figure 3.1: Aluminum copper binary phase diagram [3].

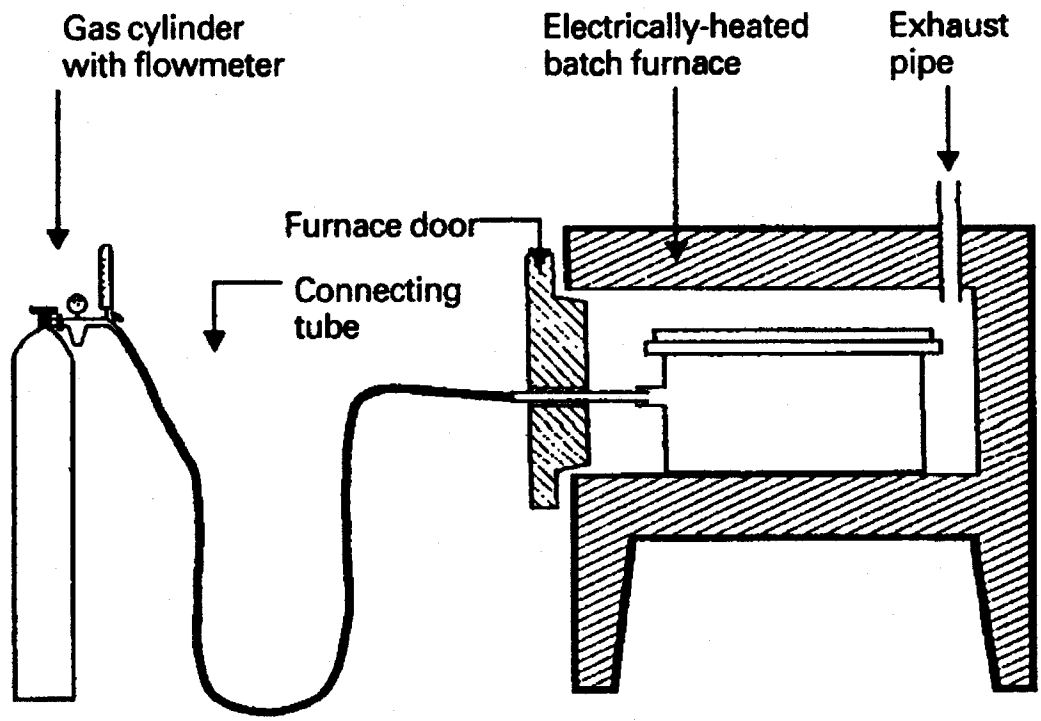

Figure 3.2: Schematic of chamber furnace for boronizing [7].

3.6 Characterization of Boronized Refractory Metals

Metallographic observations were conducted using a scanning electron microscope (SEM). The morphology of borides formed on the substrate was observed. This revealed a nearly compact and smooth boride layer. Figures 3.3, 3.4, and 3.5 show the continuous layers of borides on tungsten, chromium, and niobium respectively. These figures are for refractory metals which were boronized at 940°C for 8 hours.

The boronizing process is a diffusion process. Upon reaching the surface, atoms either form interstitial solid solutions or react with substrate to form borides. Because of successive diffusion from the surface to the bulk of the substrate, the concentration of the boron atoms is different. This leads to the formation of three regions. These regions are shown in Figures 3.3 and 3.4. In Figure 3.3 region "1" is the boride layer, where the boron atoms formed the borides with tungsten. Region "2" is the boron rich diffusion/transition zone, while region "3" is the substrate material not affected by boron atoms. Similar regions were observed in other boride layers as well.

It is difficult to distinguish region 1 from region 2. However, it is possible to separate region 2 from region 3 with a microhardness indentation test. The microhardness of boronized refractory metals and underlined substrate along the cross-section was measured by an Instron microhardness tester attached to a Vickers diamond indenter at a constant load of 100 g (0.98N). Samples were prepared by using a conventional metallographic technique before the measurements. The micro indents are shown in Figures 3.6, 3.7, and 3.8 for boronized tungsten, chromium, and niobium, respectively.

These micrographs are for refractory metals which were boronized at 940°C for 8 hours. According to Figures 3.6, 3.7, and 3.8, the hardness increases towards the surface of the coating. The hardness of the borides is much higher than that of the substrate underneath. The hardness values are given in Table 3.10.

Borides were characterized by X-ray diffraction with a Rigaku X-Ray Diffractometer. Figure 3.9 illustrates the x-ray diffraction results of the boronized (at 940°C for 8 hours) tungsten. It shows the presence of single phase, WB, on the surface. The high concentration of B enables the formation of WB, which is one of the eutectic phases in the W-B binary alloy system. According to the W-B phase diagram, there are four different types of tungsten borides: W_2B_5, WB, WB_4, and W_2B. They are all nonstoichiometric intermetallic compounds that have a range of compositions. Figure 3.12 shows the binary phase diagram of W and B [3].

Figure 3.10 reveals the X-ray diffraction pattern of the boronized chromium. It shows the presence of CrB. There are six chromium borides (Cr_2B, Cr_5B_3, CrB, Cr_3B_4, CrB_2, and CrB_4), according to the Cr-B phase diagram shown in Figure 3.13 [11]. They all are stoichiometric intermetallic compounds that have a fixed composition.

Figure 3.11 shows the X-ray diffraction pattern of the boronized niobium. Results show the presence of NbB_2. According to the equilibrium phase diagram of Nb-B, there are five niobium borides: Nb_3B_2, NbB, Nb_5B_6, Nb_3B_4, and NbB_2. Figure 3.14 shows the binary phase diagram of Nb and B [3]. A single-phase layer of borides is desirable for stability and uniform surface properties.

Table 3.10: Hardness Measurements.

Metal	Boronized surface	Transition region	Substrate
Tungsten	2500	655	445
Niobium	2500	670	110
Chromium	1700	365	110

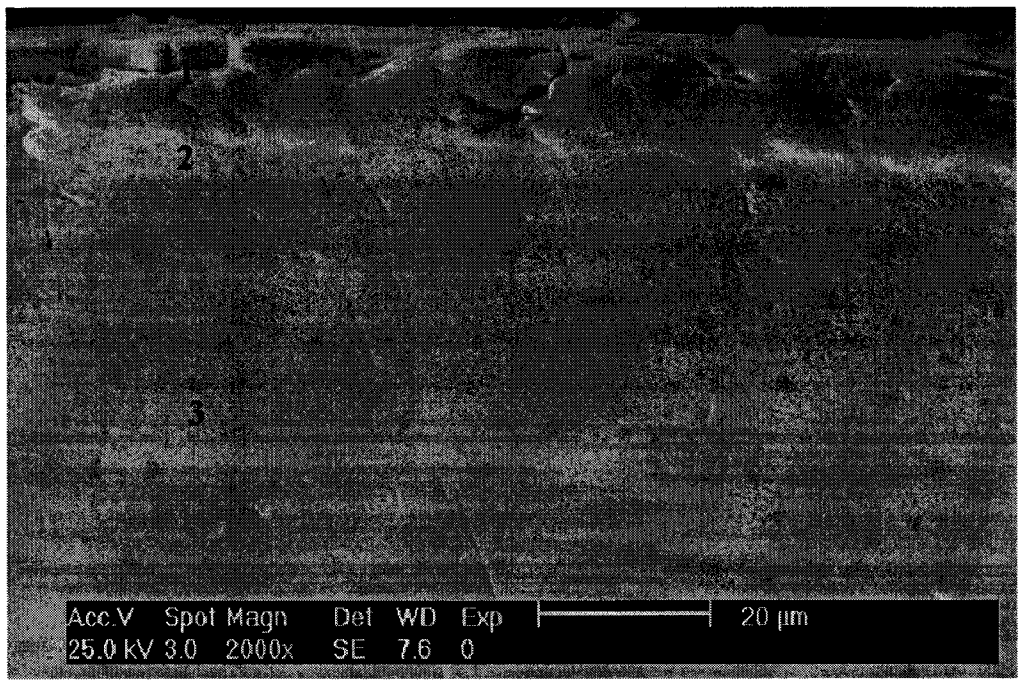

Figure 3.3. SEM image of tungsten boronized at 940°C, for 8 hours, 1- boride layer, 2- transition layer and 3- base metal.

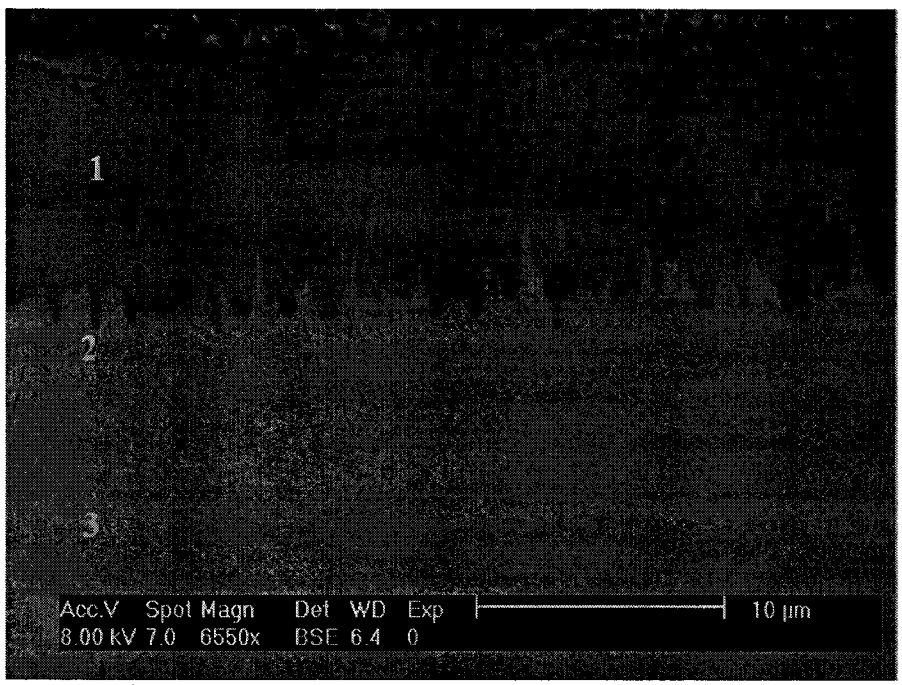

Figure 3.4. SEM image of chromium boronized at 940°C for 8 hours, 1- boride layer, 2- transition layer and 3- base metal.

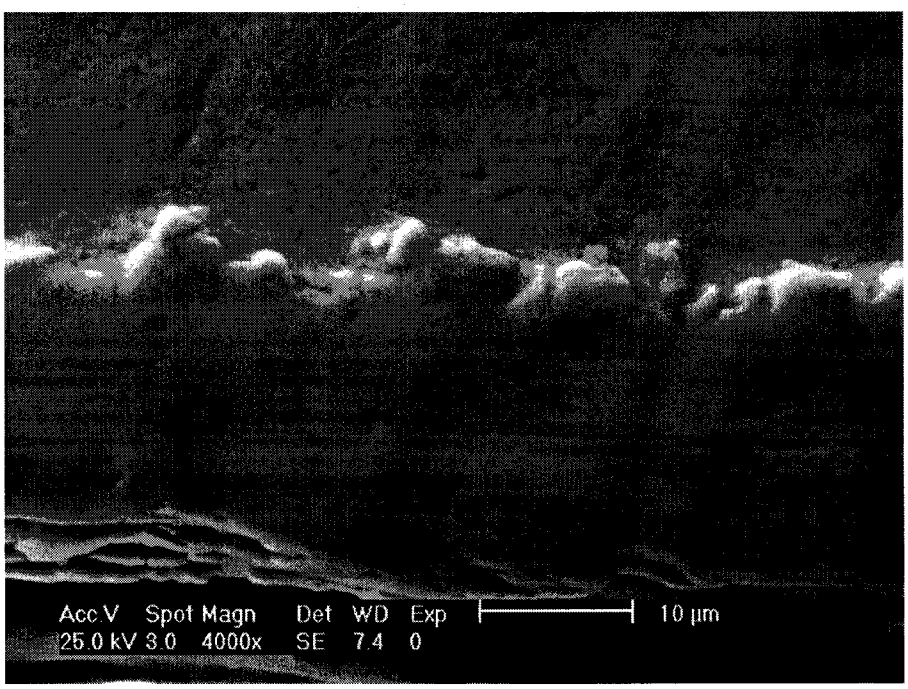

Figure 3.5. SEM image of niobium boronized at 940°C.

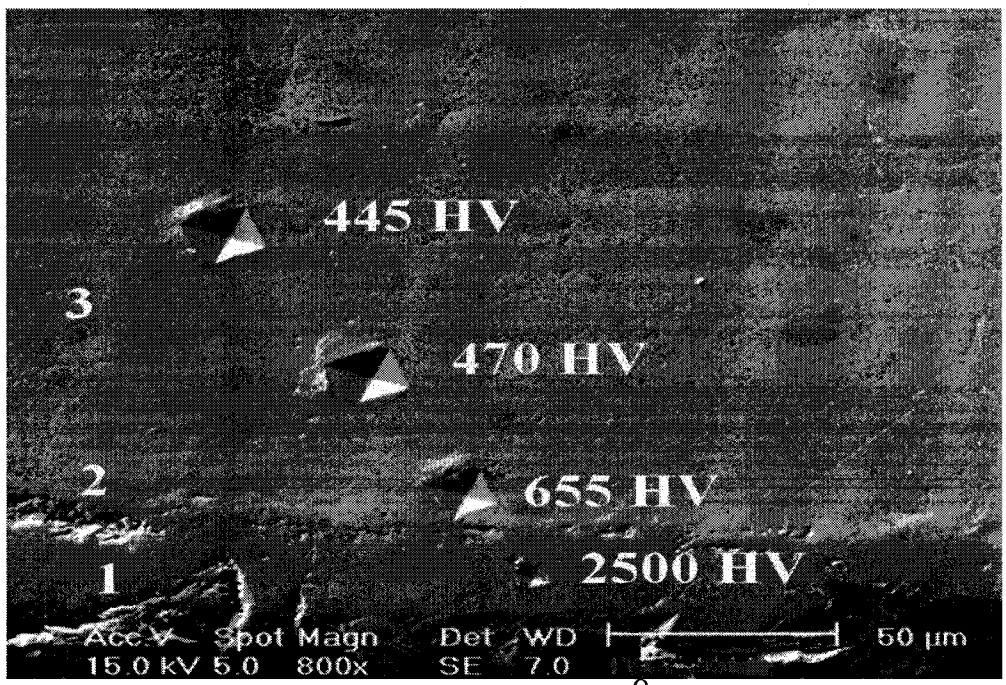

Figure 3.6: SEM image of tungsten boronized at 940^{O}C for 8 hours, showing Vickers indents.

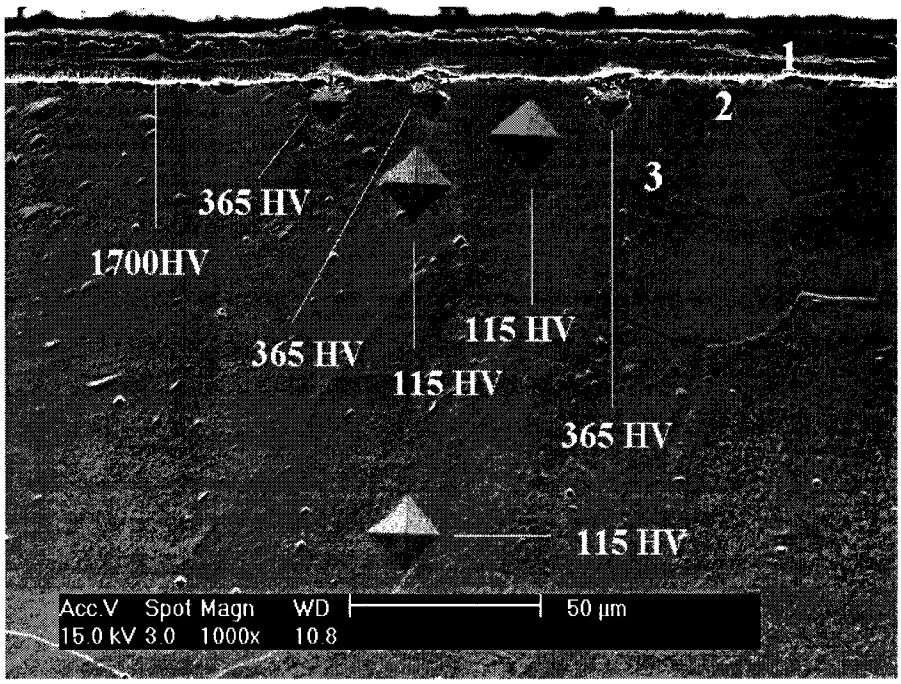

Figure 3.7: SEM image of chromium boronized at 940^{O}C for 8 hours, showing Vickers indents.

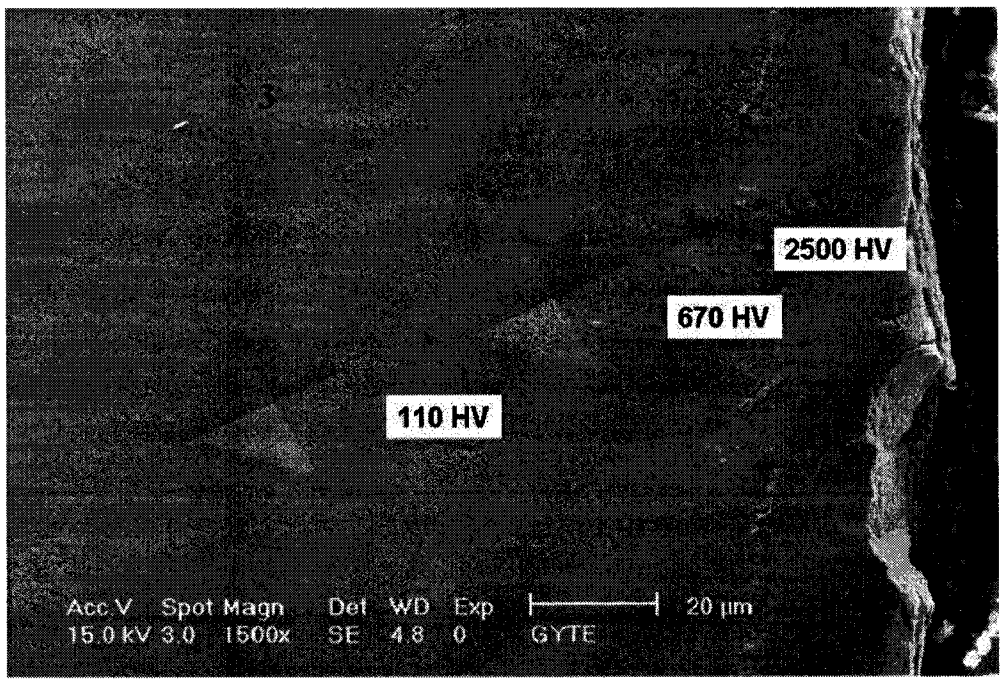

Figure 3.8: SEM image of niobium boronized at 940^{O}C for 8 hours, showing Vickers indents.

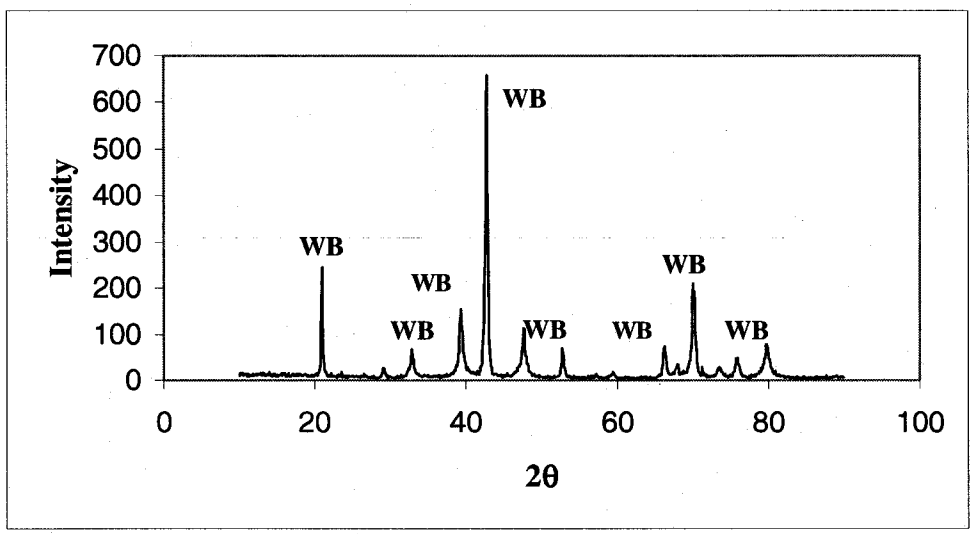

Figure 3.9: X-ray diffraction pattern showing WB formation on the surface of boronized tungsten.

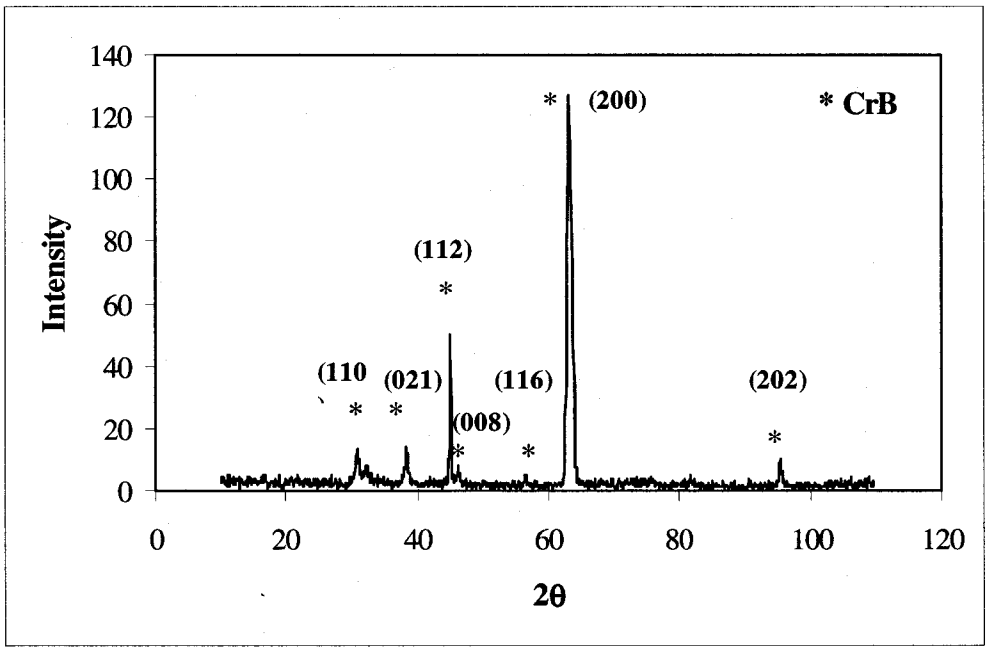

Figure 3.10: X-ray diffraction pattern showing CrB formation on the surface of boronized chromium.

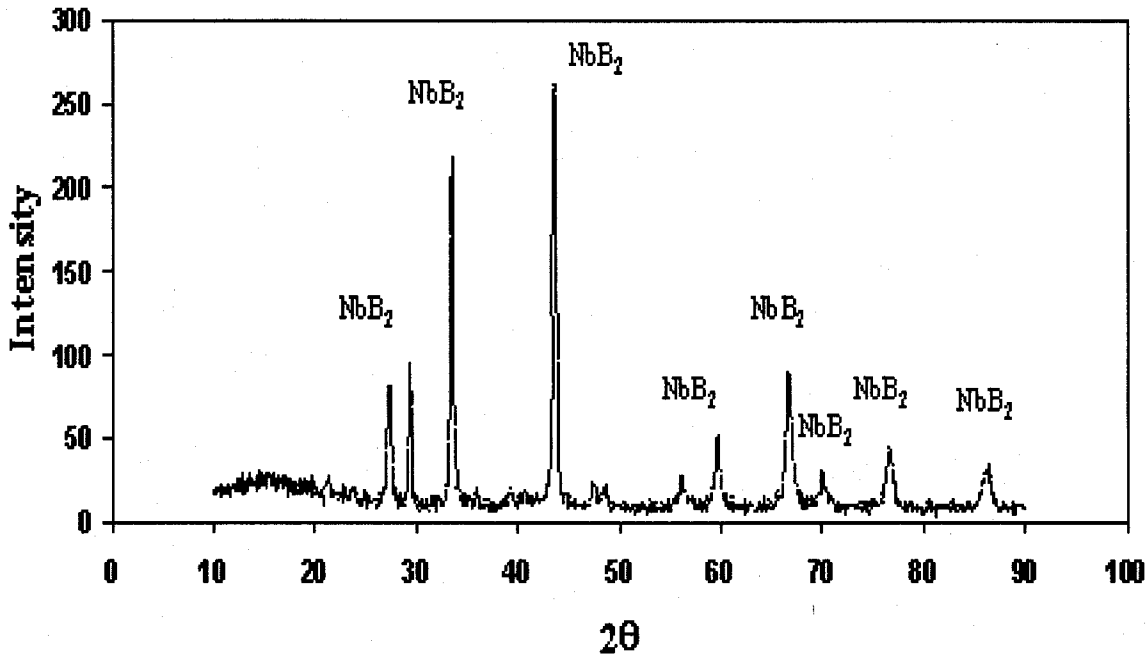

Figure 3.11: X-ray diffraction pattern showing NbB_2 formation on the surface of boronized niobium.

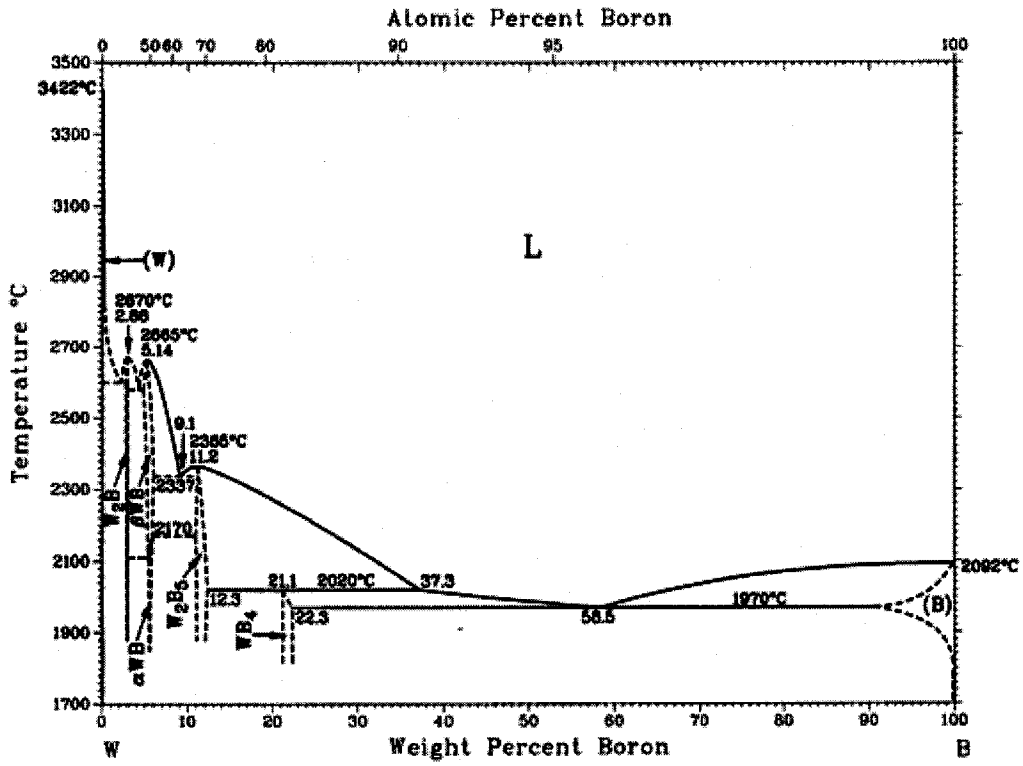

Figure 3.12: W-B binary phase diagram [3].

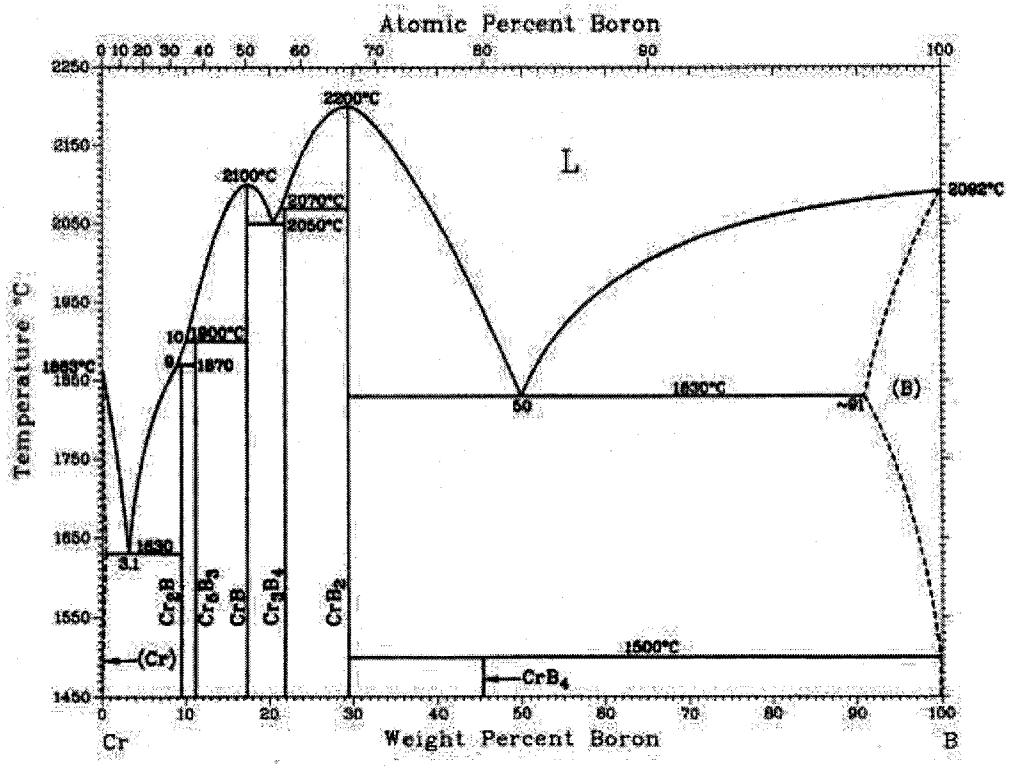

Figure 3.13: Cr-B binary phase diagram [11]

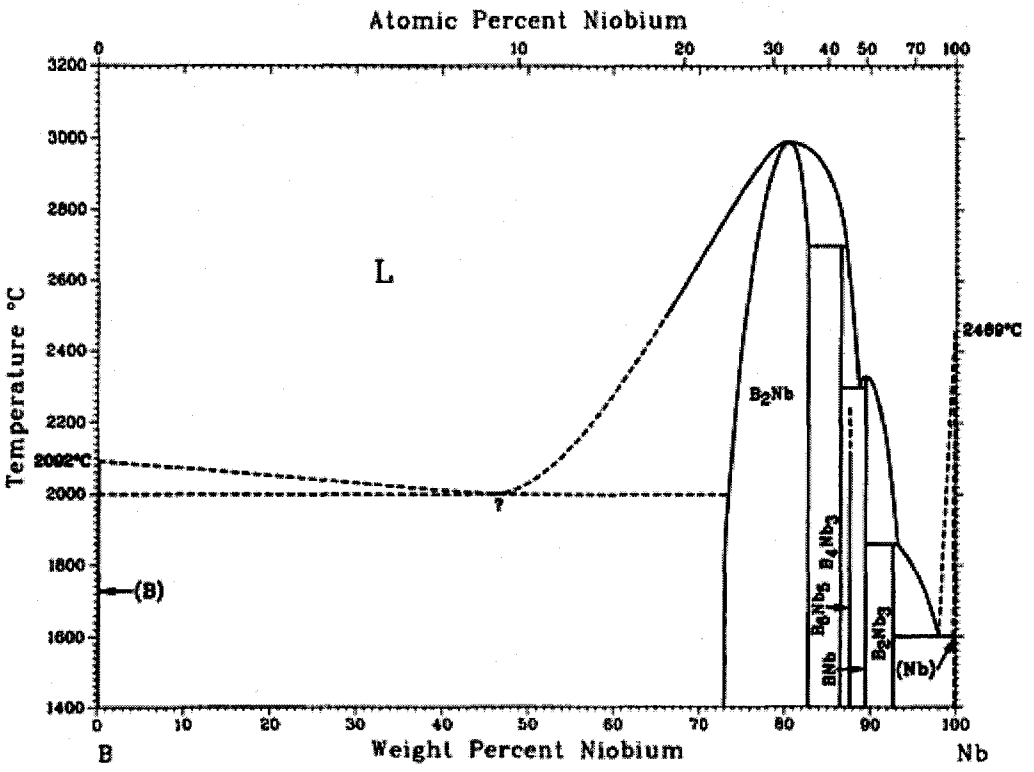

Figure 3.14: Nb-B binary phase diagram [3].

3.7 References

1 CRC Handbook of Chemistry and Physics, CRC press, 85th Edition (online) 2004-2005.

2 CRC Materials Science and Engineering Handbook, CRC press, 3rd Edition (online) 2005.

3 ASM Handbook, ASM International, Online Edition 2005.

4 I. Ozbek, H. Akbkulut, S. Zeytin, C. Bindal, A. H. Ucisik, "The characterization of borided 99.5% purity nickel" Surface and Coatings Technology 126 2000 p166-170.

5 S. Sen, I. Ozbek, U. Sen, C. Bindal, "Mechanical behavior of borides formed on borided cold work tool steel" Surface and Coatings Technology 135 (2-3) 2001 p173-177.

6 I. Özbek, B. A. Konduk, C. Bindal, A. H. Ucisik, "Characterization of borided AISI 316L stainless steel implant" Vacuum 65 (3-4) 2002 p521-525.

7 K. Genel, I. Ozbek, C. Bindal, "Kinetics of boriding of AISI W1 steel" Materials Science and Engineering A 347 (1-2) 2003 p311-314.

8 A. H. Ucisik, C. Bindal, "Fracture toughness of boride formed on low-alloy steels" Surface and Coatings Technology 94–95 1997 p561–565.

9 Y. V. Dzyadykevich, L. I. Kytskay, "Improving the oxidation protection of niobium and tantalum by the use of multilayer coatings." Journal of the Minerals, Metals & Materials Society 49 1997 p30–31.

10 H. J. Hunger, G. Trute, "Boronizing to produce wear resistant surface layers" Heat Treatment of Metals 21 (2) 1994 p31-39.

11 ASM Handbook, Volume 03: Alloy Phase Diagrams. ASM Metals Handbook Series, ASM International p81.

Chapter 4

Experiments

The measurement of friction is crucial in surface sciences. Friction plays a major role in surface design at all levels from micro levels to nano levels. It has prime importance in designing the biocompatible long lasting implants, as friction and wear are

the modes of failure of these materials. Commercially there are many types of equipment available to study these properties of materials. Wide ranges of experiments were conducted in the present investigation. Various equipment was used to characterize and analyze the surfaces. The equipment and experimental conditions are discussed here.

4.1 Sample Preparation

All the refractory metals and their boronized counterparts were cleaned ultrasonically, using an acetone bath, for 10 minutes before surface roughness measurements. The samples were made flat using putty clay before taking the surface profile. These samples were used for friction and wear tests after profile measurements.

To study friction-induced phase transformation, pure aluminum was cut to dimensions of 10 mm x 10 mm and cleaned ultrasonically with acetone to make sure that there were no foreign particles sitting on the surface. A copper pin was used to slide against the aluminum. The pin was also cleaned ultrasonically with acetone for about 10 minutes. The friction-induced hardening was studied for pure aluminum and copper. The samples were cleaned as discussed earlier.

The debris formed during various friction and wear tests consisted of fine particles. The debris was collected for analysis. The debris of CrB, pure Cr, and debris formed during Al-Cu sliding were collected in plastic ampoules containing alcohol and dispersed by placing them in a sonicator for 10 minutes. A few drops of the dispersed debris were applied to carbon stabilized Formvar-coated 400 mesh copper grids. The

alcohol was allowed to evaporate, leaving behind particles of a wide range of sizes and shapes. The mounted samples were then analyzed using transmission electron microscopes (TEM), JEOL 1200 (tungsten filament, 100 kV operating voltage) and JEOL 2010 (LaB_6 filament, 200 kV operating voltage).

The samples were placed on the sample puck for surface characterization using AFM without any preparation. The advantage of using AFM to study wear mechanisms is that sample preparation is not essential. The specimen was pasted to the sample puck using adhesive tape.

For element mapping using FE-SEM, the samples were used as-tested condition.

4.2 Universal Micro-Tribometer (UMT)

The Universal Micro-Tribometer is manufactured by the Center for Tribology, CETR, in Mountain View, CA, USA. This equipment can be used for tribological testing of both metallic and nonmetallic materials. It can be used with solid and liquid lubrication. The equipment can be used in different modes of operation:

- Pin-on -disc
- Pin-on-V-block
- Block-on-ring
- Disc-on-disc (flat-on-flat)

4.2.1 Operating Principle

The specimen can be fixed on both the parts (i.e. upper and lower) of the UMT. The upper part moves in a vertical linear motion with a travel length of 150 mm. The precision spindle can rotate the lower specimen with a speed of 0.001 RPM to 5000 RPM. The lateral and vertical forces are recorded by strain gauges. The lateral force can be measured in two directions on the same plane. The vertical-force sensor provides feedback to the vertical motion controller to apply the vertical constant load. It has an automatic motor controller and a data acquisition operated using PC-based software. Figure 4.1 shows the photograph of a Universal Micro-Tribometer with test configuration in zoom [1].

4.2.2 Test Conditions and Test Measurements of Materials

Friction and wear tests in reciprocating pin-on-disc configurations were conducted using this equipment. The upper pin was a steel ball with a diameter of 5 mm. The lower specimen was cylindrical (6.3 mm diameter and 6 mm high) and made of boronized refractory metals. The tests were conducted on the flat face of the cylinders.

The face of the cylinder was made horizontal and fixed with adhesive glue on the bottom stage of the UMT. The tests were conducted in two steps. In step one, the load was 2N for 120 seconds to achieve the uniform friction; then continued in the second step, the contact load was 5N for 3600 seconds. The reciprocating amplitude was 4 mm, which

formed a wear track of the same length. The tests were conducted at 100 RPM at room temperature. The relative humidity of the room was 55-60%.

After the wear test, the debris formed was collected for further analysis. The software was configured with the equipment. It plotted the coefficient of friction and the change in vertical position of the steel ball with time. The reduction of the vertical position of the steel ball represents ball and test specimen wear.

The materials tested using this instrument were:

- Boronized tungsten (WB)
- Pure tungsten (W)
- Boronized tantalum (TaB)
- Boronized niobium (NbB)

4.3 Tribox 2.7 (CSM)

Tribox 2.7 is a pin-on-disc tribometer manufactured by CSEM S. A., Nauchatel, Switzerland. It can be used in two different configurations: reciprocating and rotating.

4.3.1 Operating Principle

The top part is a stiff lever on which a pin can be mounted. This lever is designed as a frictionless force transducer. The bottom plate is movable (rotating and/or oscillating). Frictional forces act between the pin and the sample as a result of either

rotatory or oscillatory motion. They are measured by deflections of the lever. Measurement of friction and wear can be conducted with a simple principle. Almost all types of solids can be used as a sample specimen. The test can be performed with different variables like time, contact pressure, velocity, temperature, humidity, lubricants, etc.

The equipment is semi-automatic and controlled with PC-based software. The data can be collected through a data acquisition system on the PC. The software can plot the friction coefficient against speed, time, or number of cycles. Data acquisition can record the temperature data as well. The software can calculate separately the wear rate of the ball and the sample. It can also calculate the contact stress (Hertzian).

4.3.2 Test Conditions and Test Measurements of Materials

Friction and wear tests in reciprocating pin-on-disc configurations were conducted using Tribox 2.7. The upper pin was a steel ball with a diameter of 5 mm. The lower specimens were cylindrical boronized refractory metals (6.3 mm diameter and 6 mm high). The tests were conducted on the flat face of the cylinders. The boronized chromium specimen was rectangular.

4.3.2.1 Friction Test in Dry Condition

The face of the cleaned rectangular specimen of pure Cr and CrB was made horizontal and fixed with a clamp on the movable bottom part of Tribox. The tests were conducted at 5N for 3600 seconds. The reciprocating amplitude was 8 mm, which formed

a wear track of the same length. The tests were conducted at 100 RPM at room temperature. The relative humidity of the room was 60-65%.

The debris formed during the test was collected for further analysis. The software configured with the instrument plotted the coefficient of friction with time. The wear scar on the steel ball was observed using an optical microscope.

The materials tested using this equipment were:

- Boronized chromium (CrB)
- Pure chromium (Cr)

4.3.2.2 Friction Test in Simulated Body Fluid (SBF)

The faces of the cleaned rectangular (Cr and CrB) and cylindrical specimens of boronized refractory metals (i.e., TaB, WB, and NbB) were made horizontal and fixed with a clamp on the movable bottom part in a cup of aluminum foil that held SBF. The tests were conducted at 5N for 3600 seconds. The reciprocating amplitude for TaB, WB, and NbB was 4 mm, which formed a wear track of the same length. The reciprocating amplitude for Cr and CrB was 8 mm, which formed a wear track of the same length. The tests were conducted at 100 RPM at room temperature. The relative humidity of the room was 60-65%.

The debris formed during the test was collected for further analysis. The software configured with the instrument plotted the coefficient of friction with the time. The wear scar on the steel ball was observed using an optical microscope.

The materials tested using this equipment were:

- Boronized chromium (CrB)
- Pure chromium (Cr)
- Boronized tungsten (WB)
- Pure tungsten (W)
- Boronized tantalum (TaB)
- Boronized niobium (NbB)

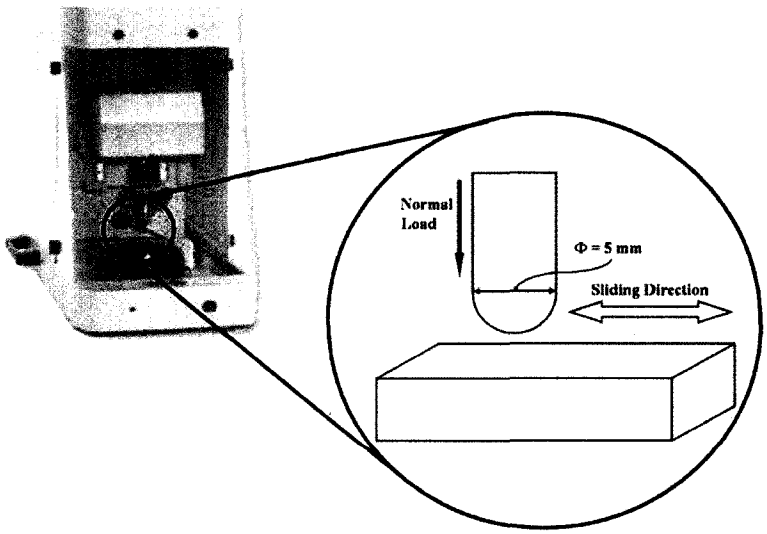

Figure 4.1: Pin-on-disk tribometer CETR [1].

4.4 Rotating Pin-on-disc Tribometer

The pin-on-disc and flat-on-disc tests were conducted using a tribometer manufactured by Ducom Triboinovators, Bangalore, India. This equipment records friction and wear during sliding contact in a dry, lubricated, controlled environment and partial vacuum. This tribometer can be used to study the friction and wear of metals, ceramics, soft and hard coatings, plastics, polymers and composites, lubricants, cutting fluids, and heat processed samples. It has PC-controlled software and a data acquisition system. The software permits measurements of RPM, wear, frictional force, and temperature. The copper flat on Al disc was tested in rotating configurations. The test was conducted at 150 RPM using a 2 kg load for 3600 seconds. The debris formed was collected for further analysis. The copper pin on copper disc was also tested in rotating configuration at the similar experimental parameters.

4.5 Surface Characterization

The wear mechanisms and surface characterization of boronized refractory metals were studied using an atomic force microscope, a profilometer, a field emission-scanning electron microscope, and a transmission electron microscope.

4.5.1 Atomic Force Microscope (AFM)

The atomic force microscope (AFM) is a member of the scanning probe microscope (SPM) family. Binning et al [2, 3] reported the first atomic force microscope. Thereafter, this equipment has been used in every field of science that involves surfaces.

The study of surfaces at the atomic level is achieved using this equipment. In the present investigation, the AFM used was manufactured by Pacific Nanotechnology, Inc. (PNI), Santa Clara, CA, USA. The following sections will cover the operating principles and modes.

4.5.1.1 Operating Principles

Forces are always present in close proximity to two physically separated solids. AFM is based on this fact. These forces are sensed using a very sensitive detector, and an image is formed. The forces measured are between the cantilever tip and the sample surface. The operating principle is similar to the stylus profiler, but in AFM a much higher resolution can be achieved.

The major parts of the AFM are: cantilever, tip, piezo system, and detector. The controlled motion (i.e., in the X-Y plane and in the Z direction) in the piezo system was achieved using an electromechanical transducer. The AFM utilized in the present investigation is equipped with piezoelectric ceramic. The scanning probe was made of silicon from the same manufacturer. While scanning the sample, a constant force was applied on the cantilever using a feedback mechanism. Figure 4.2 shows the schematic of different parts of the AFM, the functions of which are listed here [4]:

- Z: Facilitates linear vertical motion (coarse).
- T: Facilitates linear X-Y motion.
- X-P & Y-P: Piezoelectric transducer to scan the surface in raster motion.

- FC: Force Sensor.
- Z-P: Piezoelectric ceramic to move in vertical direction as a response to the cantilever deflection (fine).
- FCU: Feedback mechanism.
- SG: Raster scan controller to help to form image.
- CPU: Computer control and data acquisition.
- F: Body of the AFM.

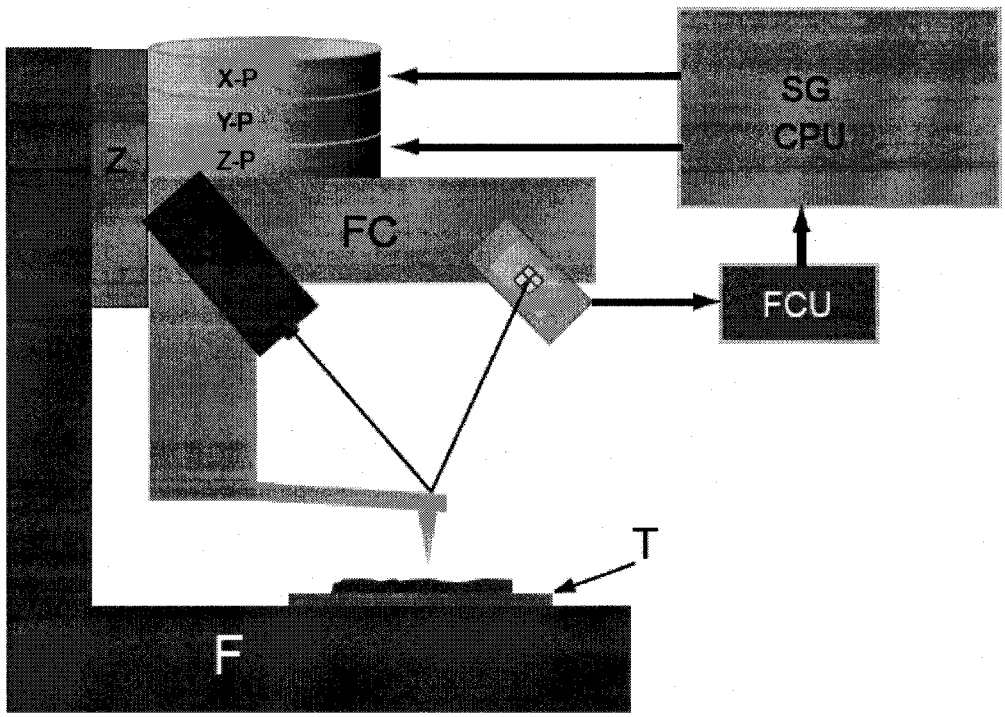

Figure 4.2: Major components of AFM [4].

One of the advantages of using an AFM image over a conventional microscope image is that AFM provides images revealing three dimensions. Very high resolutions can be achieved in the X-Y plane by using the sharper tip. The vertical resolution depends on the noise coming from the surroundings such as acoustic and thermal vibrations. The floor vibrations can also contribute noise and deteriorate the vertical resolution [4]. Figure 4.3 shows the AFM equipment used in the present study.

4.5.1.2 Imaging Modes

Images can be formed by operating the AFM in different modes; i.e., contact mode and non-contact mode. In contact mode, the cantilever tip touches the sample and scans the surface in raster motion. The feedback system maintains constant force between the tip and the sample. The deflection of the cantilever tip was measured. In non-contact mode, the cantilever tip oscillates near the surface of the sample. The change in amplitude of the oscillations of the tip was measured.

The materials' properties can also be studied by using material-sensing modes. These modes are operated simultaneously with contact mode or non-contact mode operation. There are two different materials-sensing modes. One is the phase detection mode, in which an AFM cantilever is oscillated vertically near its mechanical resonance frequency (non-contact mode). When the tip comes very close to the sample surface, the amplitude of the cantilever's frequency is reduced. This change in amplitude is measured and used to track changes in the surface topography and roughness of the sample. At the same time, the AFM tip experiences the regions of different composition and the phase

change on the surface. The phase change occurs in the oscillating frequency with respect to its initial frequency. This change is measured and recorded. This change in phase is very sensitive to variations in material properties, including surface stiffness, elasticity, and adhesion. These phase shifts are used to form an image. The phase images facilitate quantitative analysis and interpretation [5].

The other material-sensing mode is also called lateral force microscopy (LFM). During the contact mode of AFM scanning, when the probe scans over the surface by touching the tip continuously on the surface, surface friction and topologic features produce the forces and twist the cantilever. These lateral deflections of the cantilever are sensed by the photo detector and are used to form a lateral force image. LFM is useful in the study of surfaces that have variations in friction values. As both surface friction and topology can cause lateral deflection, a careful study of the topological image and the LFM image is necessary [6].

4.5.1.3 Scan Modes, Conditions and Materials Scanned

The finer-scale analysis of wear mechanisms was conducted using the atomic force microscope (AFM). The AFM was used to image the surface profile and its details at high resolution with high accuracy. In contact mode, the raw data of each scan were produced using four channels (Z- HGT, Z-SEN, Z-LR, and Z-ERR). In non-contact mode, the raw data of each scan were produced using four channels (Z- HGT, Z-SEN, Z-DEM, and Z-ERR). The scans were taken at different sizes from an area of approximately 75μm

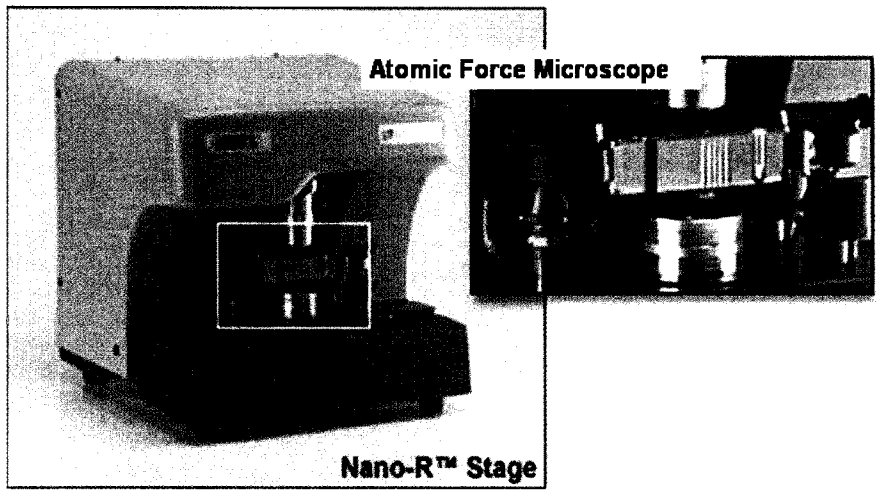

Figure 4.3: Atomic force microscope (PNI) [7].

x 75μm down to 0.75μm x 0.75μm. The maximum scan size depended on the linearization parameters (for details, refer to the instrument manual). The Z-HGT signal was used to study morphology and wear mechanism. (The Z-HGT images are referred as "Morphology Images" in this dissertation.) The lateral displacement signal (Z-LR) was used to study the frictional response of the surface to the cantilever tip. The images formed using this signal are referred to as frictional force microscopy images (FFM images). The Z-ERR signal was used to trace the noise in the scan and to select a good quality image for analysis. The Z-SEN signal image was used to compare the quality with the Z-HGT image. In general, the Z-HGT and Z-SEN signal images look alike. Therefore, for analysis purposes only, two types of images (i.e., morphology images and frictional force microscope images) were used. In non-contact mode, the phase image, instead of the FFM image, was obtained. The materials scanned in contact mode are listed here:

- Boronized tungsten (WB): Surface, wear track, and debris.

- Pure tungsten (W): Surface, wear track, and debris.
- Boronized tantalum (TaB): Surface, wear track, and debris.
- Boronized niobium (NbB): Surface, wear track, and debris.
- Pure copper (Cu): Surface, wear track, debris, and Vickers indents.

The surfaces, debris, and wear tracks of the pure refractory metals and their boronized counterparts, which were tested using SBF as a lubricant, were scanned in non-contact mode. The Vickers indents were also scanned in non-contact mode.

4.5.2 Field Emission Scanning Electron Microscopy (FE-SEM)

The worn surface analysis was done to study the chemical composition of the materials transfered from the ball and the boronized surface for WB. The elemental mapping was done on the wear track to trace the material transfer using a Field Emission Scanning Electron Microscope (Leo VP1530 FE-SEM). The secondary electron image was captured. The microscope was used at 15 KV, and the working distance was 9 mm.

4.5.3 Transmission Electron Microscopy (TEM)

The high-resolution imaging and chemical composition study was conducted using transmission electron microscopes JEOL 1200 and JEOL 2010. JEOL 1200 has a tungsten filament as an electron source, and the microscope was operated at 100KV. JEOL 2010 has LaB_6 filament as electron source and the microscope was operated at 200KV. Bright field images were taken at different magnifications. The EDS spectrum was collected at different places on the CrB sample. The selected area diffraction (SAD)

pattern was collected. For Al-Cu debris the bright field images and the SAD pattern were collected.

4.5.4 Profilometer

Surface roughness is defined as the finer irregularities of the surface texture that usually result from the inherent action of some production process. The surface roughness of boronized refractory metals was studied by using the Talysurf profilometer (Taylor Hobson) with a diamond tip diameter of 5μm. The scan length was 4mm. The tests were conducted at three different places on the surfaces of the coated samples. The reported Ra value is the average of these three values with standard deviation.

4.6 Vickers Indenter

The Vickers indents were used to study the stress induced hardening using atomic force microscopy. The microhardness tester (Buehler, Micromat II) was utilized. Vickers indentation was used to produce the deformation on the pure Cu surface. The indents were made on a copper surface at different loads of 1000, 300, 50, and 25 gms. The load was applied for 15 seconds.

4.7 References

---

1 http://www.cetr.com. The Center for Tribology, CETR, Mountain View, CA, USA, last accessed Jan 2005.

2 G. Binning, H. Rohrer, C. Gerber, E. Weibel, "Surface studies by scanning tunneling microscopy" Physical Review Letters 49 1982 p57.

3 G. Binning, C. F. Quate, C. Gerber, "Atomic force microscope" Physical Review Letters 56 1986 p930.

4 Nano –R™ AFM user's manual, 2004.

5 http://www.molec.com/apps_imagingmodes.html, Molecular Imaging, last accessed Jan 2005.

6 R. Overney, E. Mayer, "Tribological investigations using friction force microscopy" MRS Bulletin May 1993 p26-34.

7 http://www.pacificnano.com, Pacific Nanotechnology, Inc. (PNI), Santa Clara, CA, USA, last accessed Jan 2005.

Chapter 5

Friction-Induced Phase Transformation

5.1 Background

During sliding, structural as well as chemical changes occur between the interfaces of two sliding bodies. G. Beilby reported in his book that materials polishing produces a thin film on the surface that is different from its parent material. In the tribology community, this layer is known as the "Beilby Layer" [1]. After G. Beilby, Bowden and Hughes mentioned that this layer was amorphous and formed due to the rapid solidification of locally- melted asperities [2, 3]. After their work there were many efforts made to understand and to experimentally prove the formation of the Beilby layer on the sliding surface. It was shown that during sliding the nano-crystalline materials

could develop [4, 5]. Recently, Molecular Dynamics (MD) simulations have been done on the formation of nano-crystalline and amorphous materials during sliding that are in close agreement with experimental observations [6, 7, 8, 9]. Fu et al. [7] reported the sliding behavior of a Zr–Ti–Cu–Ni–Be bulk metallic glass (BMG) in vacuum and in air. In both environments, sliding produced a work-softened layer where the plastic deformation was highest. The annealed nanocrystalline BMG specimen forms the amorphous layer during sliding. Furthermore, XRD studies of the resulting debris indicated that the material re-amorphized [7].

Erdemir et al. studied the frictional behavior of the Diamond-like-coating (DLC) [10, 11]. They found that the ultra-low friction was due to the graphite phase formed on the surface during sliding. This graphite is the transformed phase of DLC due to friction.

A recent investigation by Prof. J. T. Dickinson's group observed the stress-induced dissolution. They used a scanning force microscope (SFM) probe tip to provide frictional stimulus. In this study, they found localized dissolution of calcite ($CaCO_3$) and brushite ($CaHPO_4 \cdot 2H_2O$) surfaces near the SFM probe tip. It was dramatically increased by applying stress with the tip. They showed that a SFM tip can also be used to nucleate, accelerate, and control deposition along step edges on brushite surfaces in supersaturated aqueous solutions [12, 13]. In their report they showed that friction induced layer-by-layer growth at step edges on the {010} cleavage surfaces of brushite ($CaHPO_4 \cdot 2H_2O$). They also showed that the growth rates are highly sensitive to the crystallographic orientation of the steps [14].

Guruzu et al. [15, 16, 17, 18] studied the friction induced phase transformation in the Si-Ga sliding system by using a pin-on-disk sliding contact configuration for their tests. The frictional force provides the mechanical stimulus for phase transformation to occur. They found that the nano crystals of Si-Ga with hypereutectic composition were formed on a silicon surface. These nano crystals formed on the sliding surfaces are shown in Figure 5.1.

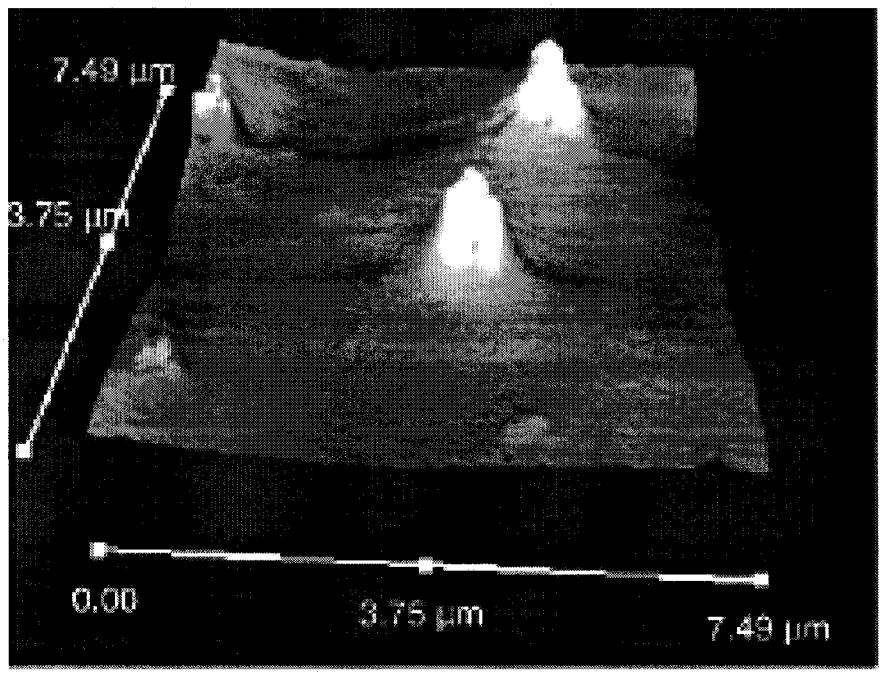

Figure 5.1: Nano crystals grown on Si surface during sliding [16, 17, 18, 19].

This chapter further investigates the phase transformation taking place during sliding conditions. Differently from previous studies, this research focuses on the refractory and active metals due to their wide range of applications. Detailed materials properties and experimental procedures have been discussed in Chapter 3 and Chapter 4.

In brief, three different test configurations were used for friction and wear tests for different materials pairs.

1. Reciprocating pin-on-disc friction and wear tests were conducted for boronized refractory metals (CrB and TaB). The pin material was a bearing ball and the disc was made of one of several boronized refractory metals.
2. The rotating flat-on-disc test configuration was used for the Cu and Al pair. The top flat surface was Cu and the bottom rotating disc was Al.
3. The rotating pin-on-disc configuration was used for pure Cu. Both the pin and the disc were made of Cu.

The following sections will provide a detailed description of the experimental results and their possible interpretations.

5.2 Experimental Results

5.2.1 Boronized Chromium

A TEM image of the debris collected and analyzed is shown in Figure 5.2. This TEM micrograph showed debris with very fine particle size (<50nm). Most of the particles of nano-sized debris were clustered together due to the adhesive interaction among them. The inset in Figure 5.2 shows the selected area diffraction pattern (SAD), revealing the crystal structure of these nano sized debris particles.

5.2.2 Boronized Tantalum

Figures 5.3a and 5.3b are the topological image and FFM image of boronized tantalum observed using the contact mode of AFM, respectively. After the wear test, the topological and FFM images of the worn track are shown in Figures 5.4a and 5.4b. The arrow shows the reciprocating direction during the test.

5.2.3 Aluminum-Copper Sliding System

The topology and phase images of the Cu surface were observed using the non-contact mode of the AFM shown in Figures 5.5a and 5.5b, respectively, taken at lower magnifications. The topology and phase images of the same surface are shown in Figures 5.6a and 5.6b, respectively, at higher magnifications.

Figures 5.7a and 5.7b, respectively, show the topological and FFM images of the copper wear track formed after the wear test in the contact mode of the AFM. Figure 5.8 shows the TEM micrograph of debris and the insert of the selected area diffraction pattern (SAD) taken on the debris surface. The selective area diffraction pattern (SAD) with possible nano nuclei is shown in Figure 5.9.

5.2.4 Copper-Copper Sliding System

The topological and phase images of the disc specimen are shown in Figures 5.10a and 5.10b, respectively. The topology and FFM images of the worn disc surface using the contact mode of the AFM are shown in Figures 11a and 11b, respectively.

Figure 5.2: TEM image of debris of CrB; inset is the SAD pattern.

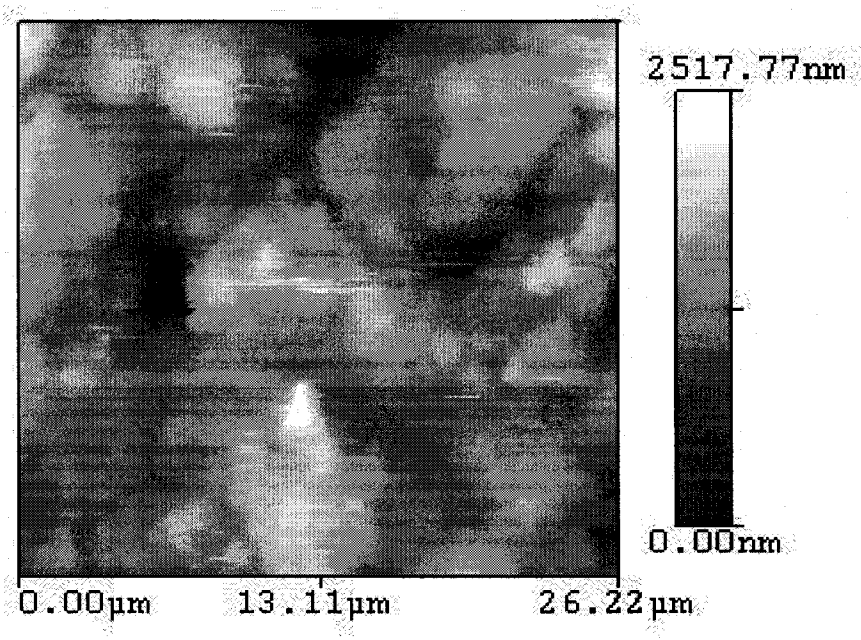

Figure 5.3: a) Topological image of TaB coating before wear.

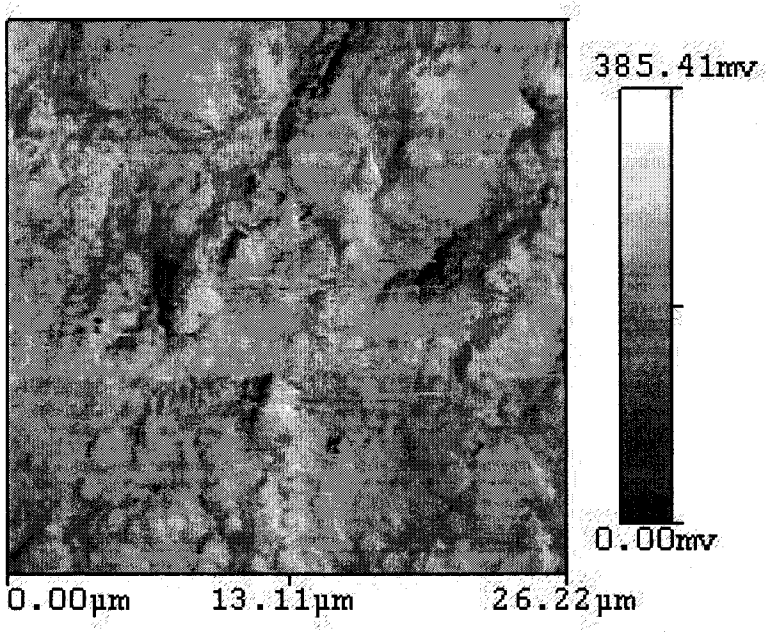

Figure 5.3: b) FFM image of TaB coating before wear.

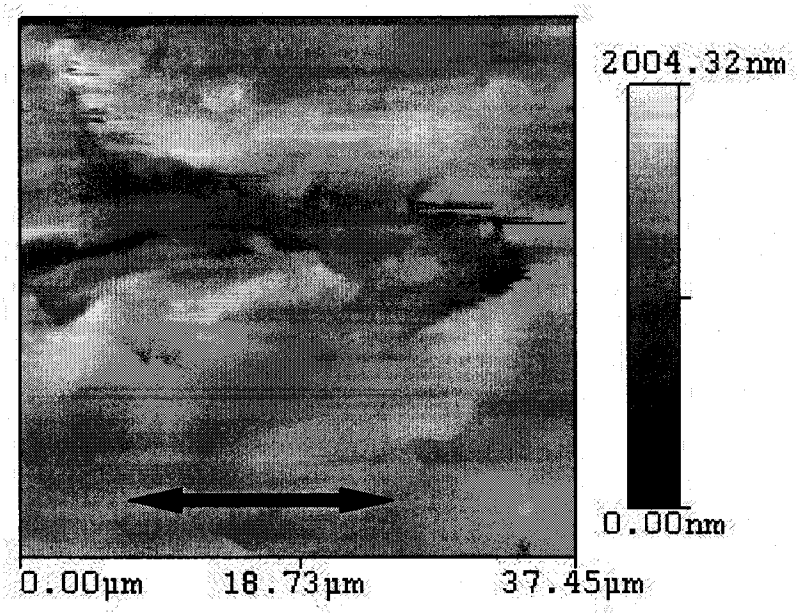

Figure 5.4: a) Topological image of TaB coating after wear.

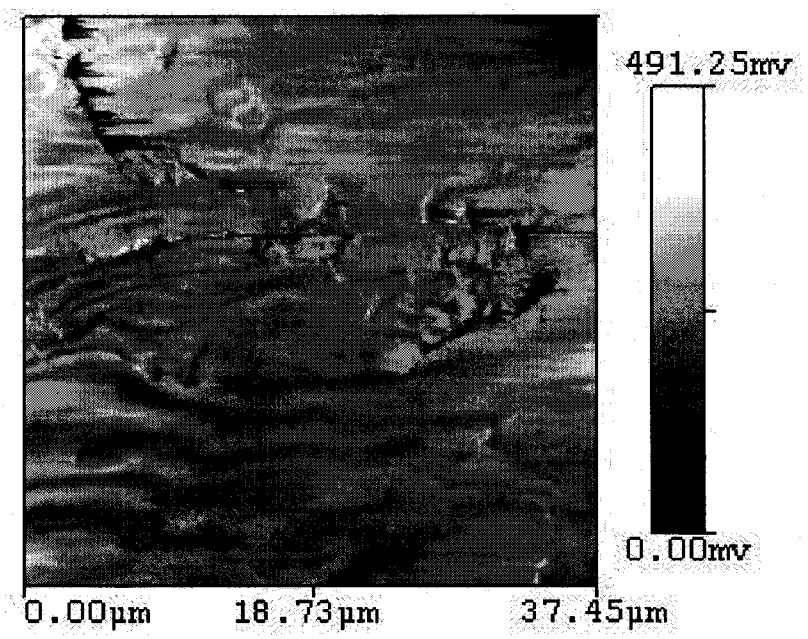

Figure 5.4: b) FFM image of TaB coating after wear.

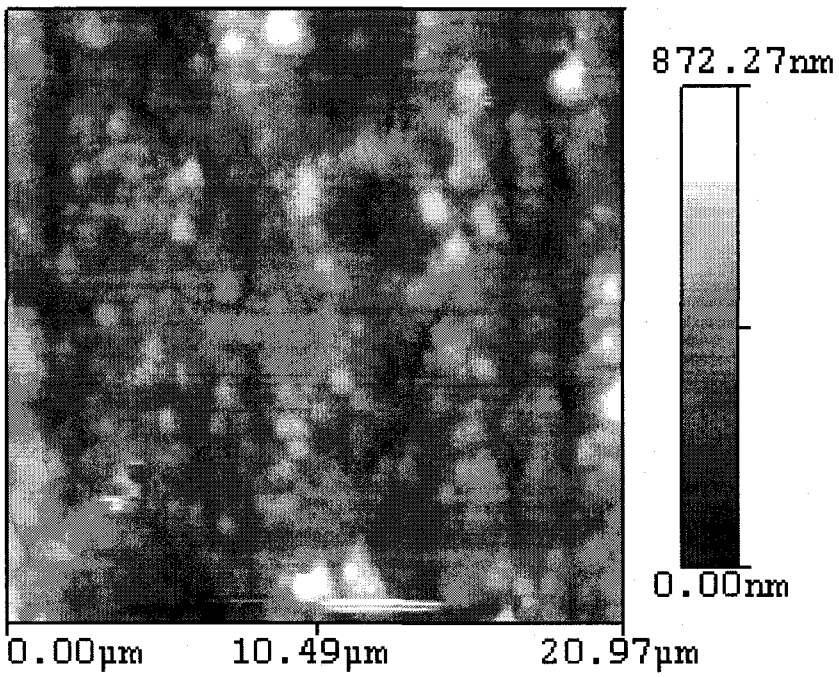

Figure 5.5: a) Topological image of Cu surface before wear.

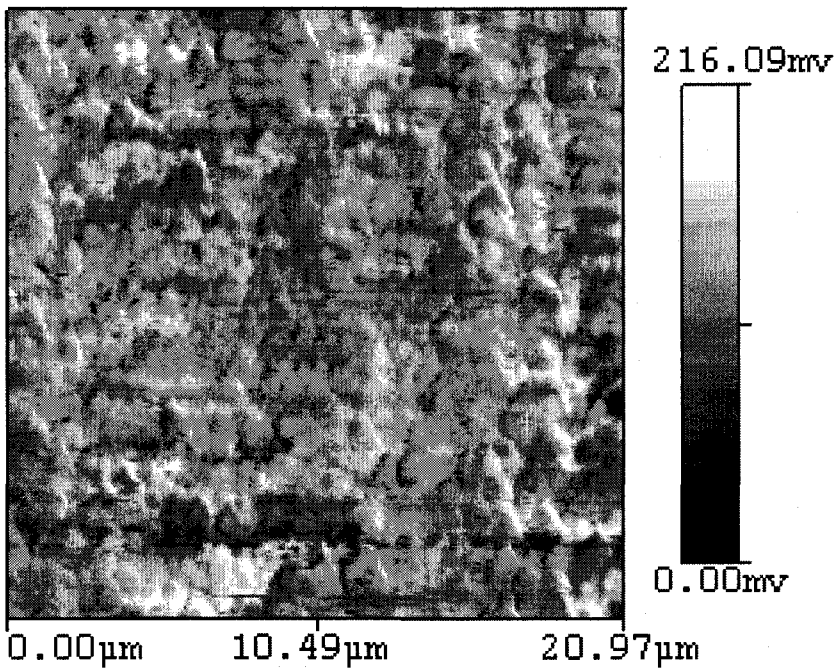

Figure 5.5: b) FFM image of Cu surface before wear.

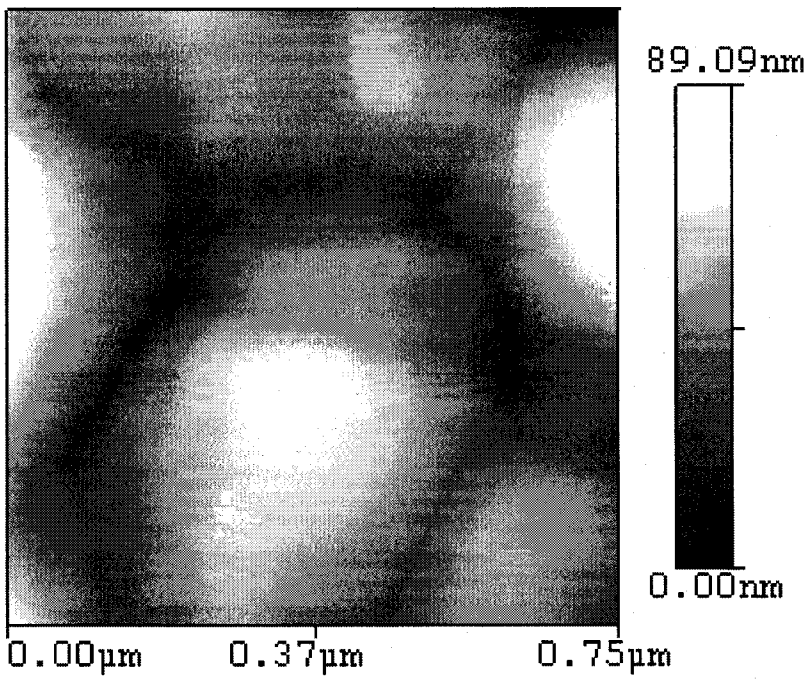

Figure 5.6: a) Topological image (at high magnification) of Cu surface before wear.

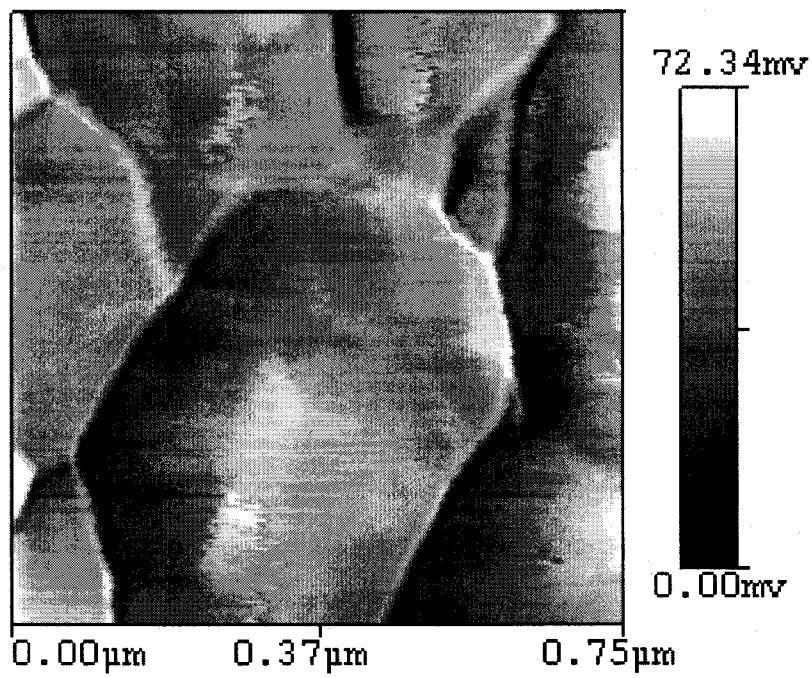

Figure 5.6: b) Phase image (at high magnification) of Cu surface before wear.

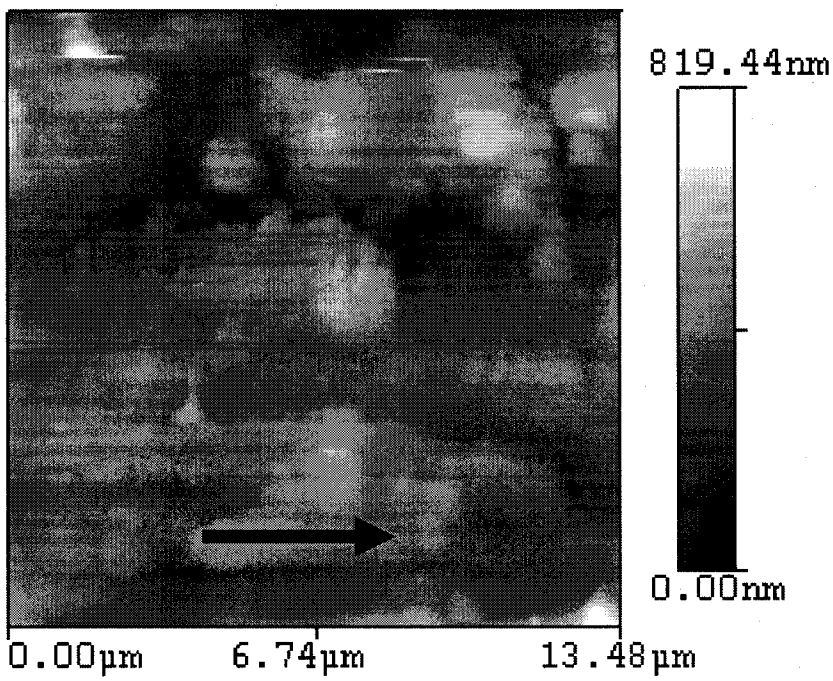

Figure 5.7: a) Topological image of Cu surface after wear.

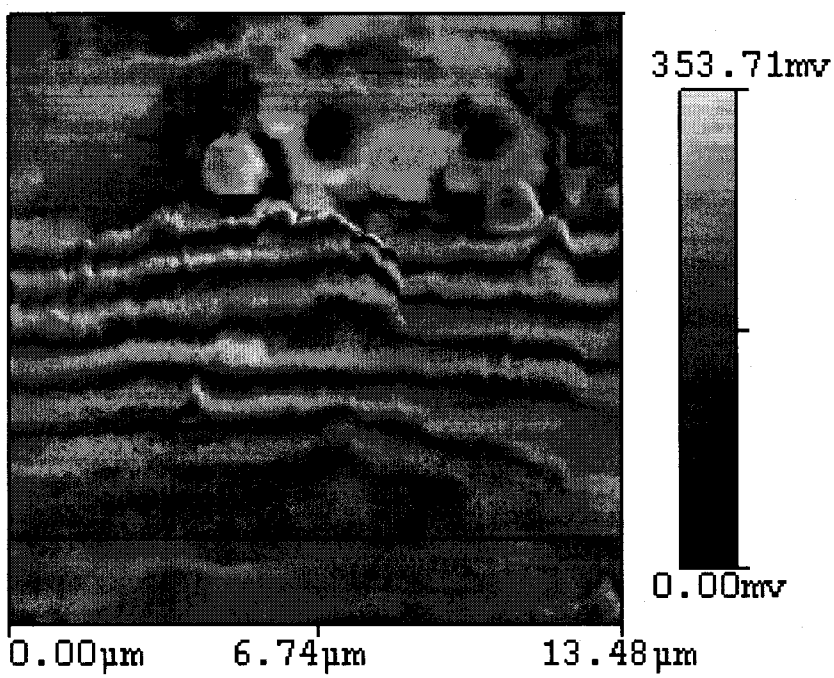

Figure 5.7: b) FFM image of Cu surface after wear.

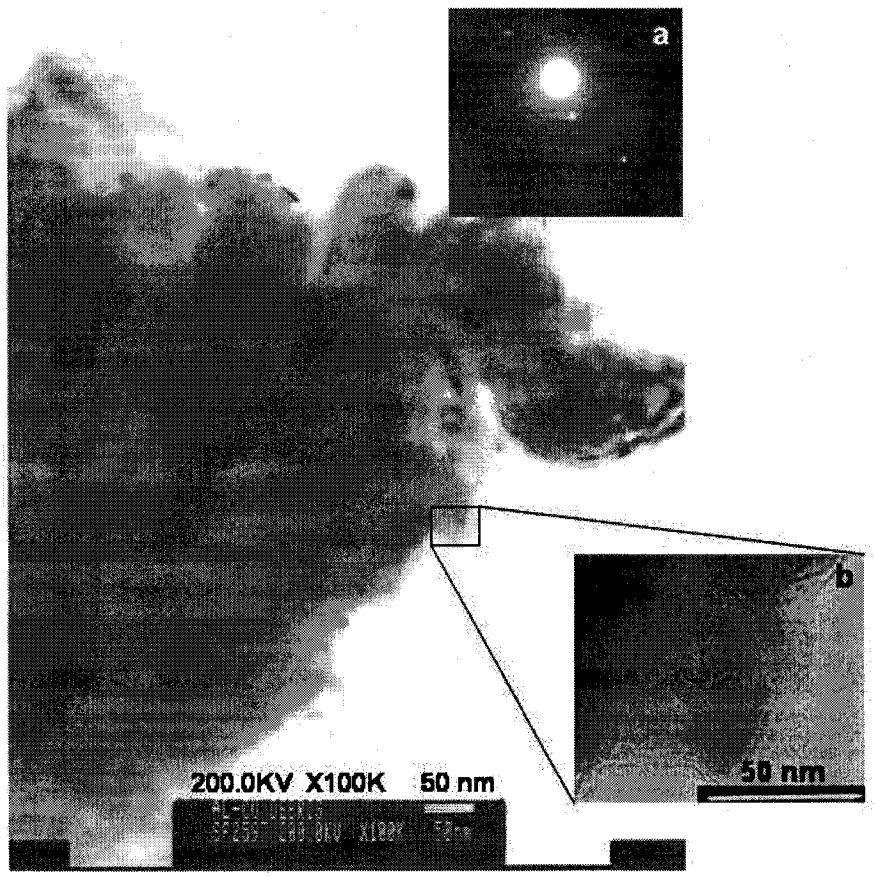

Figure 5.8: TEM micrograph of Al-Cu Debris.

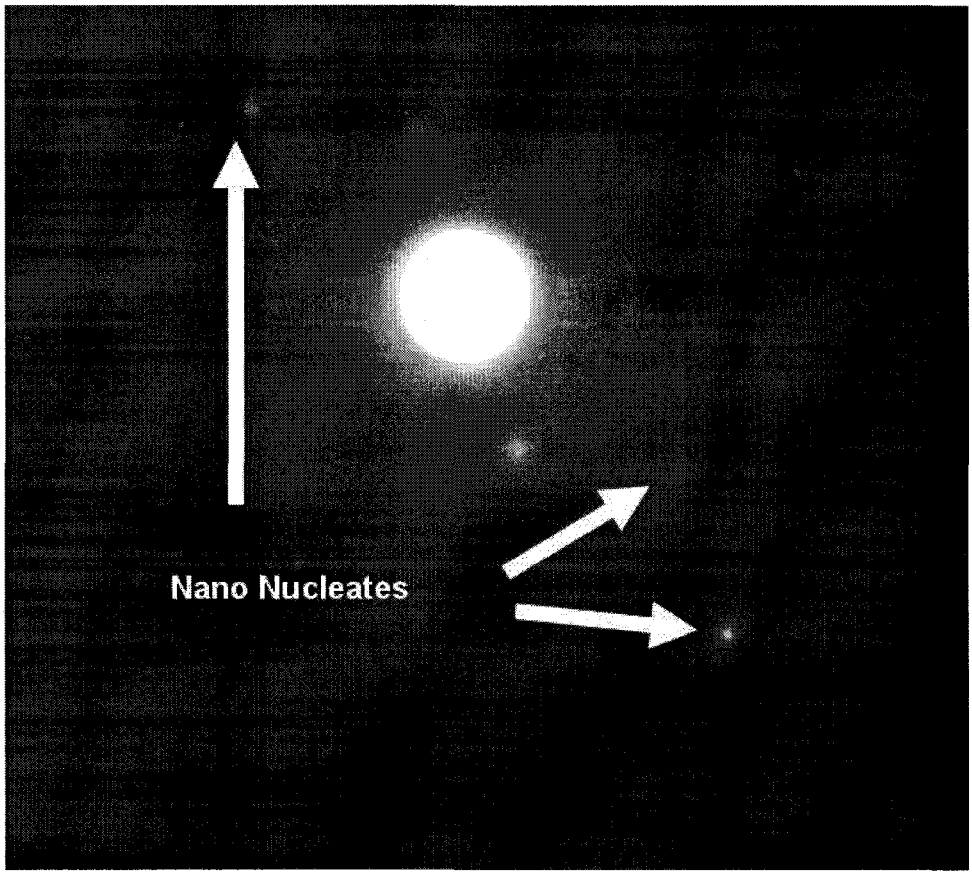

Figure 5.9: Selective area diffraction of Al-Cu debris.

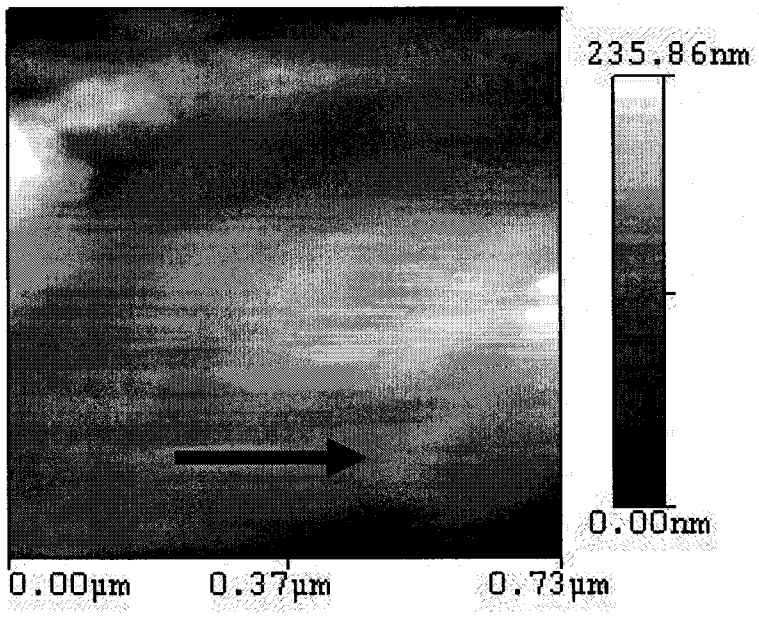

Figure 5.10: a) Topological image of Cu surface after wear (non contact mode).

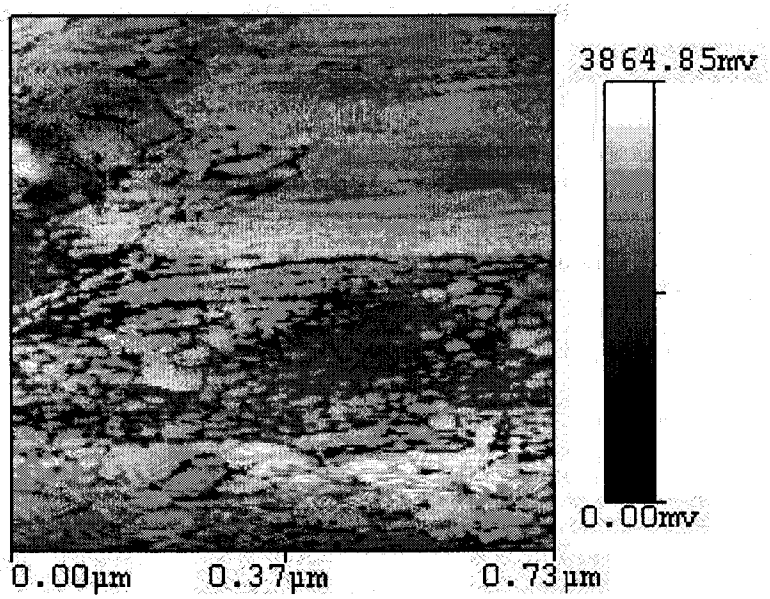

Figure 5.10: b) Phase image of Cu surface after wear.

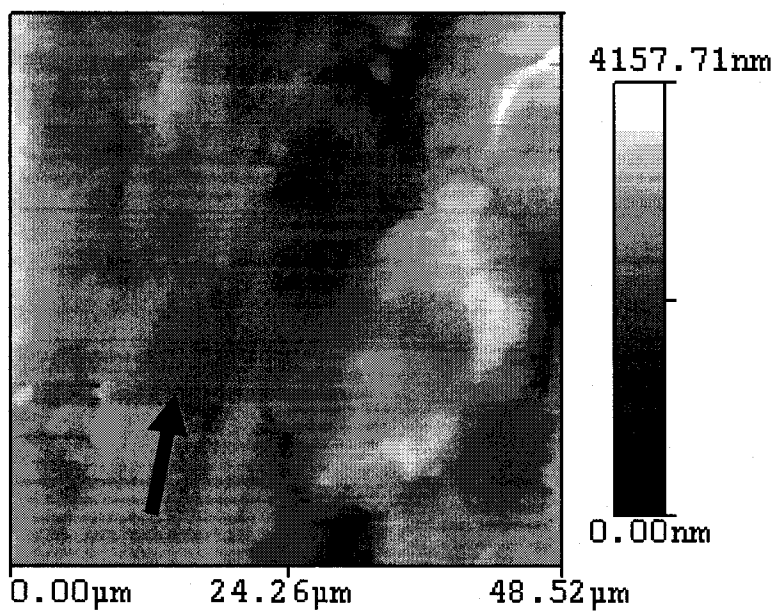

Figure 5.11: a) Topological image of Cu surface after wear (Cu-Cu sliding).

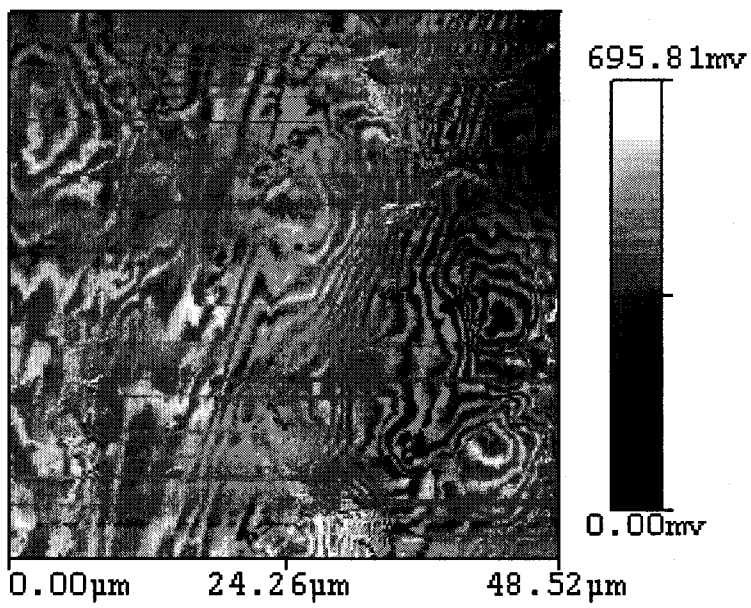

Figure 5.11: b) FFM image of Cu surface after wear (Cu-Cu sliding).

5.3 Discussion

5.3.1 Sliding Contacts

The materials behavior and the surface changes at the interface during the sliding of two different surfaces is a very complex process. The surface wear mechanisms were already discussed in Chapter 2. Adhesive forces play an important role in the wearing and tearing of the material which was discussed earlier and shown in Figure 2.1.

A study of the temperature increase at the interface during sliding has been conducted by many authors [19, 20, 21]. The temperature increase is sudden at the asperities. It can reach the melting point of the mating surfaces. This temperature is termed the flash temperature.

Materials used in tribological applications are mostly elastoplastic in nature. Due to continuous load and frictional forces on the surface, these materials deform plastically. The subsurface deformation, the crack nucleation, and growth under the surfaces are explained by Suh [22]. In a separate report on delamination wear, he discussed the dislocation movements under the surface [23].

In summary, during sliding materials undergo different processes such as temperature rise, plastic deformation, and subsurface deformation by movements of defects.

Debris formation during sliding is also a complex phenomenon. There are different possibilities for the debris particle once it separates from the parent materials.

These possibilities are explained in Figure 5.12. The detached particle can adhere to the other surface by adhesive interaction, which is represented by "a." It can react with the surrounding atmosphere and get oxidized depending upon its reactivity with oxygen; this is represented by "b." It can roll in between two sliding surfaces as a third body which is represented by "c." If the third body rolling debris particle is hard, it will damage the softer surface and form a groove on it. This is represented by "d." The deformation of the mating surface that can occur during sliding is represented by "e." The debris formed during this process has a very complex structure. Figure 5.13 shows the schematic of the debris particle.

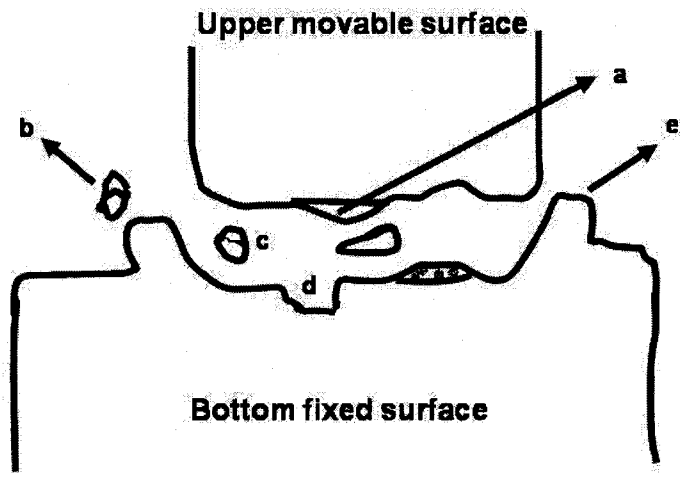

Figure 5.12: Different possibilities of materials behavior during sliding.

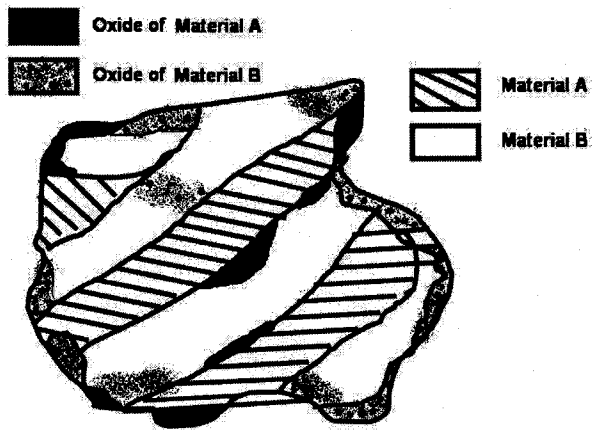

Figure 5.13: Schematic of debris particle formed during sliding.

5.3.2 Formation of Amorphous State During CrB-Bearing Ball Sliding

During the friction and wear tests, the bearing ball was slid against the chromium boride coating. The major constituents of the bearing ball are Fe and C. It was found that the CrB surface was worn mainly by abrasive wear and fracture. The detailed wear mechanisms are discussed in Chapter 7. The SAD pattern in Figure 5.4 showed no diffraction from the crystallographic planes, indicating the resulting phase is amorphous.

Hume Rothery explained the formation of stable binary phases. He gave four different criteria to form binary alloys [24]. Those are:

a. The ratio of atomic radii of constituent should not exceed 15%.
b. The crystal structure of both the metals should be the same.
c. Their electro negativity should be close.
d. The two metal ions must have same valance.

Most of the binary alloy systems follow these rules.

Davis [25] and Giessen [26] have reported that the atomic radii of two constituent metals are important parameters that define the amorphous structure. The difference between radii should be more than 15%. Therefore most of the binary alloys, which follow the Hume Rothery rules, cannot be solidified as amorphous structures. These conventionally solidified alloys (in general, which follow the Hume Rothery rules) show the long-range crystal structures. If this crystal structure is broken below the crystallization temperature, the alloys retain their metastable structure. It has been reported that mechanical milling and mechanical alloying can produce such structures [27, 28, 29, 30, 31, 32, 33, 34]. The phase change occurs by inter-diffusion and accumulation of lattice defects such as vacancies. During milling, amorphization can take place if the stored energy in the material exceeds the energy of the amorphous phase [11, 35]. It was also found that mechanical deformation assists inter-diffusion to occur and subsequently to form the homogeneous amorphous alloy [36].

The experimental conditions in mechanical milling are in many ways analogous to the sliding of two surfaces. As discussed in section 5.3.1, during sliding many complex processes occur. Sliding of two materials provides all the necessary experimental parameters and driving forces for amorphization to occur, such as plastic deformation, temperature rise, and the accumulation of the lattice defects. During sliding, the driving force for the diffusion to occur is the temperature rise due to sliding. This temperature increase speeds up the solid reaction and phase changes by inter-diffusion between two

sliding materials. A similar mechanism was explained by Schwarz for the formation of an amorphous alloy from pure crystalline metals [37, 38].

Both Cr and Fe crystals have body center cubic (BCC) structures. The bond length of Cr and Fe are 0.24980 nm and 0.24823 nm, respectively [39]. FeCr is a typical binary alloy which, according to Hume Rothery rules, forms a substitutional solid solution [1]. Although this alloy system is not readily glass forming (RGF), Xia and Saitovitch found that the middle composition range can form an amorphous state by thermal evaporation at room temperature using very low deposition rates [40]. They have calculated Gibbs free energy for the amorphous and crystalline states, shown in Figure 5.14.

In the present investigation, temperature increase during sliding is possible, and this rise in temperature might be the driving force for the inter-diffusion of the Fe and Cr. This diffusion can occur on one of the mating surfaces, on both surfaces, or on the debris after they detach from their parent surfaces. Plastic deformation, which occurred due to the continuously-applied load during the tests, might be the other factor causing amorphization to occur.

The existing amorphous debris can act as a third body for further deformation if debris comes in contact with mating surfaces. Due to the debris' high strength and wear resistance, further deterioration of the mating surface occurs. When wear occurs, along with debris formation, the surfaces undergo various changes. The sub-surface also changes due to existing continuous load conditions and heat generation. The present

study was focused only on debris analysis in order to establish a foundation for future investigation.

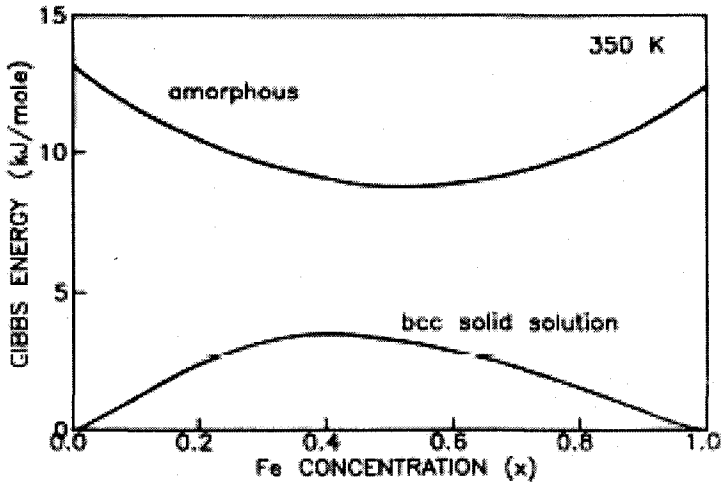

Figure 5.14: Gibbs free energy for amorphous Cr-Fe [14]

5.3.3 Surface Friction Change in Boronized Tantalum

Figure 5.3a shows borides forming on the tantalum surface. In the FFM image in 5.3b, it is found that there is no significant difference in friction. This means that there is no difference in mechanical properties. The visible change in friction is due to the surface roughness. Thus it is concluded that the borides formed on the surface are of the same mechanical properties.

The AFM topological (Figure 5.4a) and FFM image (Figure 5.4b) analysis showed that the surface is different in friction. The friction change on the surface can be assessed by surface response and the roughness. To study the friction change due to surface response, it is necessary to filter out the roughness effect on friction. A similar

line analysis can accomplish this objective. Figure 5.15 is a line profile of the surface. The surface response and roughness effect on friction are discussed here. In Figure 5.15, the blue line is the surface roughness or profile, and others are surface force parameters. It is clearly seen that across most of the distance scanned, the friction does not correlate with the surface roughness. This means that the variation in friction is due to materials properties, rather than surface roughness. In one part of the scan, however, there is some correlation between the surface roughness and the friction. On this line scan there was a sudden height change from scan length 29.961 μm to 30.548 μm, as shown in Figure 5.16. The corresponding friction was also changed due to this height change (Figure 5.16). The friction, appearing from scan length 31.136 μm to 34.926 μm, was not affected by the change in height even though the surface height is constantly decreasing. The overall topology image used for this analysis is shown in Figure 5.17. In this figure, the red line is the profile discussed in Figures 5.4 and 5.17. As noted, Figures 5.4, and 5.15 to 5.17 are correlated with each other.

As discussed, the surface roughness change induces the change in friction on the worn surface, and the materials property (surface) modifications also affect friction. The change in friction due to the surface response might be due to surface property change during sliding. Due to continuous load and frictional forces on the surface, these materials deform plastically. Subsurface deformation is also possible. As discussed in Section 5.3.1, the subsurface deformation, the crack nucleation and growth, and the dislocation movements under the surface are possible [23, 24]. In this research, it was found that the subsurface events are somehow associated with the change in surface

properties. Evidence was found in the frictional force microscope image. It is also possible that the asperities on the surface melt during sliding [21, 22, 23]. Due to rapid cooling, the molten parts solidified into new phases that can be seen in the friction image. Furthermore, work hardening can be induced through continuous sliding. The hardened surface should be differentiated from its original surface in an AFM FFM image.

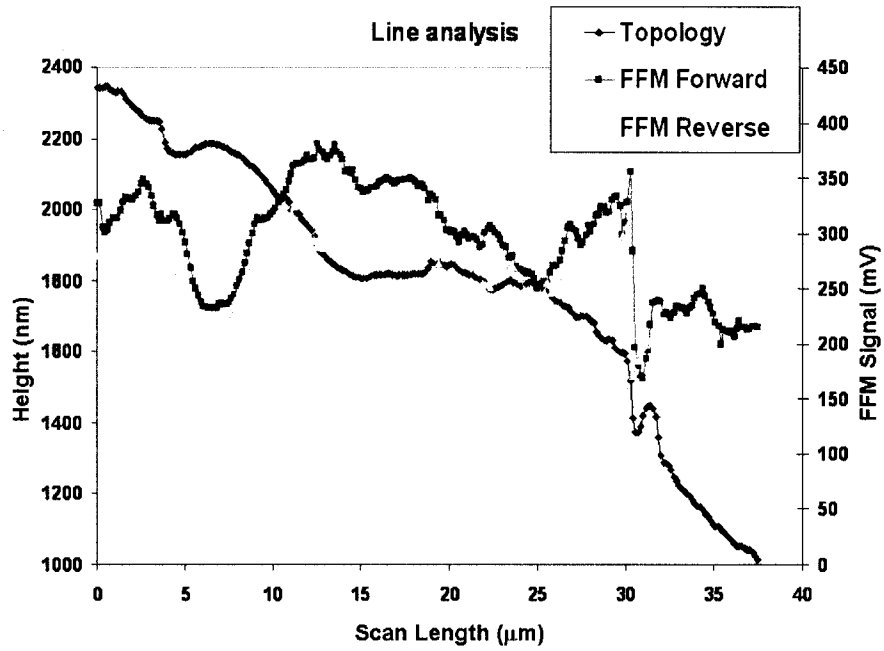

Figure 5.15: The line analysis of topology and FFM scan (line 189).

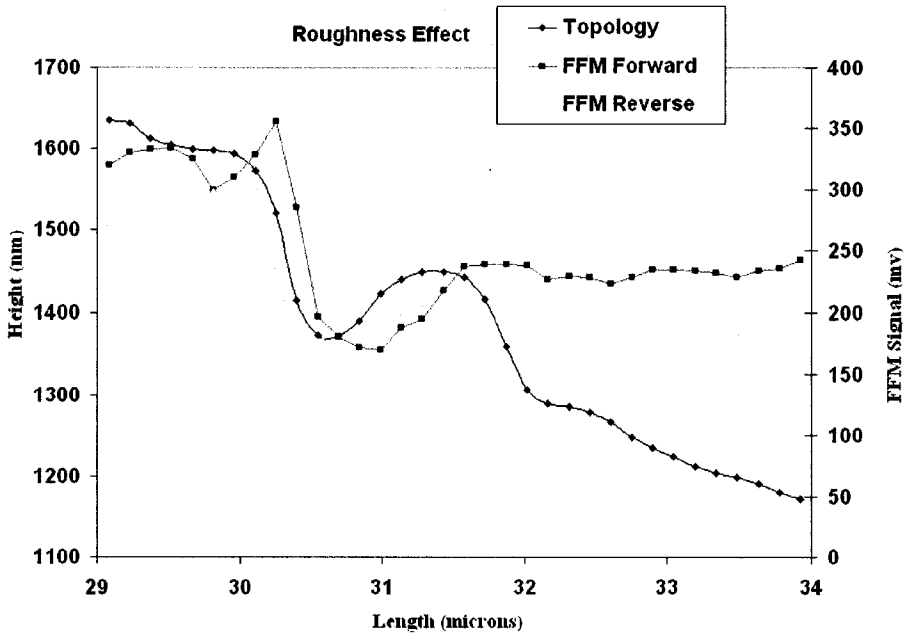

Figure 5.16: Effect of roughness on friction (line 189).

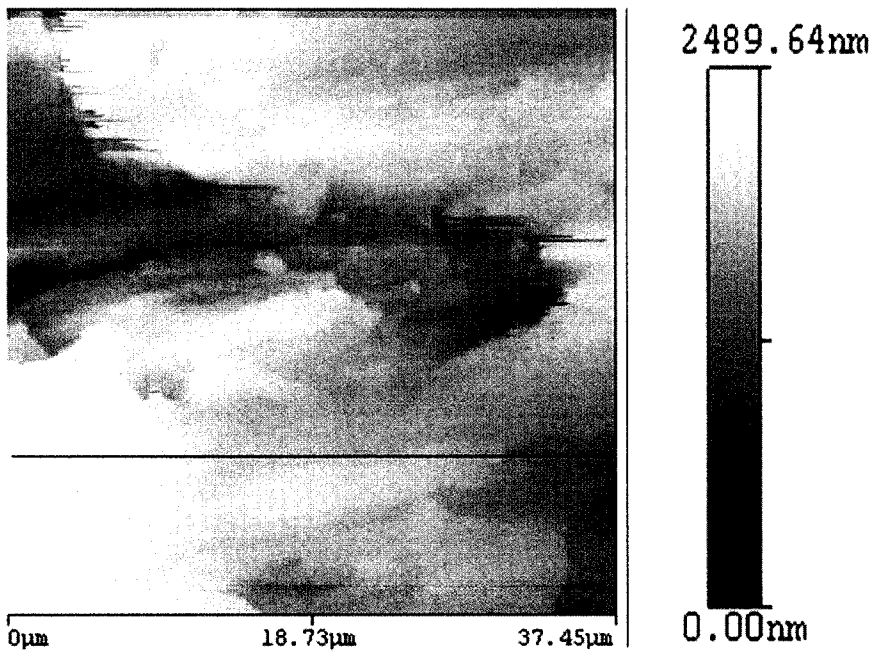

Figure 5.17: Topology image showing line 189.

5.3.4 Aluminum-Copper Sliding

In metals such as Cu, Ni, Fe, Co, W, Mo, and Zn, surface oxide films form and grow as crystalline layers. However, in the case of Al, Si, Cr, Ge, Nb, and Ta, oxidation initially takes place, forming amorphous films, and then these films become crystalline depending upon temperature and time [41, 42, 43, 44, 45]. An amorphous alumina oxide film can be thermodynamically more stable than the corresponding crystalline γ-Al_2O_3 film up to a certain critical oxide-film thickness. This amorphous film can be more stable even for higher oxidation temperatures [3].

In the present work, flat Cu was slid against the Al disc. At the beginning of the experiment the surfaces of both sliding metals were covered with their respective oxides. In the open atmosphere, copper oxidizes to form a copper oxide layer, whereas aluminum forms aluminum oxide. When sliding started, first, the oxide layers were worn. As wear continued, pure metals underneath those oxide layers were exposed to the atmosphere. As soon as the pure metals were exposed to the atmosphere, further oxidation commenced. The oxidation potential of Cu is 0.52 E^oV, and that of Al is 1.66 E^oV. Copper oxidizes at a lower rate than aluminum; aluminum oxidizes almost instantaneously. The initial oxide layer formed on the surface is amorphous alumina. Without sufficient time to crystallize, the amorphous alumina was removed during sliding as amorphous debris. This is proven by the TEM analysis result shown in Figure 5.8.

In the present test, the sliding speed was 0.235 m/sec, and the rotating configuration was used. Thus, each point under the sliding contact takes 0.4 seconds to

come in contact again while the disc is rotating. Assuming that pure Al is exposed to the atmosphere due to wear, the surface of pure Al will have 0.4 sec to oxidize. For Al, this time is sufficient to form amorphous oxide, but not sufficient to transform the amorphous oxide into crystalline alumina. Therefore, it is believed that the oxide layer which is removed is predominantly amorphous alumina. This is a tribo-oxidation process.

At the same time during sliding, there is an increase of temperature. The raised temperature would potentially trigger the nucleation and crystallization. Assuming most of the amount is consumed through conduction, the temperature increase can heat up the debris. Indeed, this was proven to be the case as evidenced by the TEM analysis, as shown in Figure 5.8. This figure shows the bright field image of such debris in TEM. The selective area diffraction pattern from the same debris in Figure 5.9 shows that the nano nucleates formed on the debris.

According to above discussions and further evidence from TEM results, a removal model is generated; the schematic of the tribo-oxidation wear process is illustrated in Figure 5.18. There are three steps in this process: pre-oxidation, removal of the initial oxide layer, and removal of the newly formed oxide layer. Pre-oxidation is the natural oxidation of the surface of mating metals. When a pure metal is exposed to oxygen, it oxidizes and forms oxide layer on the surface.

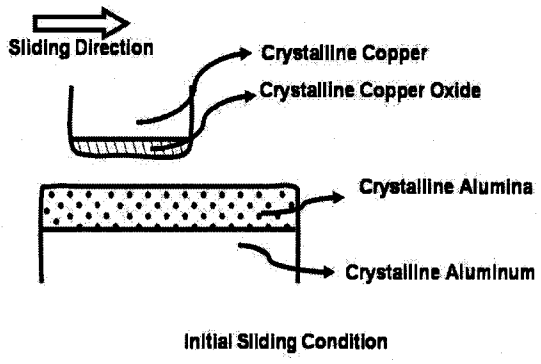

a: Pre-oxidation

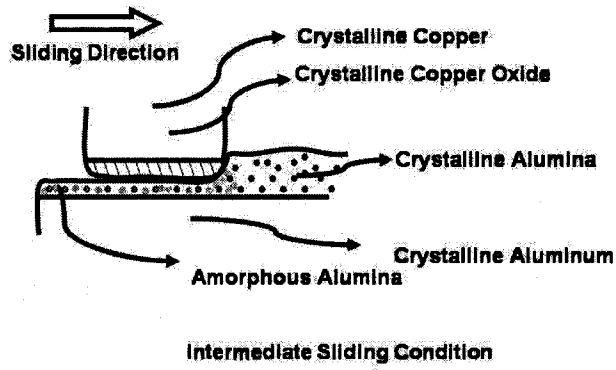

b: Removal of initial oxide layer

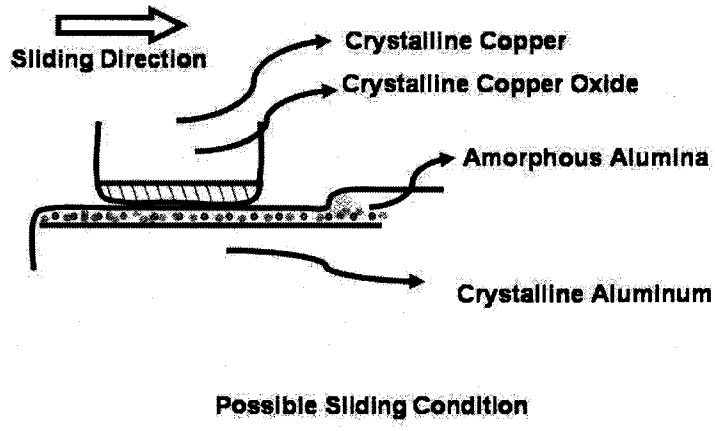

c: Removal of newly formed oxide layer

Figure 5.18: Schematic of the tribo-oxidation wear process in Al-Cu sliding.

5.4 References

1 G. Beilby, "Aggregating and Flow of Solids" Macmillan and Co., Ltd., London 1921.

2 F. P. Bowden, T.P. Hughes, "Physical properties of the surfaces IV – Polishing surface flow and the formation of the Beilby Layer" Proceedings of the Royal Society, 160A 1937 p575-587.

3 F. P. Bowden, D. Tabor, "The Friction and Wear of Solids, Part II" Clarendon Press, Oxford 1964.

4 D.A. Rigney, J. E. Hammerberg, "Mechanical mixing and development of nanocrystalline material during the sliding of metals: Advanced Materials for 21st Century, The 1999 Julia R. Weertman Symposium", TMS (The Minerals, Metals & Materials Society) 1999.

5 S. K. Ganpathi, D.A. Rigney, "An HRTEM Study of the nanocrystalline material produced by sliding wear processes" Scripta Metallurgica et Materialia 24 1990 p1675-1678.

6 D. A. Rigney, X. Y. Fu, J. E. Hammerberg, B. L. Holian, M. L. Falk, "Examples of structural evolution during sliding and shear of ductile materials" Scripta Materialia 49 (10) 2003 p977-983.

7 X. Y. Fu, M. L. Falk, D. A. Rigney, "Sliding and deformation of metallic glass: experiments and MD simulations" Journal of Non-Crystalline Solids 317 2003 p206.

8 P. Heilmann, J. Don, T. C. Sun, D. A. Rigney, W. A. Glaeser, "Sliding wear and transfer" Wear 91 (2) 1983 p171-190.

9 L. H. Chen, D. A. Rigney, "Transfer during unlubricated sliding wear of selected metal systems" Wear 105 (1) 1985 p47-61.

10 A. Erdemir, C. Bindal, J. Pagan, P. Wilbur, "Characterization of transfer layers on steel surfaces sliding against diamond-like hydrocarbon films in dry nitrogen" Surface & Coatings Technology 76–77 1995 p559.

11 A. Erdemir, C. Bindal, G. R. Fenske, C. Zuiker, P. Wilbur, "Characterization of transfer layers forming on surfaces sliding against diamond-like carbon" Surface & Coatings Technology 86–87 1996 p692.

12 N. S. Park, M. W. Kim, S. C. Langford, J. T. Dickinson, "Atomic layer wear of single-crystal calcite in aqueous solution using scanning force microscopy" Journal of Applied Physics 80 1996 p2680-2686.

13 L. Scudiero, S. C. Langford, J. T. Dickinson, "Scanning force microscope observations of corrosive wear on single-crystal brushite ($CaHPO_4 \cdot 2H2O$) in aqueous solution" Tribology Letters 6 1999 p41-55.

14 R. Hariadi, S. C. Langford, J. T. Dickinson, "Controlling nanometer-scale crystal growth on a model biomaterial with a scanning force microscope" Langmuir 18 (21) 2002 p7773 –7776.

15 S. Gururzu, M. Kulkarni, S. Ingole, H. Liang, "Friction induced crystalline phases on Si" Gordon Research Conference 2004–Tribology at Roger Williams University, Bristol, RI, 26 June-2 July 2004.

16 S. Gururzu, M. Kulkarni, S. Ingole, H. Liang, "Friction induced crystalline phases on Si" 15th International Conference on Wear of Materials (WOM 2005) to be held in San Diego, USA April 24-28, 2005. (Article in press).

17 S. Gururzu, M. Kulkarni, S. Ingole, H. Liang, "Friction induced crystalline phases on Si" 15th World Tribology Congress III, to be held in Washington D.C. on Sept. 12-16. 2005 (Accepted).

18 S. Gururzu, M. Kulkarni, S. Ingole, H. Liang, "Friction induced crystalline phases on Si" STLE 2005 to be held in Las Vegas, May 15-19 2005 (Accepted).

19 F. P. Bowden, D. Tabor, "The Friction and Lubrication of Solids, Parts I and II" Clarendon Press, Oxford 1964.

20 J. C. Jaeger, "Moving sources of heat and the temperature at sliding contacts" Proceedings of the Royal Society, N.S.W., 56 1942 p203-224.

21 N. H. Cook, B. Bhushan, "Sliding surface interface temperature" Journal of Lubrication Technology, 95 1 1973 p59-64.

22 N. P. Suh, "Tribophysics" Prentic-Hall, Inc., Englewood Cliffs, New Jersey 1986.

23 N. P. Suh, "The delamination theory of wear" Wear 25 1973 p111-124.

24 W. Hume-Rothery, "The Metallic State" Oxford University Press, Oxford 1931 p328-36.

25 H. A. Davies, In "Amorphous Metallic Alloys" F. E Luborsky [Ed.], 1983 Butterworth, London p8.

26 B. C. Giessen, Proc. 4th Int. Conf. on Rapidly Quenched Metals, Sendai. 1981 Vol 1 Japan Institute of Metals, Sendai 1982 p213.

27 S. K. Xia, E. B. Saitovitch, V. A. P Rodriguez, F. C. Rizzo, "Formation of disordered structures in Cr-Fe alloy by mechanical milling" Journal of Physics Condensed Matter 5 1993 p2729-2738.

28 E. Gaffet, N. Merk, G. Martin, J. Bigot, "Ball milling amorphization mechanism of Ni-Zr alloys" Journal of the Less Common Metals 145 1988 p251-260.

29 E. Hellstern, L. Schultz, "Formation and properties of mechanically alloyed amorphous Fe-Zr" Material Science and Engineering 97 1988 p39-42.

30 C. C. Koch, O. B. Cavin, C. G. McKamey, J. O. Scarbrough, "Preparation of "amorphous" Ni[sub 60] Nb[sub 40] by mechanical alloying" Applied Physics Letters 43 1983 p1017.

31 J. R. Thompson, C. Politis, "Formation of amorphous Ti-Pd alloys by mechanical alloying methods" Europhysics Letters 3 (2) 1987 p199-205.

32 B. P. Dolgin, M. A. Vanek. T. McGory, D. J. Ham, "Mechanical alloying of Ni, Co, and Fe with Ti: Formation of an amorphous phase" Journal of Non-Crystalline Solids 87 (3) 1986 p281-289.

33 C. Politis, W. L. Johnson, "Preparation of amorphous $Ti_{1-x}Cu_x$ ($0.10 < x <= 0.87$) by mechanical alloying" Journal of Applied Physics 60 1986 p1147.

34 L. Schultz, "Glass formation by mechanical alloying" Journal of the Less Common Metals 145 1988 p233.

35 R. B. Schwarz, C. C. Koch, "Formation of amorphous alloys by the mechanical alloying of crystalline powders of pure metals and powders of intermetallics" Applied Physics Letters 49 146 1986.

36 Michael Atzmon, John D. Verhoeven, Edwin D. Gibson, W. L. Johnson, "Formation and growth of amorphous phases by solid-state reaction in elemental composites prepared by cold working" Applied Physics Letters 45 1984 p1052.

37 R. B. Schwarz, W. L. Johnson, "Formation of an amorphous alloy by solid-state reaction of the pure polycrystalline metals" Physical Review Letters 51 (5) 1983 p415–418.

38 W. L. Johnson, "Thermodynamic and kinetic aspects of the crystal to glass transformation in metallic materials" Progress in Materials Science 30 (2) 1986 p81-134.

39 R. C. Weast, Handbook of Chemistry and Physics 46th Edn 1965 Chemical Rubber Company, Boca Raton, FL p119.

40 S. K. Xia, E. B. Saitovitch, "Formation of an amorphous phase in $Cr_{(1-x)}Fe_X$ films obtained by thermal evaporation, Physical Review B 49 5 1994 p.927.

41 F. P. Fehlner, "Low-temperature Oxidation: The Role of Vitreous Oxides" Wiley-Interscience, New York 1981.

42 L. P. H. Jeurgens, W. G. Sloof, F. D. Tichelaar, E. J. Mittemeijer, "Thermodynamic stability of amorphous oxide films on metals: Application to aluminum oxide films on aluminum substrates" Physical Review B 62 2000 p4707.

43 P. E. Doherty, R. S. Davis, "Direct observation of the oxidation of aluminum single-crystal surfaces" Journal of Applied Physics 34 1963 p619.

44 J. I. Eldridge, R. J. Hussey, D. F. Mitchell, M. J. Graham, "Thermal oxidation of single-crystal aluminum at 550°C" Oxidation of Metals (Historical Archive) 30 (5 – 6) 1988 p301 – 328.

45 P. C. Snijders, L. P. H. Jeurgens, W. G. Sloof, "Structure of thin aluminium-oxide films determined from valence band spectra measured using XPS" Surface Science 496 (1-2) 2002 p97-109.

Chapter 6

Indentation-Modified Surface

6.1 Literature Review

Over the years, the Vickers indentation method has been used to study the mechanical properties of materials. This technique has also been used to study the surface and subsurface crack propagation and to measure the fracture toughness for brittle solids [1]. Indentation with a sharp indenter produces high shear and hydrostatic stresses beneath the indenter's tip. Surface atoms move under the indenter as well. Under indentation, applied energy is sufficient to change the mechanical properties of the materials. K. Kese [2] studied the influence of residual stresses on elastic modulus and hardness, using nanoindentation with a Vickers indenter. He found that tensile stresses cause the elastic modulus to decrease, while compressive stresses cause it to increase.

In many metalworking processes, friction is one of the predominating parameters that determine the shape of the finished product. G. Dieter [3] used the theoretical approaches to study friction at the interface in a compression test of a disc.

The importance of understanding friction is obvious. With the advancement of nanoscale surface characterization techniques, the AFM has become increasingly important in studying surface properties. To date, it has not been widely reported how an AFM can be used for studying nanomechanical properties of deformed materials. The aim of the present investigation is to understand the frictional behavior of deformed surfaces. Specifically, this research focuses on Vickers indentation. The experimental details were explained in Chapter 4.

6.2 Experimental Results

Figures 6.1a and 6.1b are topological and FFM images of a Vickers indent made at a 25 g load. These figures were generated in a contact-mode configuration of an AFM. The topography shown in Figure 6.1a depicts a large indent at the center of the figure, with debris found around the indent. In the FFM image, Figure 6.1b, there are some clearly evident, almost-symmetric fringes inside the indent. Outside of it, however, there are no regular fringes.

Figure 6.2a is the image of the topology of the Vickers indent with line analysis. This figure shows the indentation slope of the indent's side wall and its depth. Figure 6.2b is a phase image using a non-contact mode of AFM. From the line scan, it is seen that the line is near-smooth. These results show that the surface of an indent is microscopically smooth but nanoscopically rough. More details will be discussed later. In Figure 6.2b, there are basically two different phases found. The brighter area represents a harder phase than the darker one. In the area around the lower left corner, "hard" phases

are parallel to each other. It is important to notice that these fringes are those observed in Figure 6.1b.

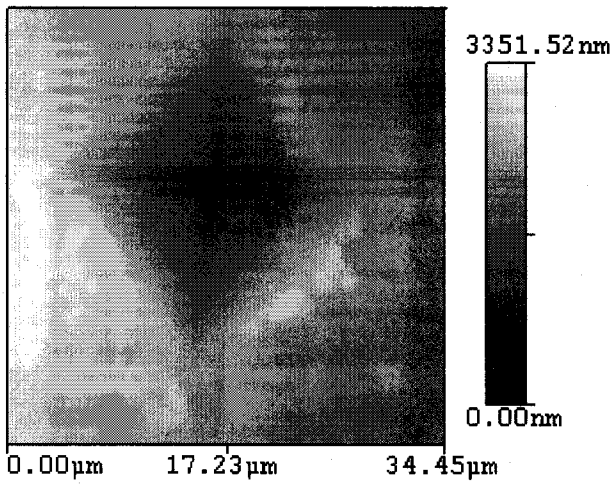

a) Topological image

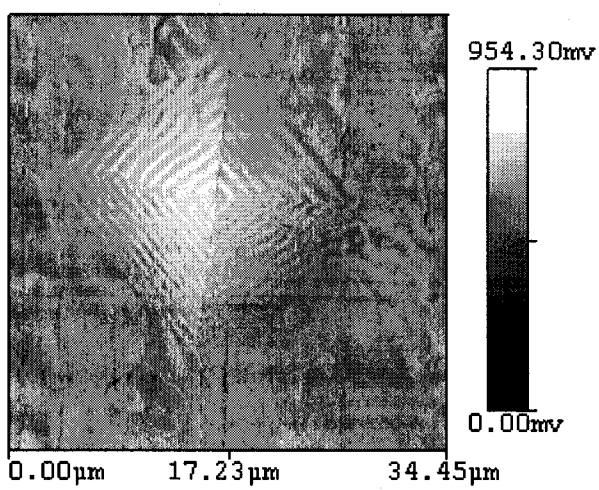

b FFM image

Figure 6.1: Vickers indent on copper surface.

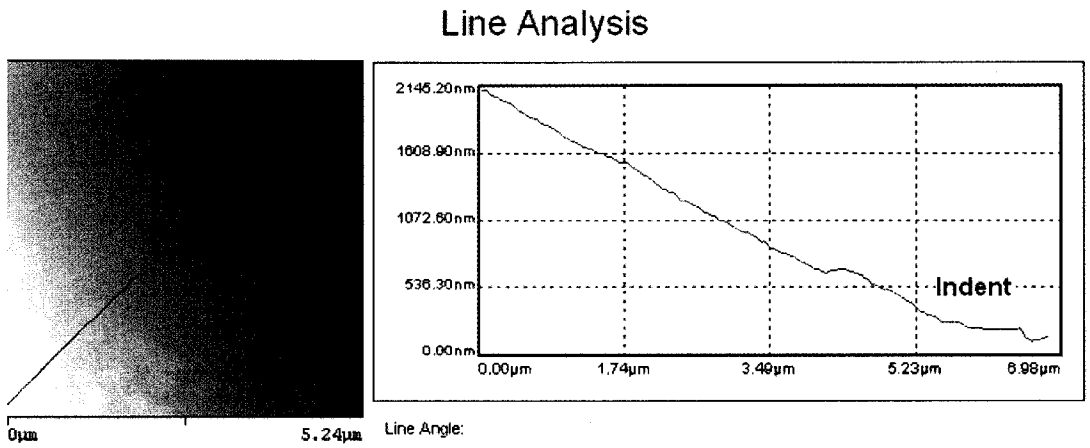

a Topology with line scan

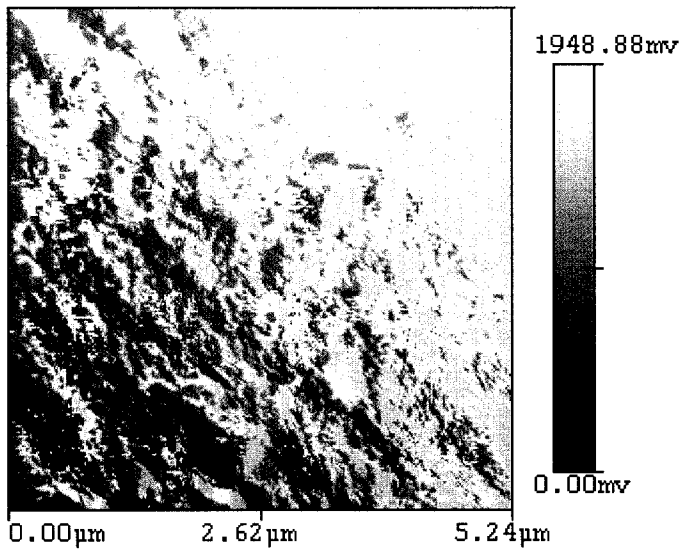

b Phase image

Figure 6.2: Vickers indent on copper surface.

6.3 Discussion

As mentioned earlier, the FFM image taken on the Vickers indent showed clear, almost symmetric fringes inside the indent. This image is by nature the frictional response of the surface to the AFM probe. Interestingly, these fringes are regular inside the indent where the material is deformed, while in areas outside the indent, the fringes are wider and less regular in space. Based on the design of the AFM, the brighter area should be the area associated with high friction. It is known that the surface roughness affects friction [4]. Therefore, it is believed that the brighter area is related to a region of high friction. This is further supported by the following.

In order to see the effects of roughness, a surface line scan was made and is shown in Figure 6.3. This line scan was made on one of the side walls of the indent. It is seen that peaks and valleys are nanometer-length scale. At the top of the indent; i.e., on the surface, there is a pile-up of materials at the edge of the indent. Farther away from it, the surface is flattened. It has been accepted that within the Hertzian stress distribution, the point of maximum shear stress occurs beneath the surface on the axis of the applied load [5]. When the shear stress exceeds the shear strength of a material, deformation, which is always the case in Vickers indentation, commences. The dislocation movement is one of the mechanisms that deform the elastic-plastic material. Theoretically, there are two explanations regarding the response of the materials beneath Vickers indent: an expanding cavity model [6, 7] and a slip line field theory [8]. In the expanding cavity model, the hardness response in Vickers indentation is modeled as an elastic zone that

expands rapidly beneath the indenter against the constraint provided by the surrounding elastic materials [5, 6]. In this model, the pile-up of material around the indentation is attributed to the relaxation, which occurs on unloading of the indenter. Here, due to shear stresses, copper deformed plastically and hardened. The principal stresses in this region will be purely compressive. K. Kese [2] has shown that the compressive stress increases the elastic modulus and hence the friction.

Further investigation on friction properties was conducted. The FFM signal versus location of the indent is shown in Figure 6.4. The FFM signal on different faces was analyzed. Here the four lines - blue, pink, red, and green - are FFM signals from four different inclined faces of the indent. Results show that friction is higher toward the center of the indent than that at the top of the indent. There are two possible explanations for this. One is a larger surface roughness, and the other is the higher elastic modulus. As shown in Figure 6.3, however, toward the center, i.e., close to the 0 μm area, the surface profile (roughness) is the same as that shown in the area toward the surface. Therefore, the change of friction should not be due to the surface roughness change. The next possibility is the elastic modulus. Indeed, there is a great potential for hardening inside the indent. In the previous paragraph, it was discussed that the stress concentration is the highest toward the center of the indent. Also shown in Figure 6.3 is that the pile-up can be only seen at the outside edge of the indent, where there is no constraint from the material, while at the bottom, there is no space for materials to pile up, so material is pushed and becomes densified, therefore, hardened. Moreover, a similar trend was found

in the phase image of the indent. The harder phase was observed towards the center of the indent (Figure 6.2b).

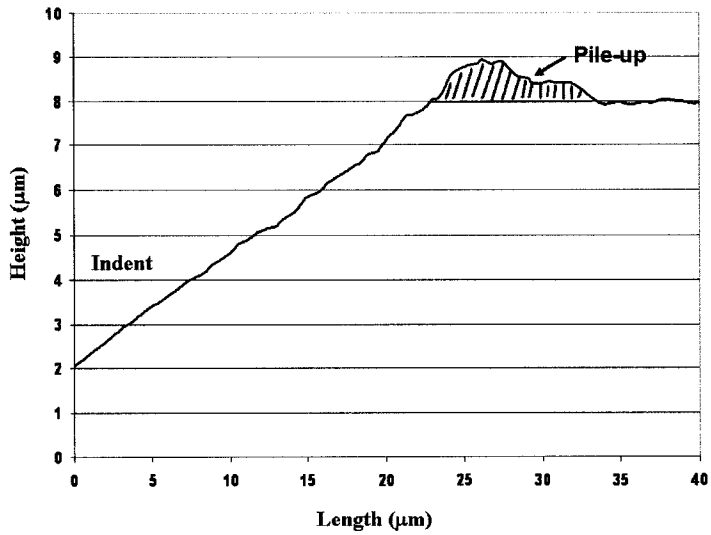

Figure 6.3: The pile-up region formed on the edges of the indent (load 300g).

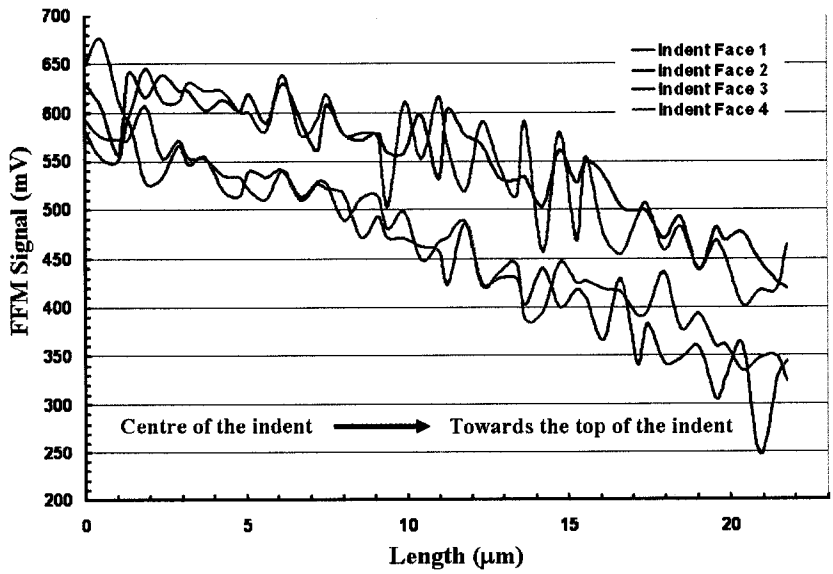

Figure 6.4: The friction change towards the center of the indent.

Further investigation was conducted on an indent made under a 25g load. Figure 6.5 shows the analysis. Here the blue line is the profile of the indent. The red and green lines are FFM scans from forward and the backward directions, respectively. The reason for using a two-direction scan was to fill out the effect of slopes. If both scans show exactly the same pattern at a particular location, this reflects the surface property of that location. In Figure 6.5, both FFM scans are high in number at the center of indents. As discussed, the surface roughness of this indent has less of an effect on the FFM value. The elastic modulus is more dominant. As such, we conclude that the indent is hardened more at the center of the indent and less at the edge. This was the first time such hardening under an indent using an AFM has been reported.

Finally, the analysis of those fringes was conducted. The average width of fringes (Figure 6.1b) was measured. Within a certain limit, the fringes were wider at the center of the indent than at the edge. The limit is shown as error bars in Figure 6.6. More importantly, the width of these fringes is more dependent on the load in the same figure. Here, a load dependent phenomenon is not surprising, since the ductile material has significant plastic flow and therefore more inherent hardening. Since the plastic flow and hardening mechanisms were not the focus of this study, future investigation will be proposed at the end of this dissertation.

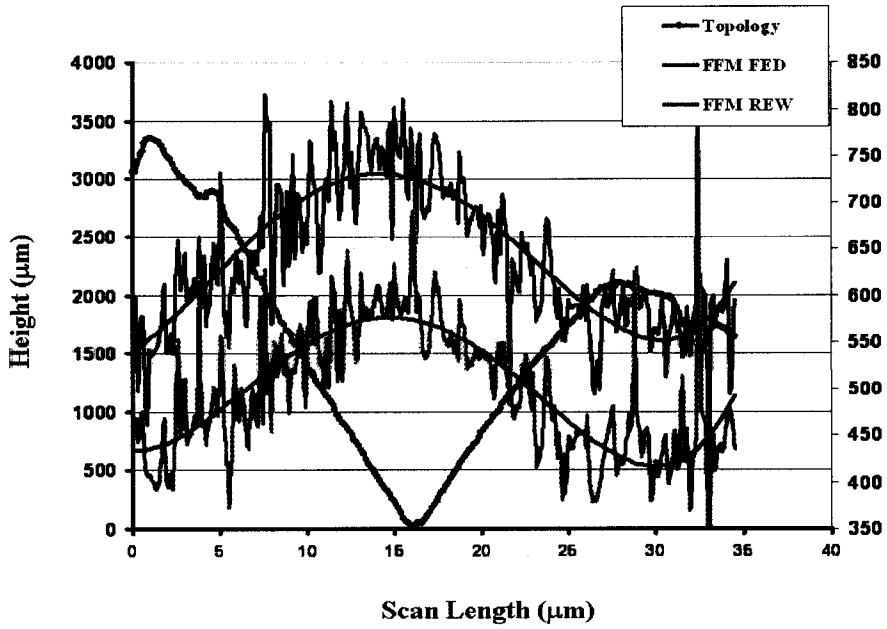

Figure 6.5: Friction change on a Vickers indent (load 25 g).

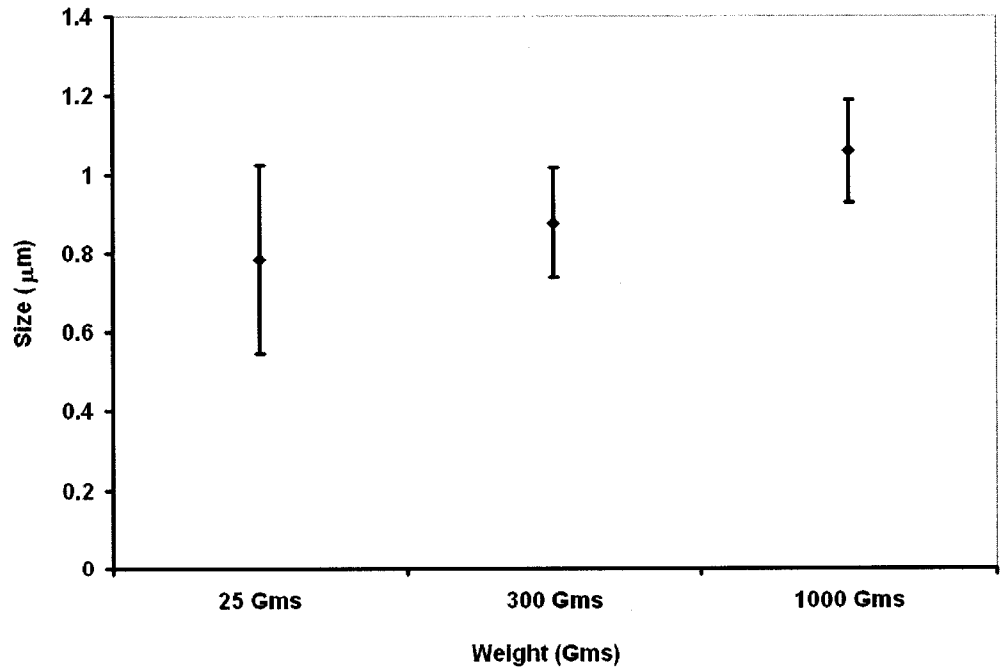

Figure 6.6: Fringe width variation with load.

6.4 References

1 B. R. Lawn, "Fracture of Brittle Solids" 2nd edition: Cambridge University Press, Cambridge, U.K. 1993.

2 K. Kese., "Relaxation and nanomechanical studies of the Vickers residual stress field in glass" Doctoral Thesis, Royal Institute of Technology, Stockholm, Sweden, 2004.

3 G. Dieter, "Mechanical Metallurgy" McGraw-Hill Book Co., UK, 1988

4 R. Overney, E. Mayer, "Tribological investigations using friction force microscopy" MRS Bulletin May 1993 p26-34.

5 K. L. Johnson, "Contact Mechanics" Cambridge University Press, Reprint edition, August 28, 1987.

6 D. M. Marsh, "Plastic flow in glass" Proceedings of the Royal Society of London, Series A 279 1378 1964 p420.

7 K. L. Johnson, Journal of the Mechanics and Physics of Solids 18 115 1970.

8 R. Hill, E. H. Lee, S. J. Tupper, "The theory of wedge indentation of ductile materials" Proceedings of the Royal Society of London, Series A 188 1013 1947 p273.

Chapter 7

Friction and Wear Study of Potential Biomaterials

7.1 Introduction

Human beings are said to have 173 bearings; all obeying the laws of tribology [1]. In recent years, instances of failures of the joints in the human body have increased. There are many reasons for this, including age, disease, and accidents. Artificial materials have been used over many years to functionalize the body parts. The materials are said to be biocompatible, which means there should be no adverse effect on the human body tissues due to prolonged contact with these foreign materials, since it is the natural tendency of human body tissues to reject foreign materials. There are different types of biocompatible materials. For example, inert materials do not react with the body tissues. Other biomaterials integrate with the tissues during their growth.

7.2 Boride Coatings in Tribology

Boride coatings have been applied to metal surfaces in order to improve their corrosion resistance, electrochemical properties, and tribological performance; and to prolong service life [2]. Efforts have been made to study the material properties of boronized steels [3, 4, 5, 6, 7]. Anthymidis et al. did a comparative study of boride coatings on a steel substrate obtained by the pack-cementation method and by fluidized bed technology [3]. Pack cementation is an *in situ* self-generated chemical vapor deposition (CVD) coating technology. In the fluidized bed method, the part to be coated is preheated in an oven and dipped into the fluidized bed of the target powder. As they come in contact with the hot parts, powder particles melt and solidify, forming a uniform coating. Coatings were characterized as having good adherence and only one phase, Fe_2B, was formed during the treatments. The pack cementation procedure resulted in coatings with residual stresses and preferred orientation, while the coatings produced by the fluidized bed were characterized as strain-free grains with random distribution [3]. Xu et al. [4] compared superplastic and conventional boronizing. They reported that superplastic boronizing retarded the formation of high boron containing boride phases and reduced the growth texture of the borides. With superplastic boronizing (001) FeB growth texture was eliminated and (001) Fe_2B growth texture was reduced significantly. In the same report, researchers noted that the superplastic boronizing processes suppressed the formation of Si-rich zones which otherwise would have formed between boride grains. The microhardness of the boride layer processed by superplastic boronizing was more uniform than that produced by conventional boronizing.

Palombarini et al. studied the role of oxygen in iron boronizing [5]. Their results indicated that the residual gaseous oxygen in the reactive atmosphere in the boronizing of Armco iron in B_4C-KBF_4-SiC powder mixtures was detrimental. It reacted with boron to form gaseous boron oxides rather than reacting with carbon in B_4C to liberate active boron for the process. The presence of oxygen in powder mixtures containing Fe_2O_3, Fe_3O_4, or SiO_2 also led to a decrease of B_4C reactivity, as shown by a lower production of surface Fe_2B. Surface structure, texture, and growth of boride coatings on Armco iron and Fe-C-1.26% Cr was studied by SEM and x-ray diffraction [6]. Single-phase Fe_2B and 2-phase FeB/Fe_2B layer structures were examined. It was found that there is no simple relation between texture and interphase topology. The columnar topology of Fe_2B on the substrate interface was explained by a tip-enhanced growth mechanism. FeB was a hard phase growing in a hard Fe_2B matrix, whereas Fe_2B grew in the ductile substrate matrix. This resulted in different local stresses and lattice distortions at the interface. Qunli et al. [7] used an Atomic Force Microscope (AFM) to analyze the surface of the Ni-B coatings treated in different processes. It was found that the microhardness was related to the surface topography of coating and the types of borides which emerged in the deposit. The authors observed nanometer size protrusions of 20-40 nm in height. Boronizing is a thermo-chemical diffusion surface treatment in which boron atoms diffuse into the surface of the work piece to form hard borides with the base materials [8].

Mechanisms of wear in boronized steels have been reported. In previous studies, formation and self-lubricating mechanisms of thin boron oxide and boric acid films on surfaces of boronized steel have been reported. The ultra-low friction behavior of

boronized steel surfaces was due to layer-lattice structures of these films [9 ,10 , 11, 12, 13]. Martini et al. [14] studied the sliding and abrasive wear of boronized coating on steel. They found that there was a difference in the values of surface height in different regions of the coatings. The difference was due to various crystallographic orders of iron borides. The wear resistance was initially poor when there was a thin, friable layer constituting disordered crystals. The wear resistance increased to a maximum value in regions with ordered Fe_2B crystals.

Due to their high wear resistance and corrosion resistance, boronized refractory metals have a potential application as implant material. The motivation of present research is to understand the most fundamental tribological issues of boronized refractory metals. The tribological experiments were carried out to study the fundamental mechanisms of wear. The study was conducted under two different conditions: dry conditions at ambient temperature, and using simulated bio fluid (SBF) as a lubricant at ambient temperature. Simulated body fluid has a composition similar to body plasma. The effects of SBF on the wear behavior of the sliding surfaces were studied. The chemical composition of SBF is described in the Discussion section of this chapter. Experimental details are given in Chapter 4. The detailed analysis of results is discussed in the following sections.

7.3 Experimental Results

7.3.1 Friction and Wear in Dry Conditions

7.3.1.1 Tungsten and Boronized Tungsten

Figure 7.1 shows the change in the coefficient of friction (between the bearing ball and tungsten substrate) plotted as a function of time. Figure 7.2 shows the change in surface height of the pin (indicating wear) with time for tungsten substrate. Figure 7.3 shows the change in the coefficient of friction with time for boronized tungsten. Figure 7.4 shows the change in surface height with time, which indicates wear of both the pin and the disc materials.

Figures 7.5a and b are the topology and the FFM images of tungsten substrate, respectively. Figures 7.6a and b are the topology and the FFM images of boronized tungsten, respectively. Figure 7.6a shows that a compact and continuous layer of boride formed on the surface of the tungsten.

Figures 7.7a and b show the topology and the FFM images, respectively, of the wear track formed on the tungsten substrate. The arrow indicates the sliding direction. The topology image of tungsten wear debris formed is shown in Figure 7.8a, and the FFM image in Figure 8b.

The topology and the FFM images of boronized tungsten wear tracks are shown in Figures 7.9a and 7.9b, respectively. The arrow indicates the sliding direction. Figures

7.10a and 7.10b show the topology and FFM images, respectively, of debris formed during the wear test.

The EDS spectrum observed in FE-SEM is shown in Figure 7.11. Inset 1 is the wear scar on the steel ball, which was observed using an optical microscope, and Inset 2 is the FE-SEM image showing the debris particles on the wear track. Figure 7.12 shows the element mapping for Fe, C, and W on the wear track.

7.3.1.2 Boronized Niobium

Figures 7.13a and 7.13b are topological and FFM images of the niobium boride layer. Figure 7.14 shows the coefficient of friction plotted against the sliding duration of a steel pin against a niobium boride coating. The change in the surface height of the pin (indicating wear) with time is shown in Figure 7.15. This change of height includes wear of both the disc and the pin.

Figure 7.16 shows the topology of the wear track formed on boronized niobium during sliding with the bearing ball. The arrow indicates the sliding direction.

Figure 7.17 is the image of wear debris. Figures 7.17a and 7.17b are the topology and the FFM images, respectively, of the wear debris.

7.3.1.3 Boronized Tantalum

Figures 7.18a and 7.18b are the topological and the FFM images of the tantalum boride layer.

The friction coefficient vs. time is shown in Figure 7.19. The change in the surface height of the pin (indicating wear) with time is also shown in Figure 7.19. The change of height includes wear of both the steel ball and the disc.

Figure 7.20 shows topology (7.20a) and the FFM image (7.20b) respectively of the wear track formed on the boronized tantalum. The arrow indicates the sliding direction. This image shows the wear track formed on the boronized tantalum.

Figure 7.21 is the image of wear debris where 7.21a shows topology and 7.21b is the FFM image.

7.3.2 Friction and Wear Using SBF as Lubricant

7.3.2.1 Boronized Tungsten

Figure 7.22 shows the coefficient of friction between the steel ball and boronized tungsten plotted against time. The simulated body fluid (SBF) was used as a lubricant. Figure 7.23 shows a topological image of the wear track imaged using the AFM.

7.3.2.2 Boronized Niobium

Figure 7.24 shows the coefficient of friction between the steel ball and boronized niobium plotted against time. The simulated body fluid (SBF) was used as a lubricant. Figure 7.25 shows the worn surface observed after a friction test using the AFM.

7.3.2.3 Boronized Tantalum

Figure 7.26 shows the coefficient of friction between the steel ball and boronized tantalum plotted against time, using simulated body fluid (SBF) as a lubricant. Figure 7.27 shows the topology of the wear track after the friction test, imaged using the AFM.

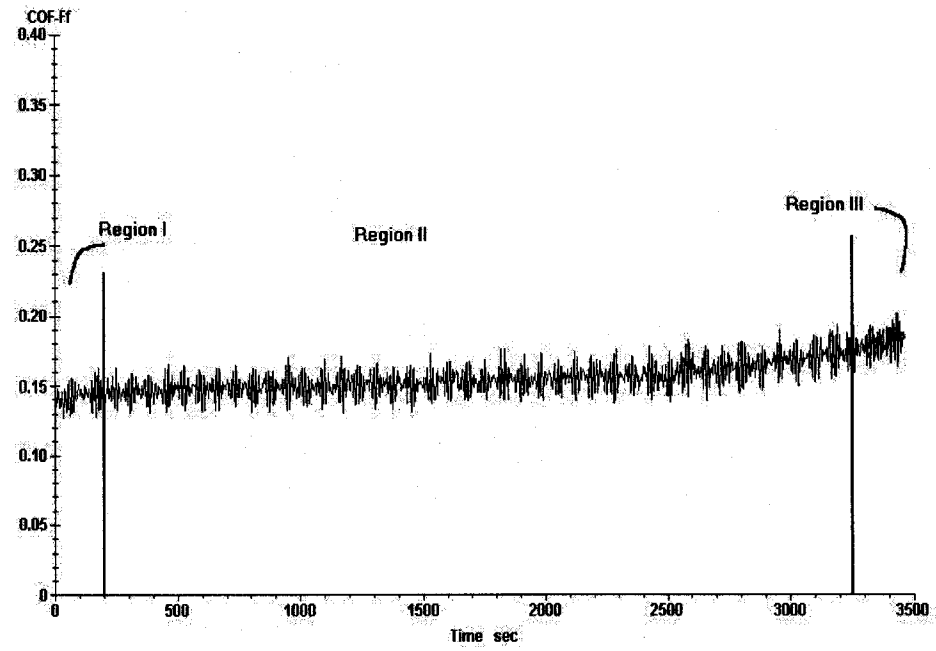

Figure 7.1: Coefficient of friction plotted against time for tungsten substrate.

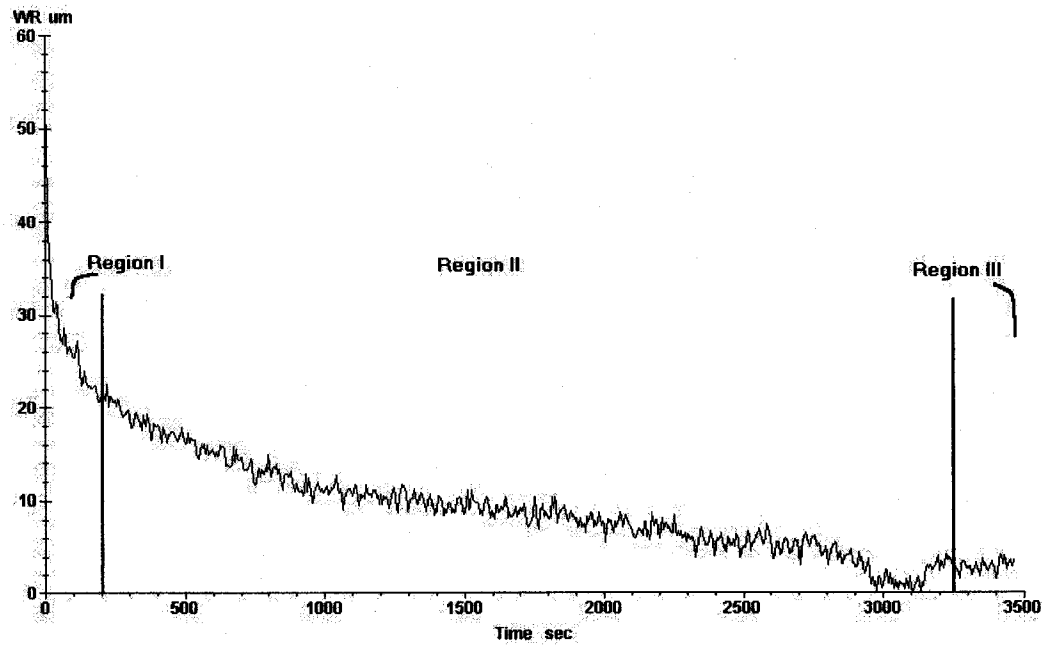

Figure 7.2: Reduction in pin height (linear wear) with time for tungsten substrate.

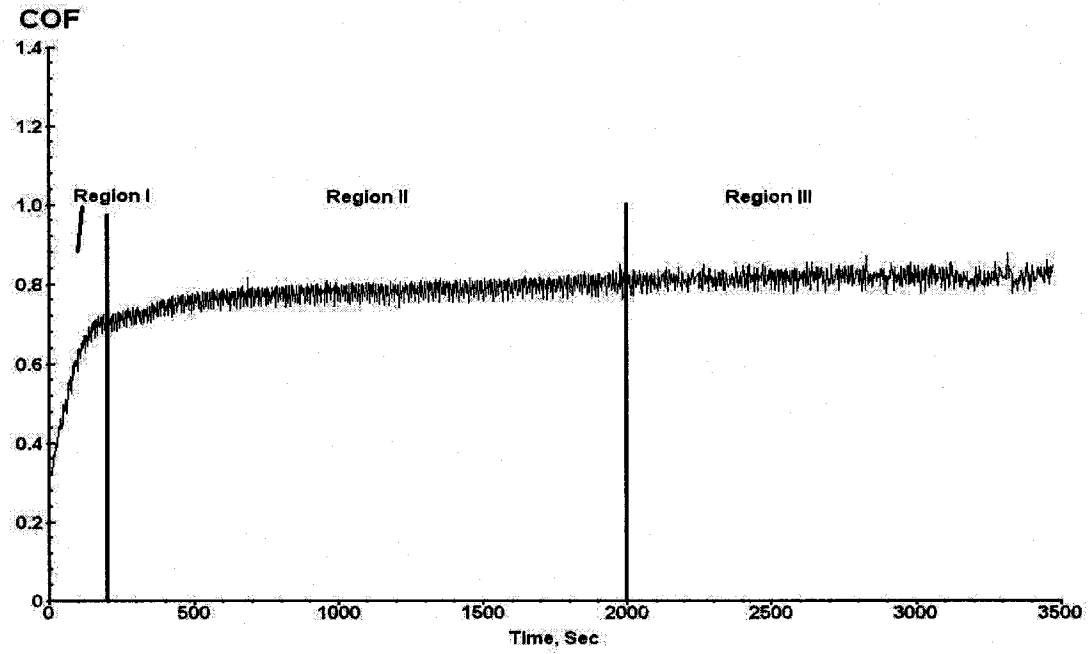

Figure 7.3: Coefficient of friction with time for boronized tungsten.

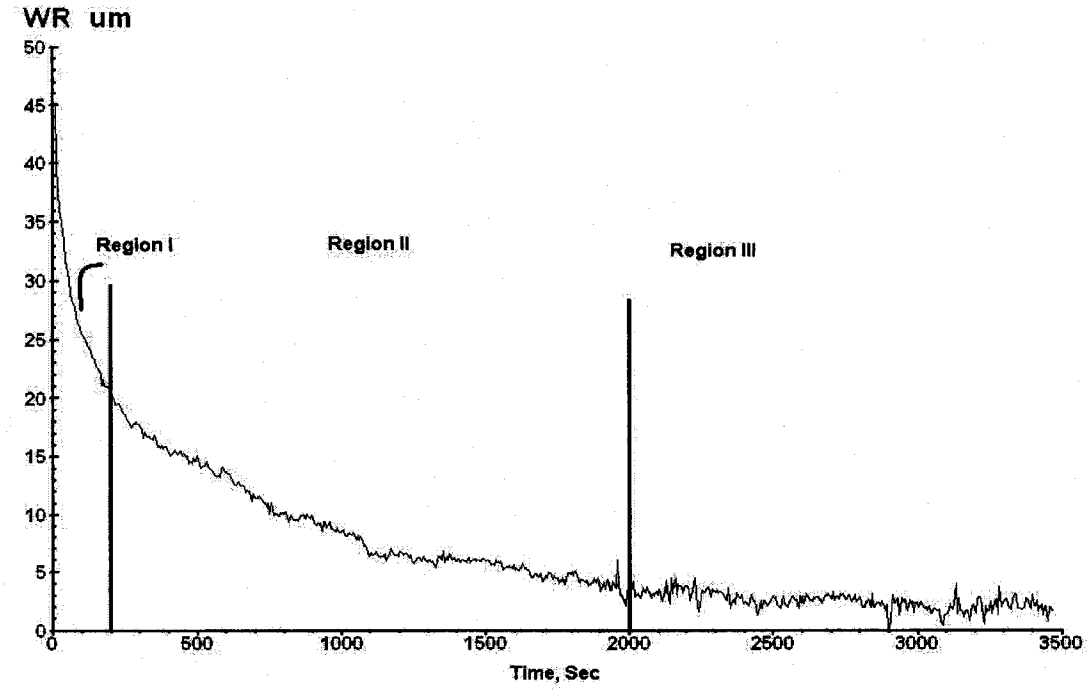

Figure 7.4: Reduction in pin height (linear wear) with time for boronized tungsten.

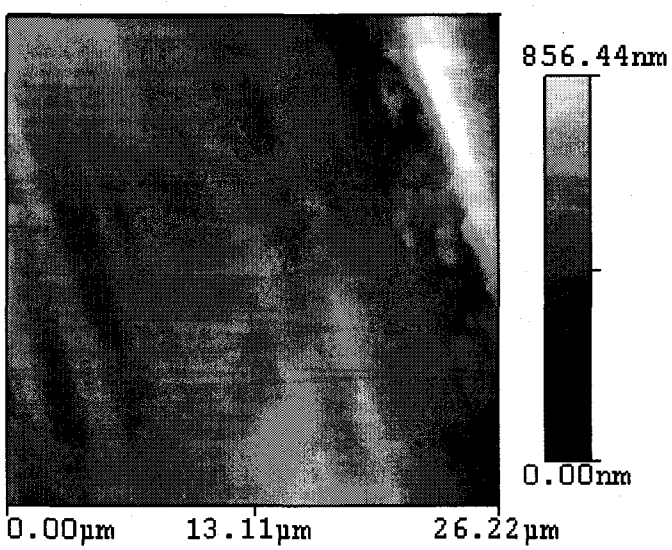

a) Topology image

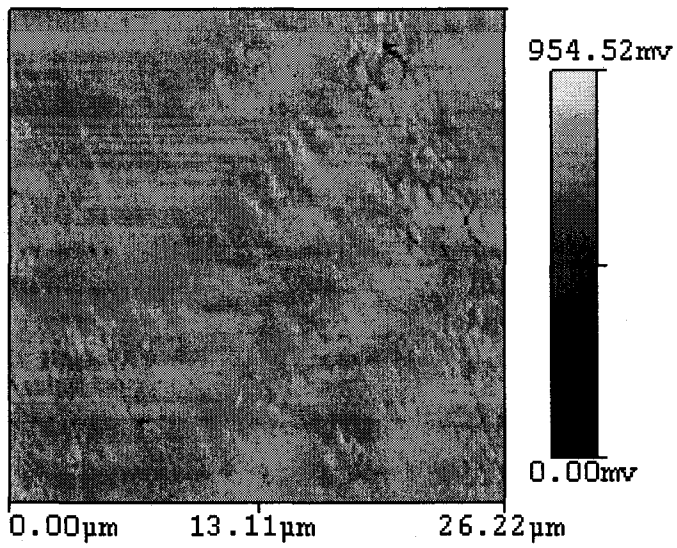

b) FFM image

Figure 7.5: Pure tungsten surface.

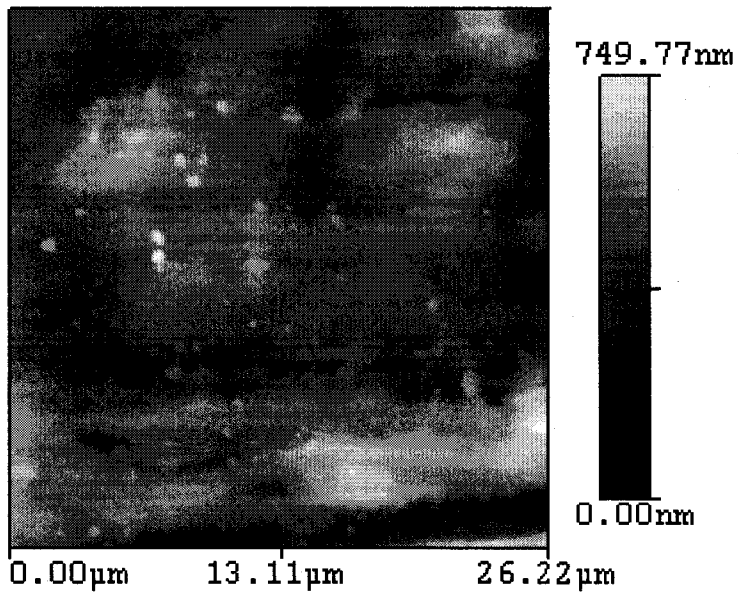

a) Topology image

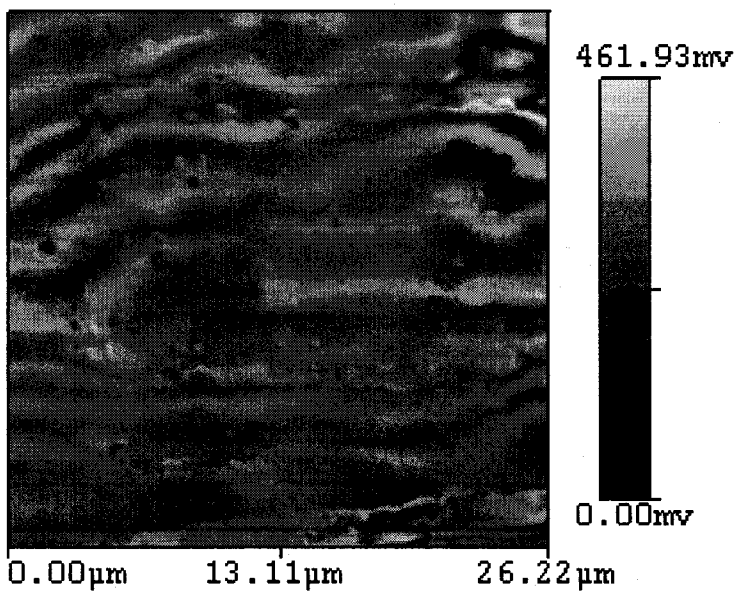

b) FFM image

Figure 7.6: Tungsten boronized at 940^{O}C for 4 hours.

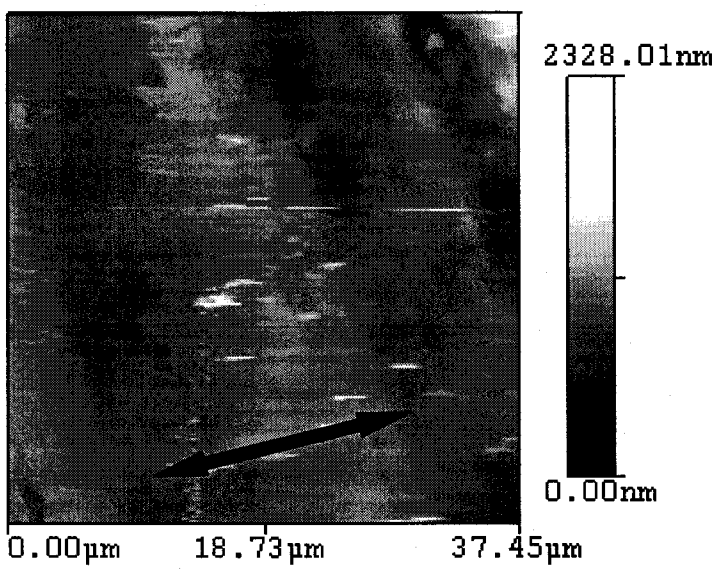

a) Topology image

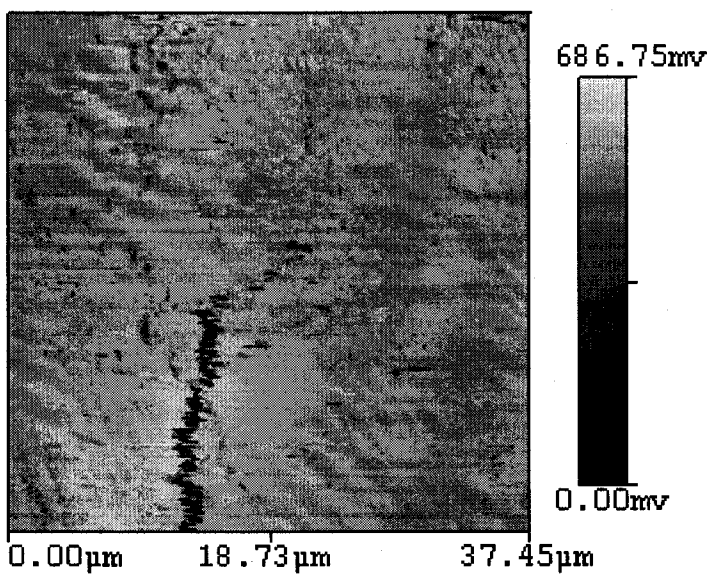

b) FFM image

Figure 7.7: Tungsten wear track.

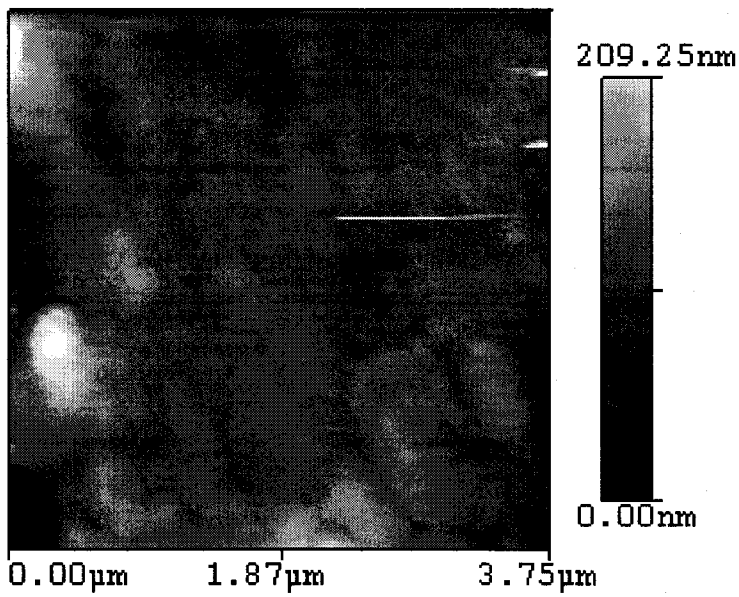

a) Topology image

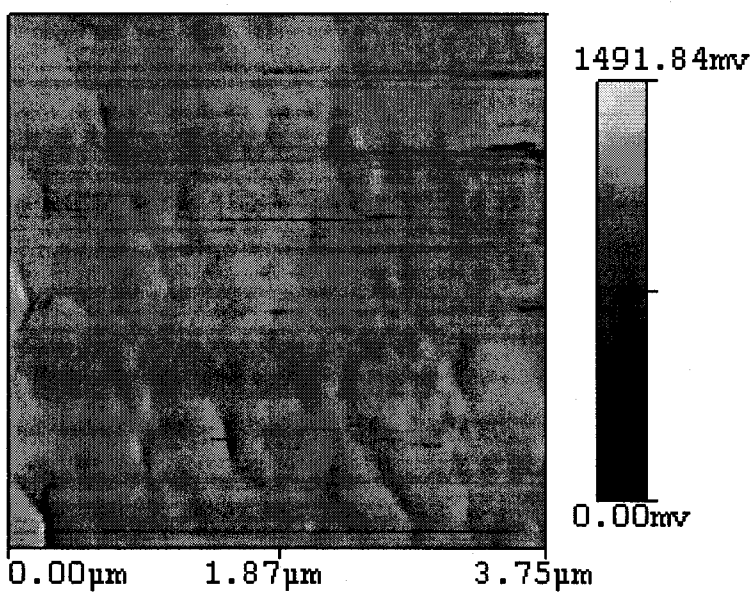

b) FFM image

Figure 7.8: Debris of tungsten substrate.

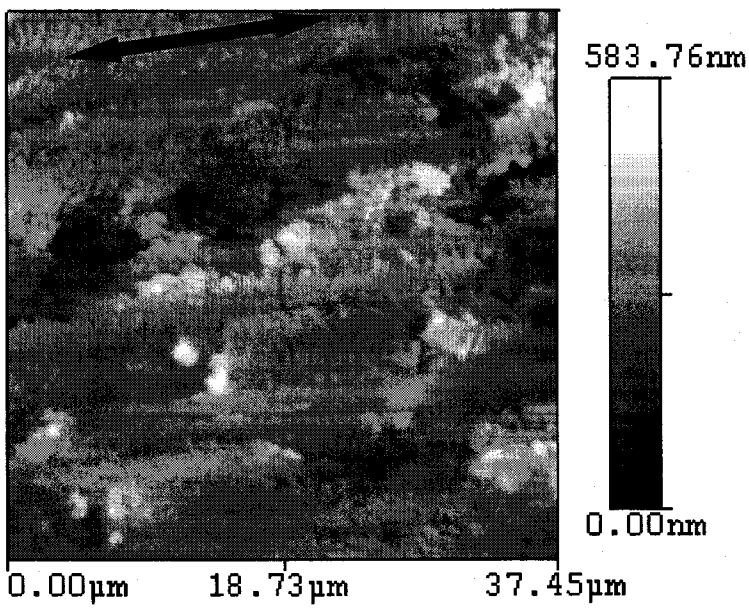

Figure 7.9: Topology image of wear track on boronized tungsten.

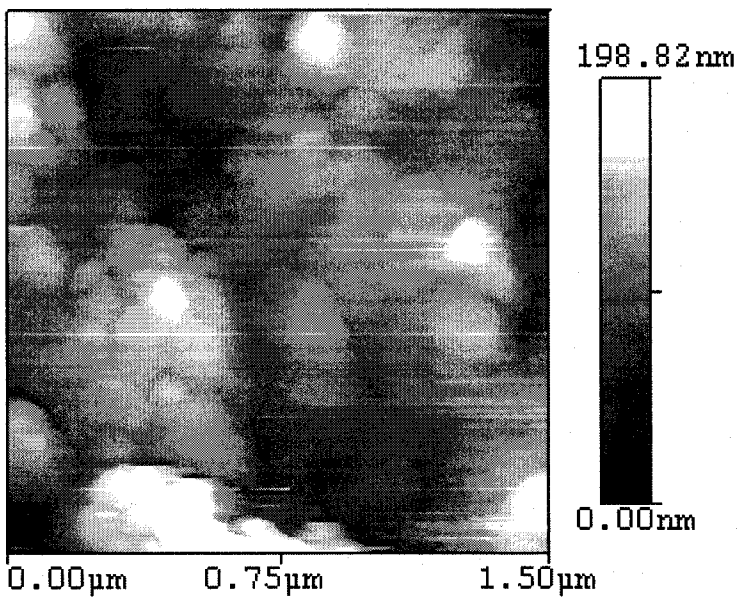

a Topology image

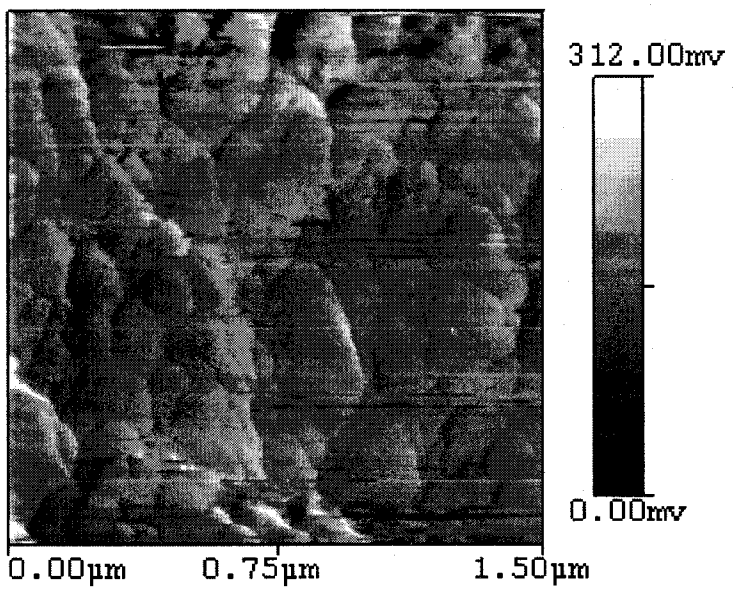

b FFM image

Figure 7.10: Debris formed during sliding of boronized tungsten with the bearing ball.

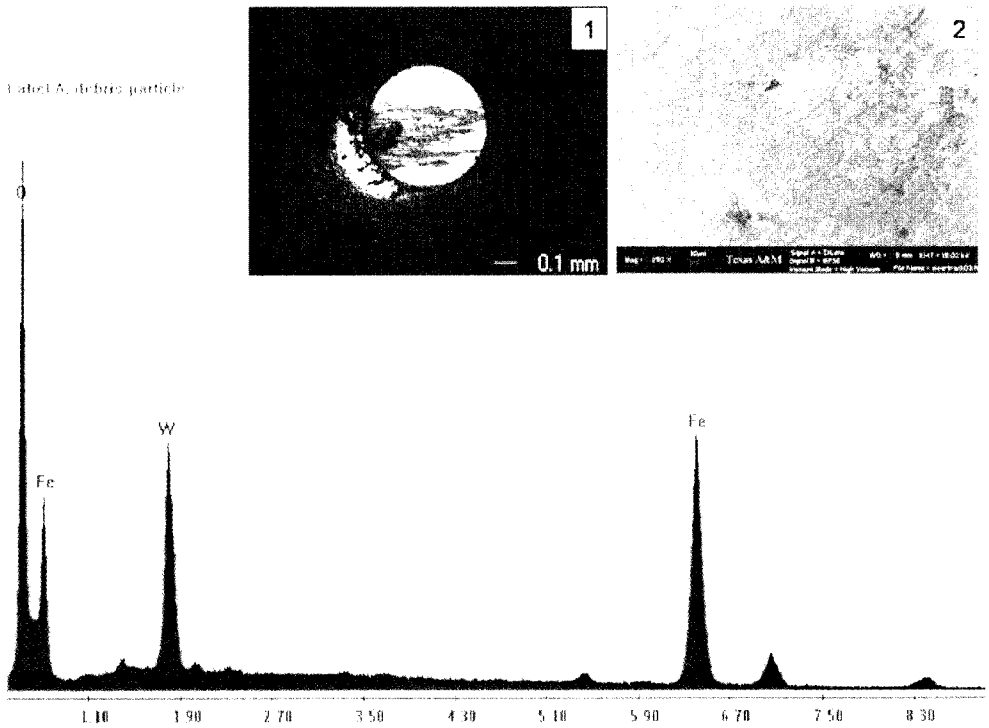

Figure 7.11: The EDS spectrum taken on debris lying on the wear track. (Inset 1: Wear scar on the bearing ball. Inset 2: Debris particles on the wear track).

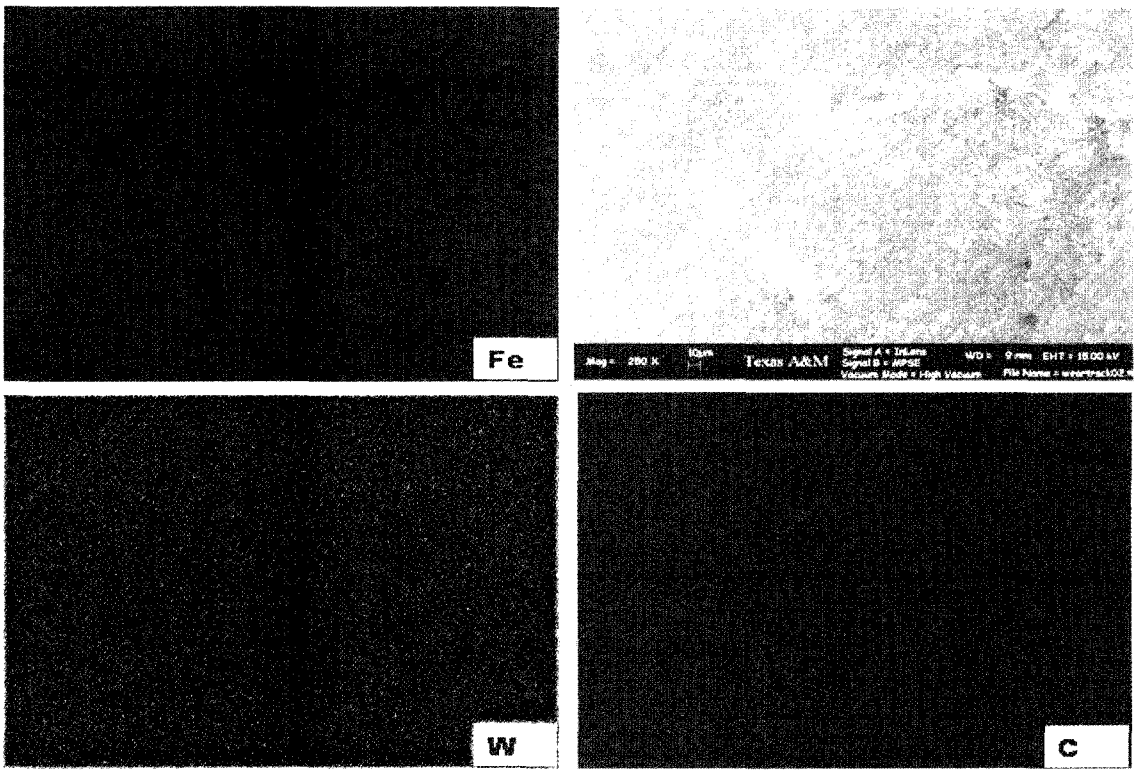

Figure 7.12: Element mapping on the worn surface of boronized tungsten.

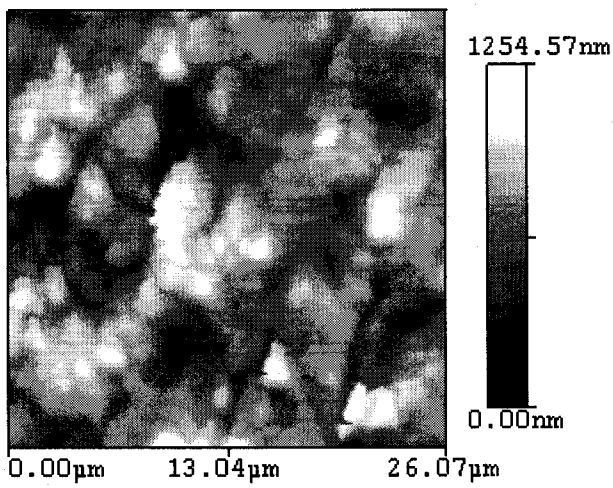

a) Topology image

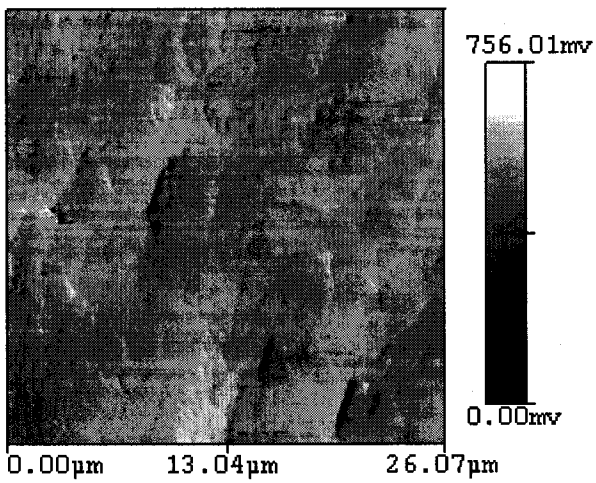

b) FFM image

Figure 7.13: Boronized niobium surface.

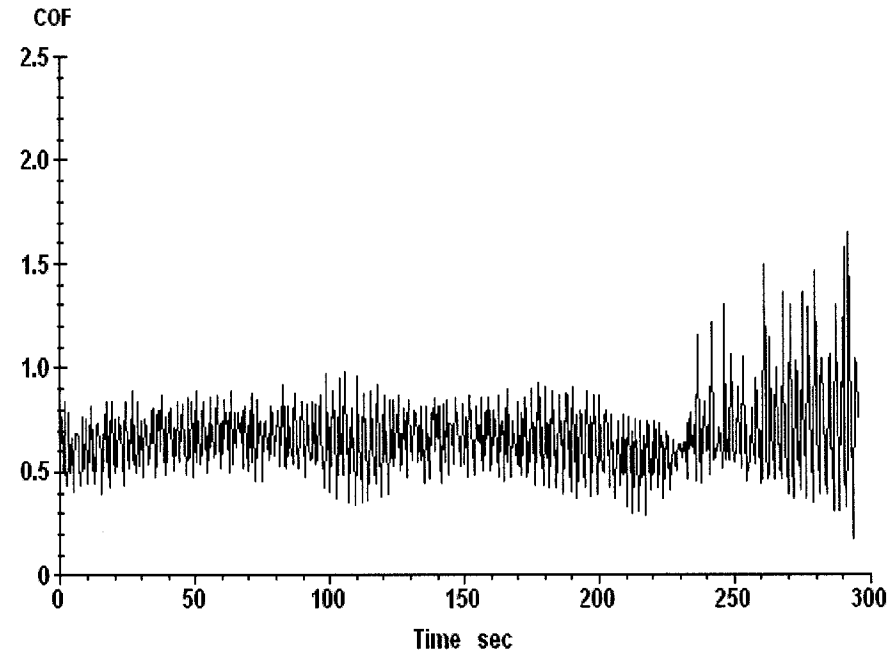

Figure 7.14: Coefficient of friction vs. time.

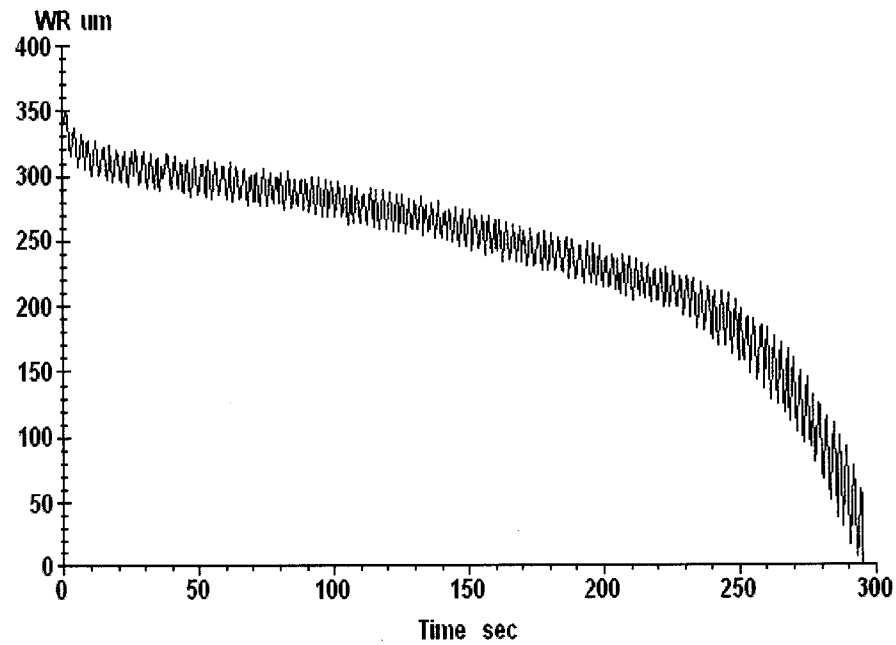

Figure 7.15: Niobium boride coating wear rate (pin movement).

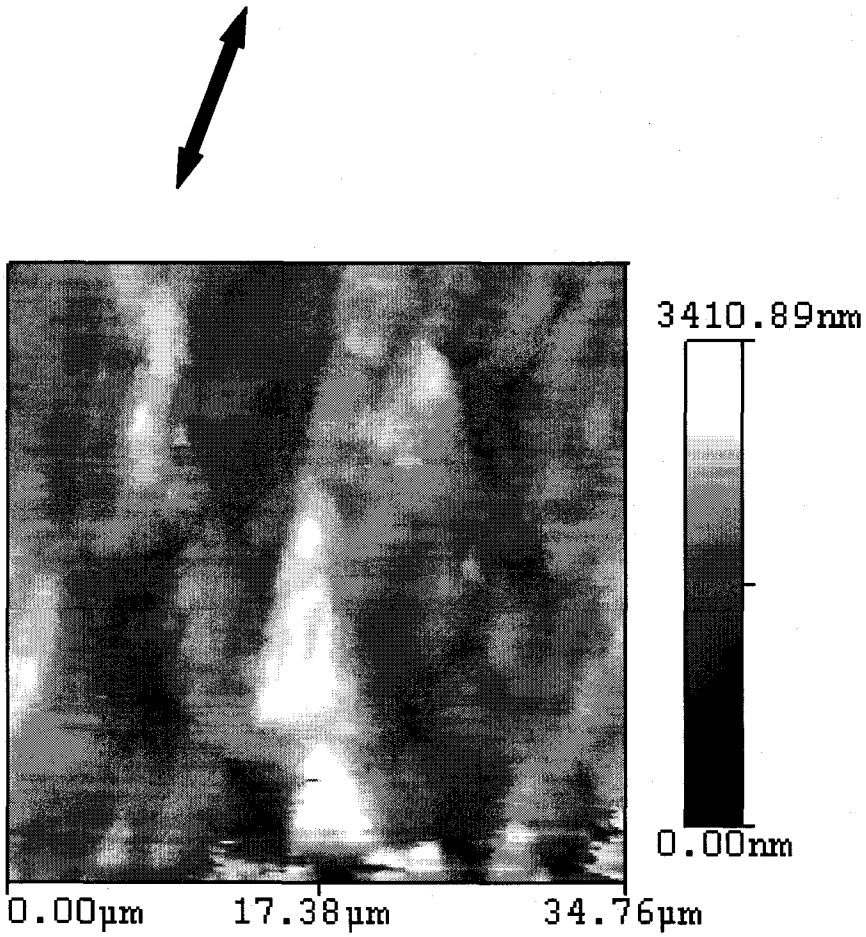

Figure 7.16: Topology image of boronized niobium wear track.

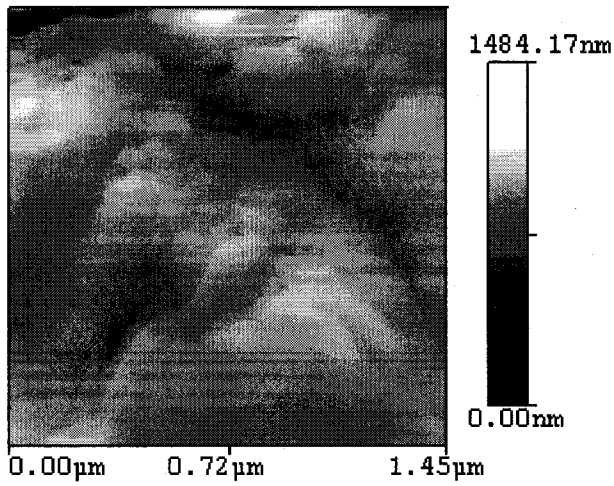

a) Topology image

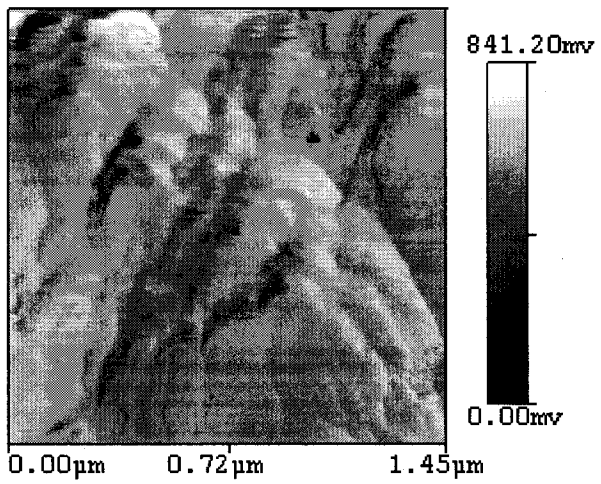

b) FFM image

Figure 7.17: Debris formed during sliding of niobium boride and the bearing ball.

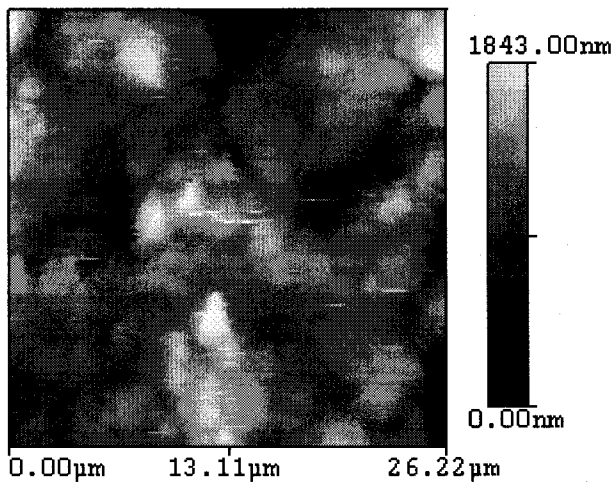

a) Topology image

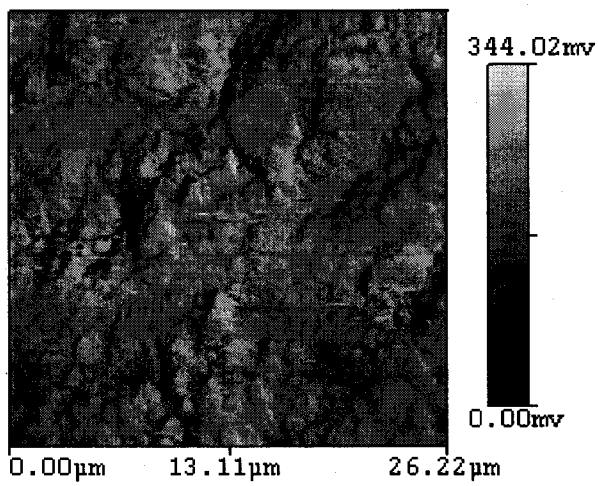

b) FFM image

Figure 7.18: Boronized tantalum surface.

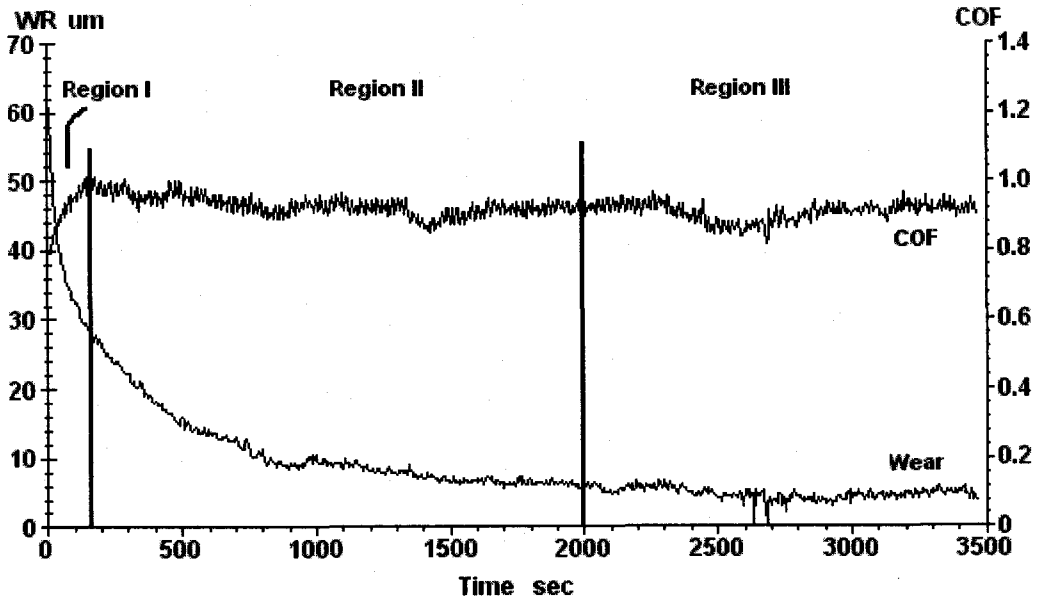

Figure 7.19: Plot of coefficient of friction and reduction in pin height vs. time.

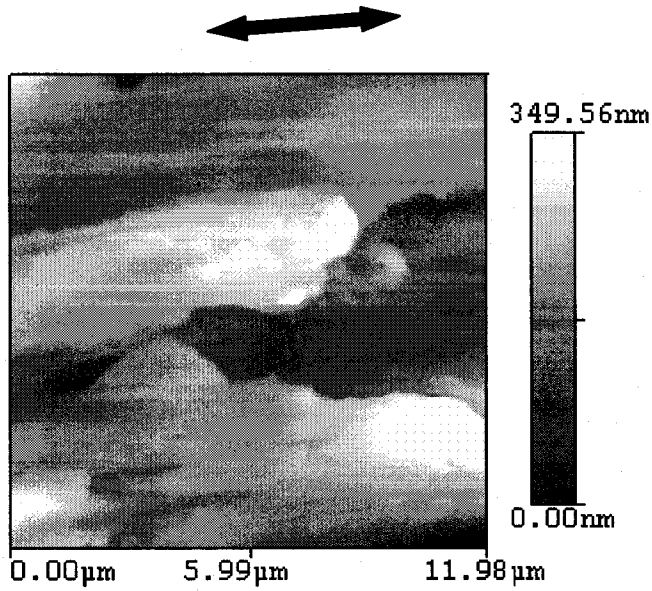

Figure 7.20: Wear track formed during sliding of boronized tantalum with the bearing ball.

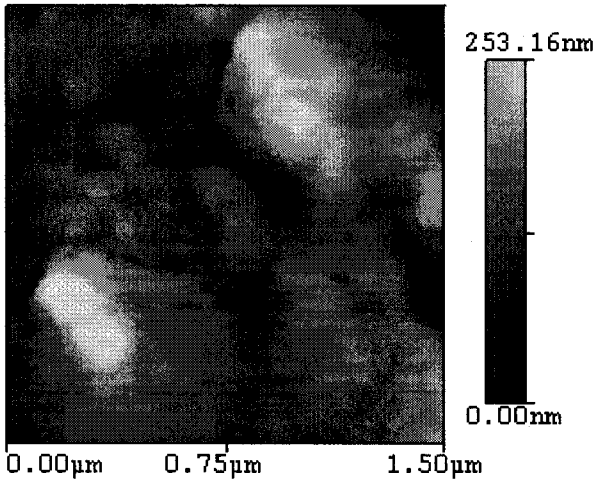

a

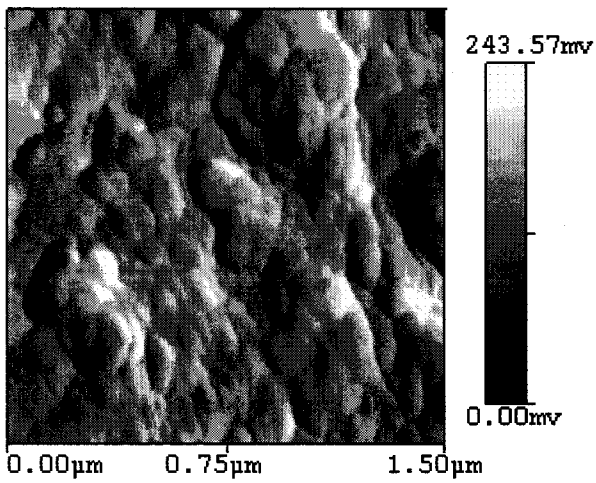

b

Figure 7.21: Debris formed during sliding of boronized tantalum and the bearing ball.

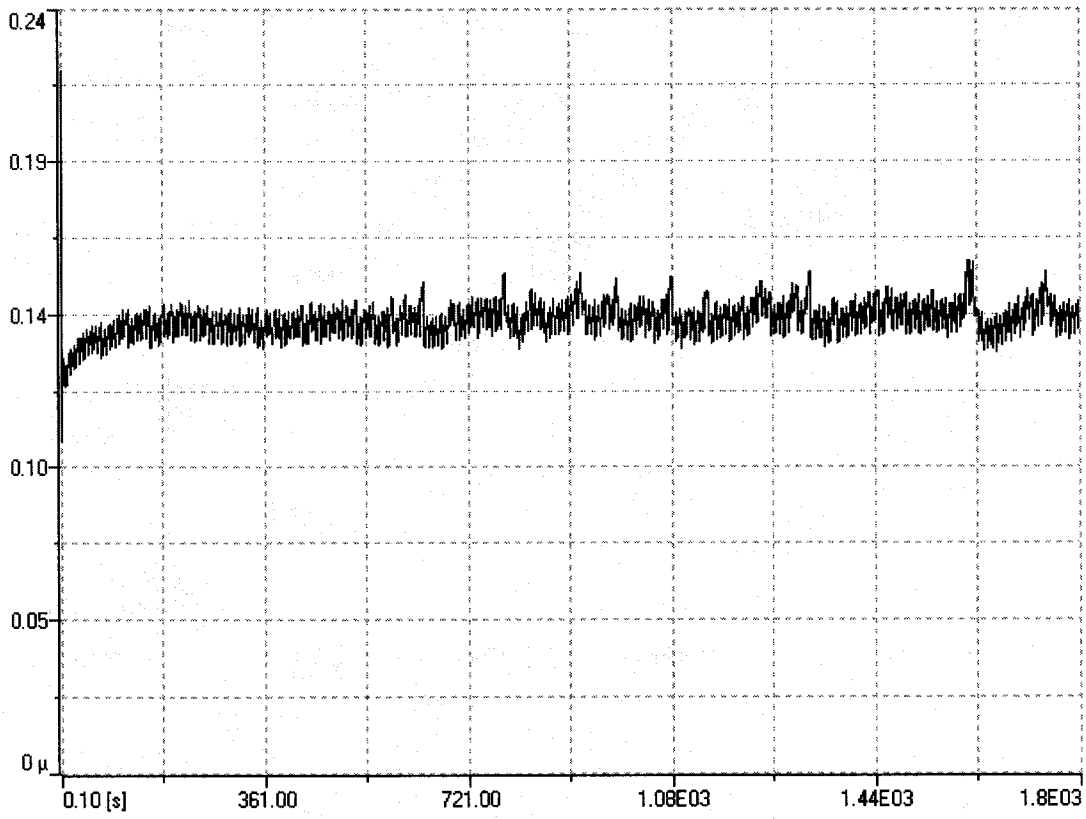

Figure 7.22: Coefficient of friction plotted against time for boronized tungsten slid against the bearing ball in SBF.

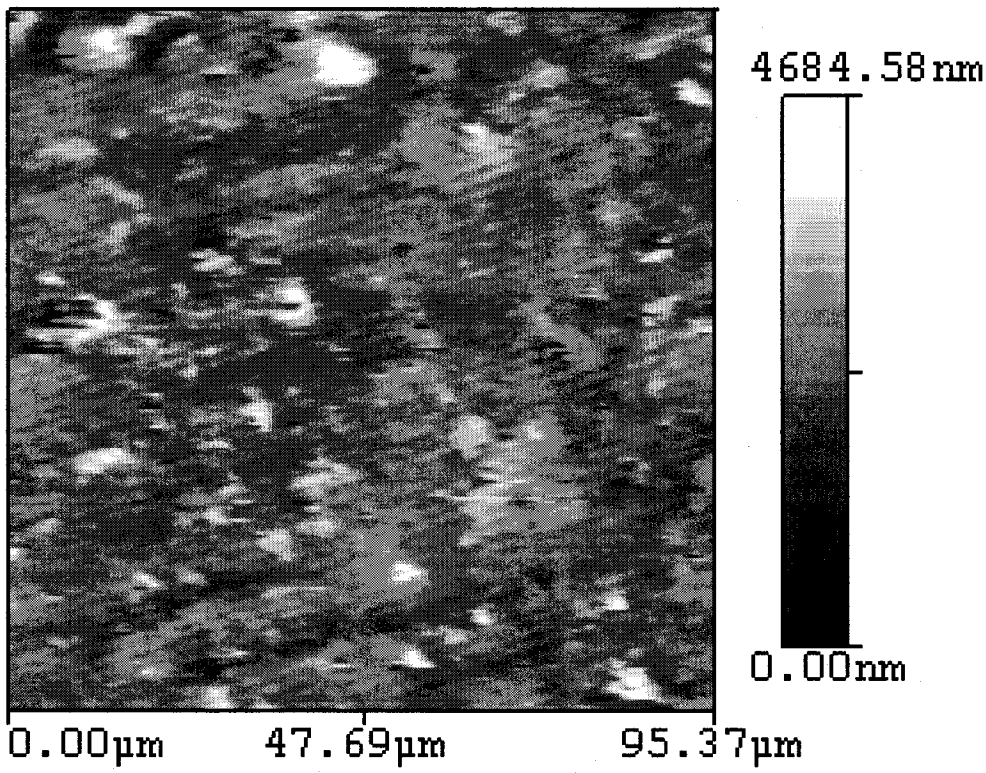

Figure 7.23: Wear track formed on boronized tungsten during sliding with the bearing ball in SBF.

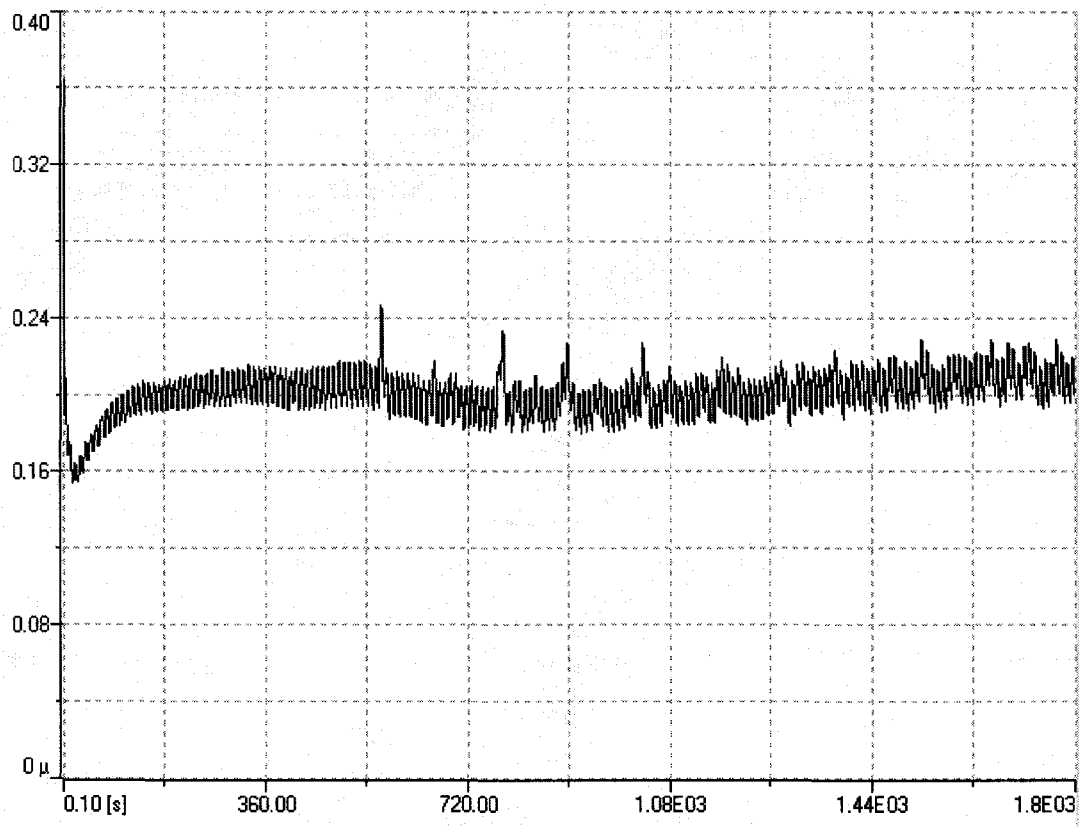

Figure 7.24: Coefficient of friction plotted against time for boronized niobium slid against the bearing ball in SBF.

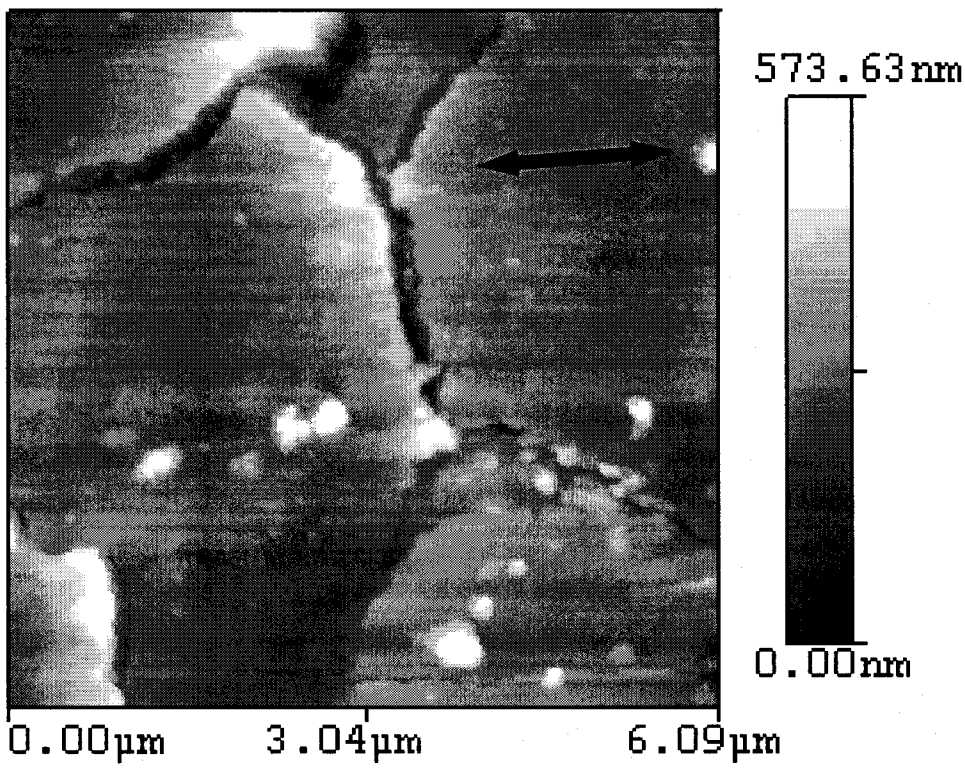

Figure 7.25: Wear track formed on the surface of boronized niobium during sliding with the bearing ball in SBF.

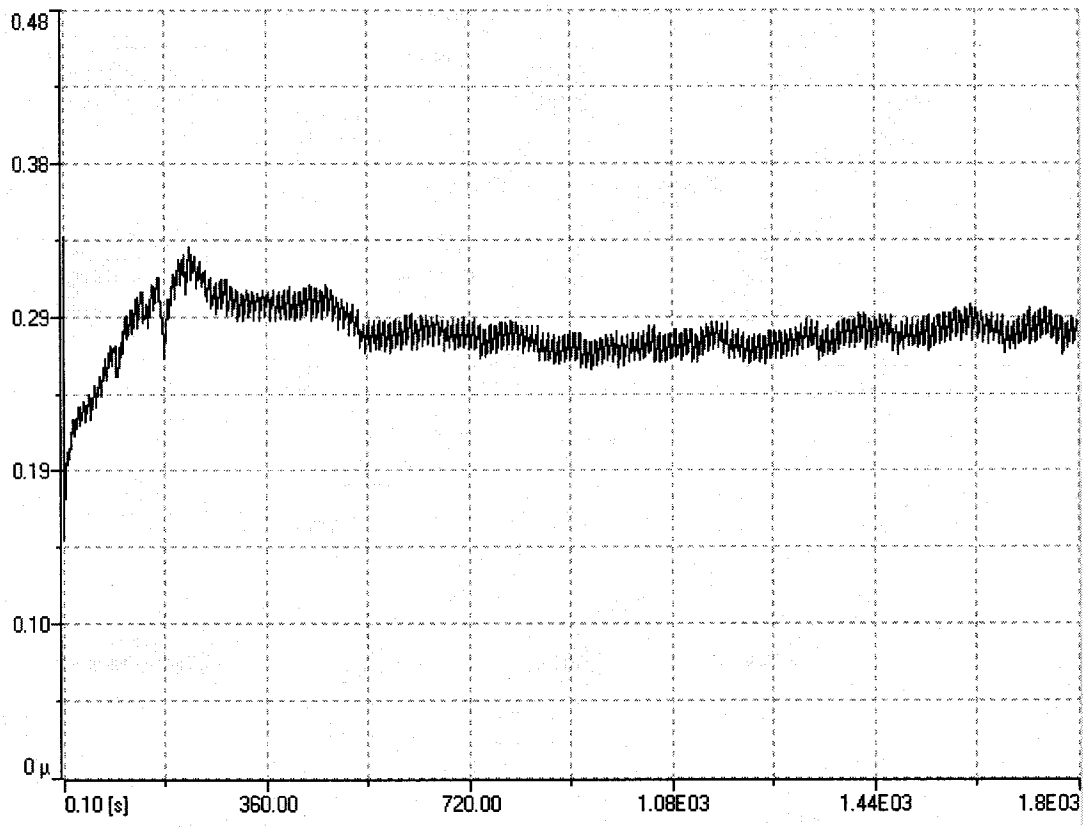

Figure 7.26: Coefficient of friction plotted against time for boronized tantalum slid against the bearing ball.

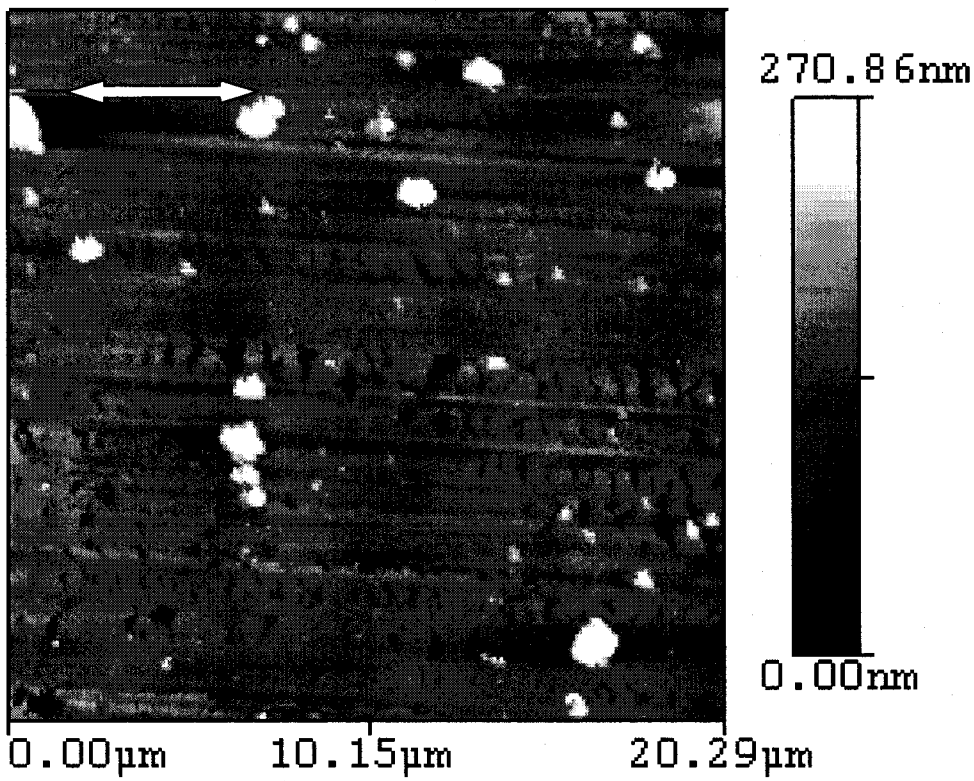

Figure 7.27: Wear track formed on boronized tantalum during sliding with the bearing ball.

Table 7.1 : Roughness of refractory metals and boronized refractory metals.

Materials	Surface Roughness Ra
Tungsten	1.32
Chromium	--
Boronized Tungsten	0.29
Boronized Niobium	1.26
Boronized Tantalum	1.15
Boronized Chromium	--

Table 7.2: Coefficient of friction of refractory metals and boronized refractory metals in dry conditions.

Materials	Coefficient of friction against the bearing ball
Tungsten	0.18
Chromium	--
Boronized Tungsten	0.75
Boronized Niobium	0.66
Boronized Tantalum	0.92
Boronized Chromium	--

Table 7.3: Coefficient of friction of refractory metals and boronized refractory metals in Simulated Body Fluid (SBF).

Materials	Coefficient of friction against bearing pin
Tungsten	--
Chromium	--
Boronized Tungsten	0.14
Boronized Niobium	0.20
Boronized Tantalum	0.28
Boronized Chromium	--

Table 7.4: Inorganic ion composition (mmol/liter) of Simulated Body Fluid.

	Na^+	K^+	Mg^{2+}	Ca^{2+}	Cl^-	HPO_4^{2-}	SO_4^{2-}	HOC_3^-	pH
Composition	142.0	5.0	1.5	2.5	147.8	1.0	0.5	4.2	7.4

7.4 Discussion

7.4.1 Wear Mechanism Study in Dry Conditions

7.4.1.1 Tungsten and Boronized Tungsten

7.4.1.1.1 Tribological Properties of Tungsten Substrate and Boronized Tungsten

The surface roughness of pure tungsten and boronized tungsten are listed in Table 7.1. Compared to pure tungsten boronized tungsten has a smoother surface.

The change in the coefficient of friction with time shows three distinct regions (I, II, III). It was observed that initially the coefficient of friction increased relatively quickly until the time reached 200 seconds (region I). This is the "break-in" or "running-in" region as explained by Rigney [15], where the initial rough surface smoothes due to a high friction force. After the "break-in" region, the change in the coefficient of friction slowed down (region II); Region II occurred from 200 to 3250 seconds. The friction stabilized after region II, entering region III (Figure 7.1).

The pin surface height reduction with time in Figure 7.2 also is divided into three different regions (i.e. I, II, III). These three regions correspond to those of the friction change discussed above. It was found that the pin surface height (due to linear wear) decreased with time until after 3250 seconds. This decrease was fast initially, for about 200 seconds (i.e. region I). After that and until 3250 seconds, this change in surface height was relatively slow (i.e. region II). In region III, this change was very slow. In the case of pure tungsten, however, the initial break-in period was very short. The coefficient of friction between pure tungsten and the steel pin is given in Table 7.2.

In case of boronized tungsten, the curve of the coefficient of friction with time (Figure 7.3) can be divided into three distinct regions (regions I, II, III). The change in the coefficient of friction in the first 200 seconds was fast (region I). This change was very slow from 200 seconds to 2000 seconds (region II), and thereafter it stabilized (region III).

For boronized tungsten, the surface height change (wear) was larger than that of pure tungsten (Figure 7.4). The surface height continuously decreased over time; but there were three different regions of surface height change. During the first 200 seconds, it decreased quickly (region I). The rate was intermediate from 200 seconds to 2000 seconds (region II), and thereafter it was very slow. The initial break-in period was different from the later period, and the coefficient of friction and surface height were relatively constant.

Although the surface roughness of boronized tungsten is lower than that of pure tungsten, the boronized tungsten shows a more pronounced running-in period in friction. Both materials have similar behavior in the change in the pin surface height, which can be correlated to linear wear. This phenomenon means that wear mechanisms differ for these two materials.

7.4.1.1.2 Wear Mechanisms of Tungsten Substrate and Boronized Tungsten

The topological image in Figure 7.5a shows the polished tungsten surface. This initial topology of the polished tungsten substrate was used for boronizing. The grooves

formed during polishing prior to boronizing are also visible in this image. The FFM image (Figure 7.5b) indicates uniform friction (between the AFM probe and the surface) across the surface. The visible variation in FFM is due to surface grooves present on the surface. Figure 7.28a, the line profile of the tungsten surface, shows grooves. Figure 7.28b shows the corresponding variation in friction. The higher friction corresponds to the peak of a groove. The surface of pure tungsten used for boronizing does not contain any other impurities, like foreign particles, which are not desirable during boronizing.

Formation of the boride layer on the tungsten surface was confirmed both in SEM (Figure 3.3) and in AFM (Figure 7.6). The topology of the borides shown in Figure 7.6a is continuous and uniform on the surface. There were few foreign particles (size around 0.5μm) present on the layer. These particles might be introduced during boronizing. The X-ray study showed that the single-phase borides (i.e., WB) were formed on the surface, but the FFM image shows the different FFM to the cantilever tip on the boronized tungsten surface (Figure 3.9).

During the sliding action with a continuous load, the tungsten substrate underwent plastic deformation. Initially, wear took place at the peaks of the grooves. These grooves underwent plastic deformation and were flattened. The topology of such deformed grooves is obvious in Figure 7.7a. The variation in FFM is due to the surface roughness. As flattening went on, the surface height reduction slowed down.

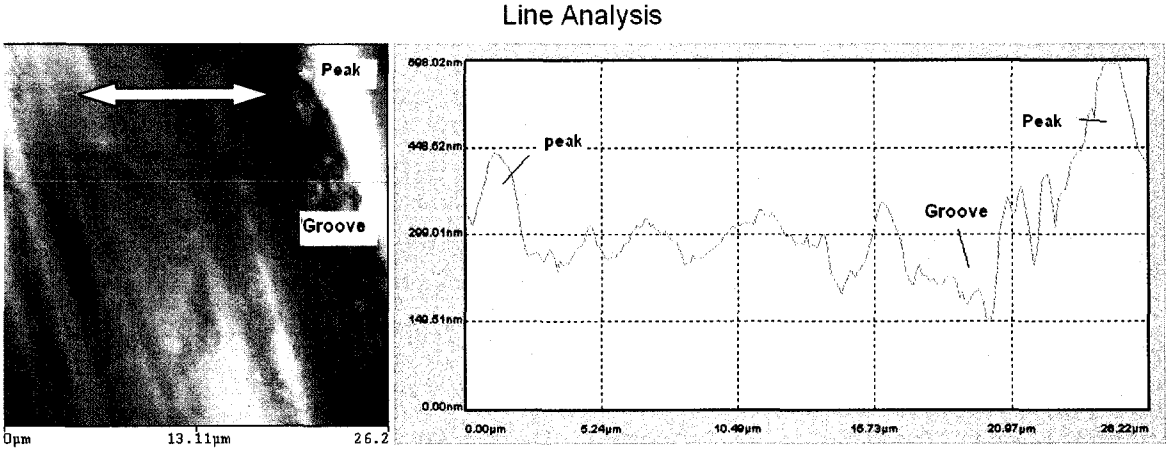

Figure 7.28: a) The line profile on pure tungsten; showing the peaks and the grooves.

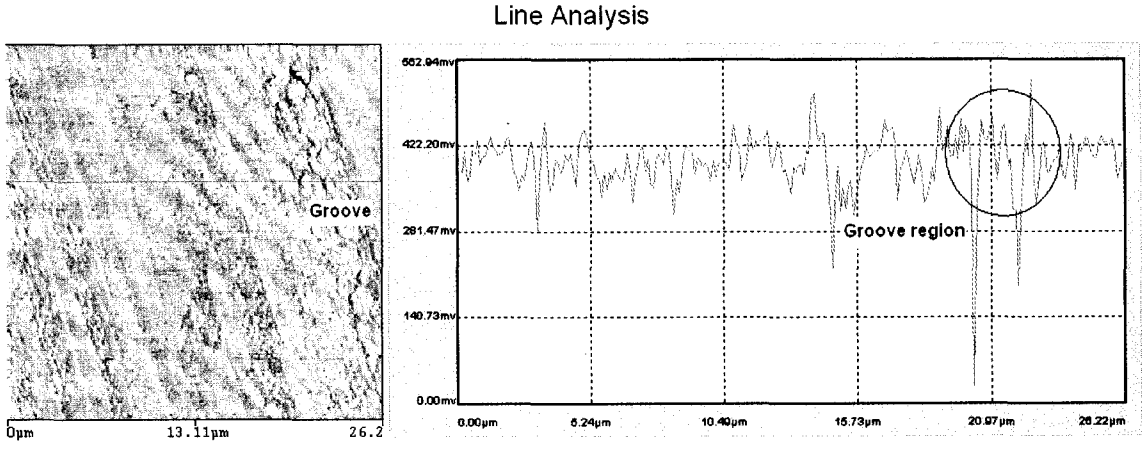

b

Figure 7.28: b) The friction variations on tungsten due to the presence of peaks and grooves; the circle represents the groove region showing variation in friction.

During sliding, both the mating surfaces underwent continuous deformation and adhesive interaction. The fact that debris was detached from either surface was due to the ductile fracture. Upon detaching from the mating surfaces, if these particles interacted with the sliding surfaces as a third body, they underwent further severe deformation. The topology of debris shown in Figure 7.8a, which shows clear evidence of deformed debris. The detached particles are connected due to adhesion. The FFM image shows uniform friction. Therefore, the debris formed has mechanical properties similar to those of the original surface.

The observation of the boronized tungsten wear track at the micron level indicated that the wear is abrasive in nature. The topology of the surface in Figure 7.9a shows the abrasive grooves on the worn surface. The single-phase tungsten boride present on the surface is a hard and brittle intermetallic compound. Upon detaching from the surface, the hard debris particles are involved in third body wear. These hard particles are further involved in the abrasion of mating surfaces and fail by fracture. The topological image of the debris in Figure 7.10a presents nano sized debris particles. The particle boundaries are very clear, and the size of these particles ranges from a few tenths of a nanometer to a few hundredths of a nanometer. Intergranular fracture might be the reason for these size variations. The AFM analysis in Figure 7.10b indicates that the debris has uniform mechanical properties, which is shown by its uniform friction with the AFM cantilever tip.

The composition study of the material transfer from either sliding material using an energy dispersive x-ray analysis (EDS) showed that the debris consists of iron from the bearing ball and tungsten from the boronized tungsten layer (Figure 7.11). The element distribution by element mapping using EDS on the wear track showed that the surface consists mainly of W, while the debris particles contain Fe and C (Figure 7.12).

The abrasive wear at the micro level does not explain the atomistic behavior of materials. It is essential to study the wear mechanism at a further, lower-length scale. The wear of the surface at the atomic level is the fundamental wear phenomenon that occurs first and transforms to other wear mechanisms at higher length scales. Further investigation of the wear mechanisms of boronized tungsten at smaller length scales using AFM showed that boronized tungsten underwent wear via different types of wear mechanisms at these length scales. At a nanometer length scale, a fracture is seen as the small cracks shown in Figure 7.29. These cracks initiated from the surface and penetrated into the surface, causing fracture. It is possible to do line analysis and observe cracks in 3D view using the Nano Rule. Figure 7.30a shows the line analysis of the image taken at very high resolution, indicating the deep cracks. Figure 7.30b shows the cracks running into the surface in 3D view.

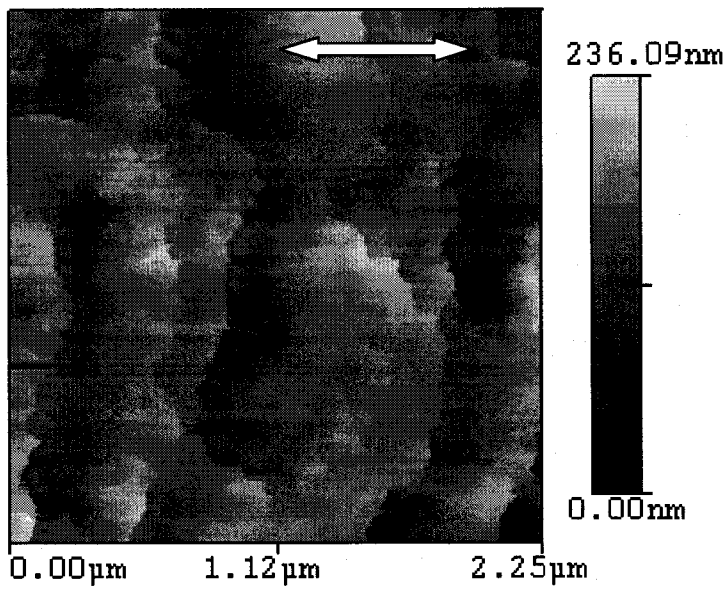

Figure 7.29: Topological image of cracks formed on the surface at nano scale.

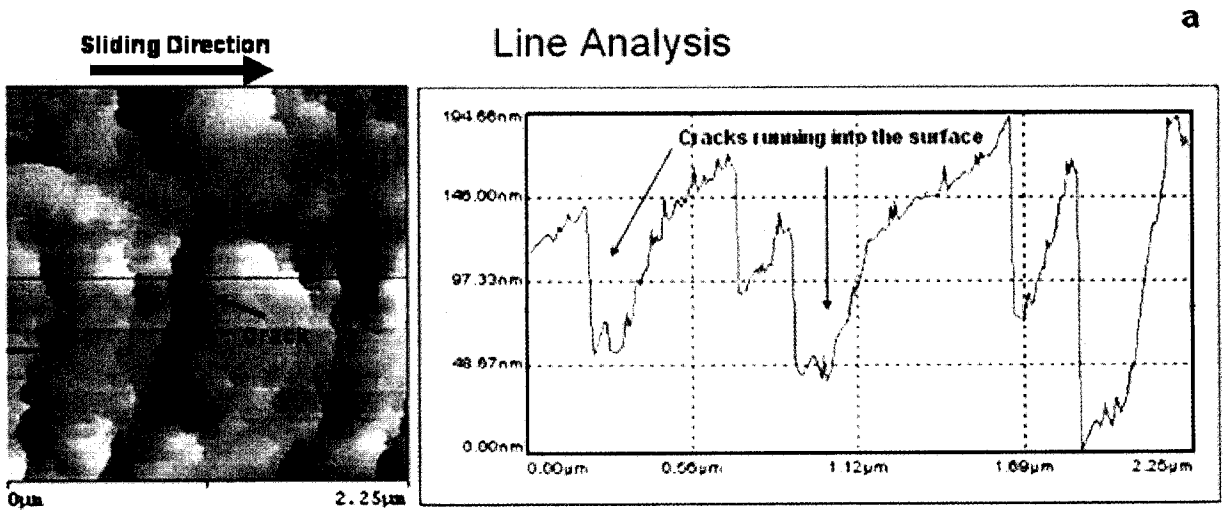

a) Line analysis

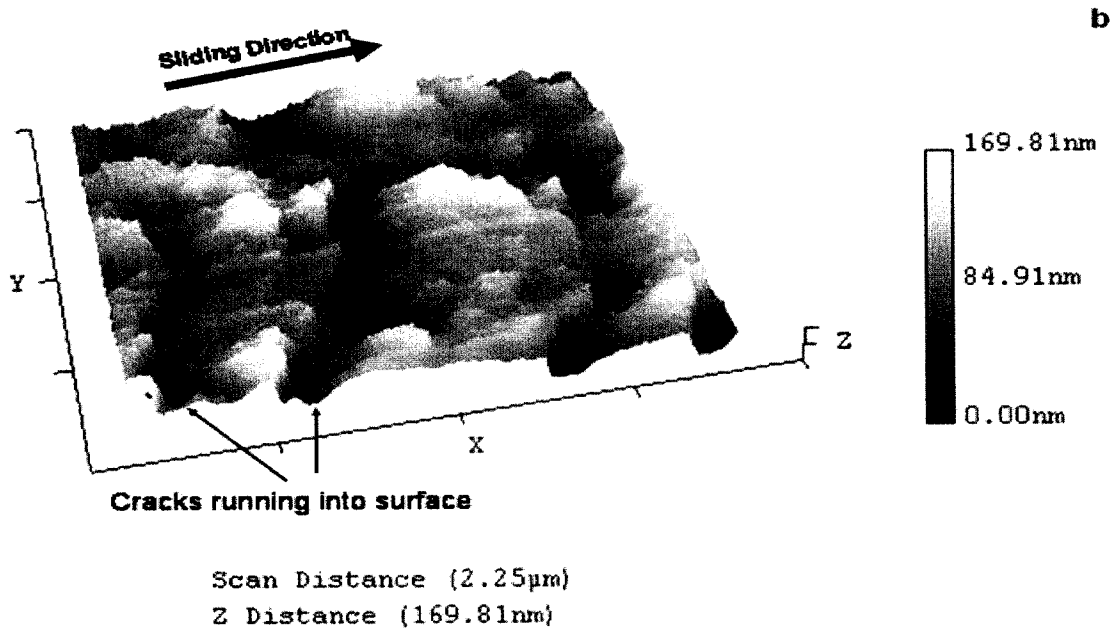

b) 3D view

Figure 7.30: Cracks on the surface at nano scale.

7.4.1.2 Boronized Niobium

7.4.1.2.1 Tribological Properties of Boronized Niobium

The SEM image in Figure 3.5 confirmed the formation and distribution of the borides formed on the niobium surface. The topological image in Figure 7.13a also provides the evidence of the formation of continuous borides on the surface of pure niobium. The flow of the grains is along a particular direction that might be the direction of the initial scratches on the surface. This direction was the sliding direction during friction and wear tests. After careful study of the topology and the FFM images of both directions, it was found that the FFM image in Figure 7.13b shows uniform friction between the cantilever tip and the boride surface.

The friction test was stopped at 300 seconds as the pin height reduction was very fast. It was found that surface height decreased with time until after 300 seconds. This decrease was fast initially, for about 60 seconds. After that the change in surface height was relatively slow for about 250 seconds. Towards the end of the test, this change was very fast. This might be simply the "breaking-in" period, but the friction coefficient did not change even though the surface height reduction was very fast. This might indicate that there is no relation between the coefficient of friction and the wear rate (Figures 7.14 and 7.15).

7.4.1.2.2 Wear Mechanisms of Boronized Niobium

The wear test was conducted for a very short period of time. There is no indication of severe wear, but the elongated grains in the sliding direction show the deformation of the surface. Figure 7.16 shows the elongated grain-like structures along the sliding direction. As the sliding time was less, a small amount of debris was formed on the wear track. The debris shows a clear layer-like structure (Figure 7.17). It is an indication of accumulated, compressed debris. The boride coating underwent plastic deformation during the sliding action with a continuous load. The debris layer is uniform in mechanical properties, as the FFM image shows uniform friction.

7.4.1.3 Boronized Tantalum

7.4.1.3.1 Tribological Properties of Boronized Tantalum

The surface roughness of boronized tantalum is listed in Table 7.1. The borides formed on the surface show grains of different sizes and shapes. Most of the grains are spherical in shape (Figure 7.18a). Upon careful study of the FFM image in both forward and backward directions and the accompanying topology image, the FFM image shows a similar frictional response to the cantilever tip on the boride surface (Figure 7.18 b).

The "break-in" or "running-in" region was observed in the friction against time plot (Figure 7.19). This period indicates that the initial rough surface was smoothened due to higher friction [15]. After the "breaking-in" period, this type of distinct region disappeared and friction stabilized. The trend in a downward movement of the pin was

similar to that of boronized tungsten and can be divided into the three regions given in Figure 7.19. The initial reduction in movement of the pin was fast until 150 seconds, and was moderate until 2000 seconds, and was very slow thereafter. There is difference in the frictional behavior. The friction stabilized earlier after a break-in period; i.e., after 150 seconds.

7.4.1.3.2 Wear Mechanisms of Boronized Tantalum

Figure 7.20 is the topology image on the wear track of the boronized tantalum. It is clear from this figure that the wear is due to abrasion and fracture. The topology of debris in Figure 7.21b shows the clear individual grains of different sizes. It is an indication that the fragments separated from boronized tantalum are continuously compressed, and failed due to fracture. The debris particles are uniform in mechanical properties, as the FFM image shows uniform friction.

The study of wear mechanisms of different refractory borides in dry sliding conditions showed that the conventional methods of studying the wear mechanisms are not sufficient to conclude that the basic wear mechanisms were involved in the failure of the surfaces. It was found that the wear mechanisms at the nano level are quite different from those at the length scale of conventional study. It was also found that there is no direct relation between the coefficient of friction and the wear of the boronized layer.

7.4.2 Wear Mechanisms of Boride Coatings in Simulated Body Fluid

The chemical composition of the simulated body fluid used as lubricant in this investigation is given in Table 7.4 [16]. The simulated body fluid is slightly acidic in nature. The effects of simulated body fluid (SBF) fluid on the topology of the boronized refractory metals during wear are carefully considered here. The present study focuses on only the surface effects.

7.4.2.1 Wear Behavior of Boronized Tungsten

7.4.2.1.1 Tribological Properties of Boronized Tungsten

The coefficient of friction between boronized tungsten and the steel ball in the presence of SBF is listed in Table 7.3. The initial break-in period lasts for 150 seconds, until the friction is stabilized (Figure 7.22). This period is shorter than the break-in period for the dry test. In the SBF fluid, a lower coefficient of friction was observed between boronized tungsten and the steel ball. Most likely, this is due to the surface modification induced by SBF. A discussion of the evidence follows.

7.4.2.1.2 Wear Mechanism of Boronized Tungsten

The topology image of the wear track in Figure 7.23 shows that the failure of the surface is due mainly to abrasive wear that occurs at the micrometer-length scale. A large amount of debris was observed on the wear track. The nano scale cracks, which were observed on the wear track in the dry sliding test, were not observed on the wear track in the wet sliding tests. Apparently, the SBF works as a vehicle to carry the debris out of the

wear track during sliding. Furthermore, it can be seen that shear forces on the surface are reduced by the presence of the SBF fluid, so that less material is removed.

7.4.2.2 Wear Behavior of Boronized Niobium

7.4.2.2.1 Tribological Properties of Boronized Niobium

The coefficient of friction between boronized niobium and the steel ball in the presence of the SBF fluid is given in Table 7.3. The value of the coefficient of friction was lower in wet than in dry conditions. Similar that for dry conditions, an initial break-in period was observed. At the beginning, the coefficient of friction increased for the first 180 seconds, and then stabilized (Figure 7.24).

7.4.2.2.2 Wear Mechanism of Boronized Niobium

It was found that the wear modes of a boronized surface in wet conditions were totally different from those in dry conditions. There are surface cracks as shown in Figure 7.25. These cracks appear at the micrometer length scale on the surface. There might be some reactions between the SBF and the surface. The line analysis in Figure 7.31 shows that the crack depths are around a few hundred nanometers.

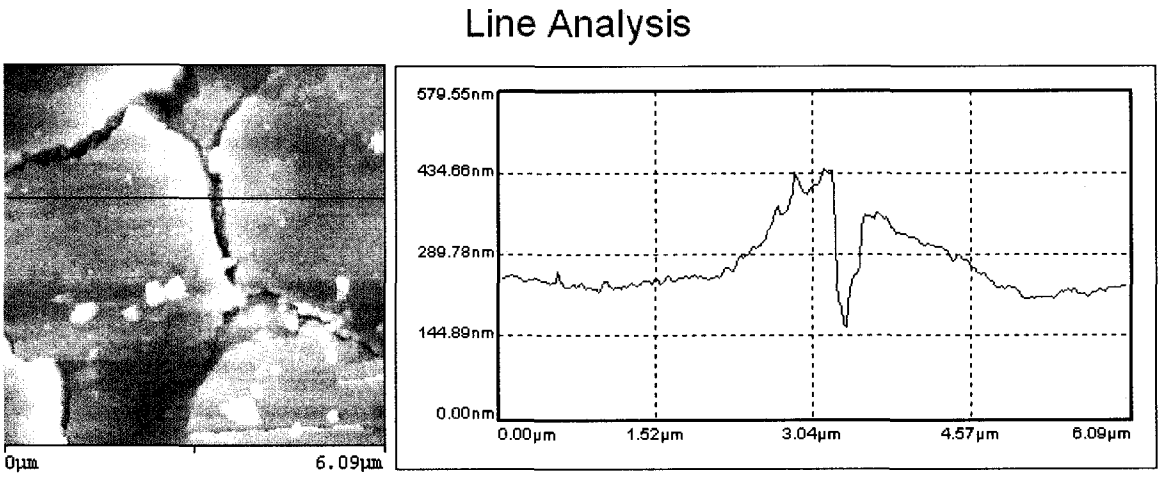

Figure 7.31: Line analysis of the worn surface of boronized niobium.

The study of the surfaces at higher magnification using the AFM (Figure 7.32) shows that at the nanometer length scale, the boronized niobium failed by fracture. This wear behavior is totally different from the micrometer length scale wear.

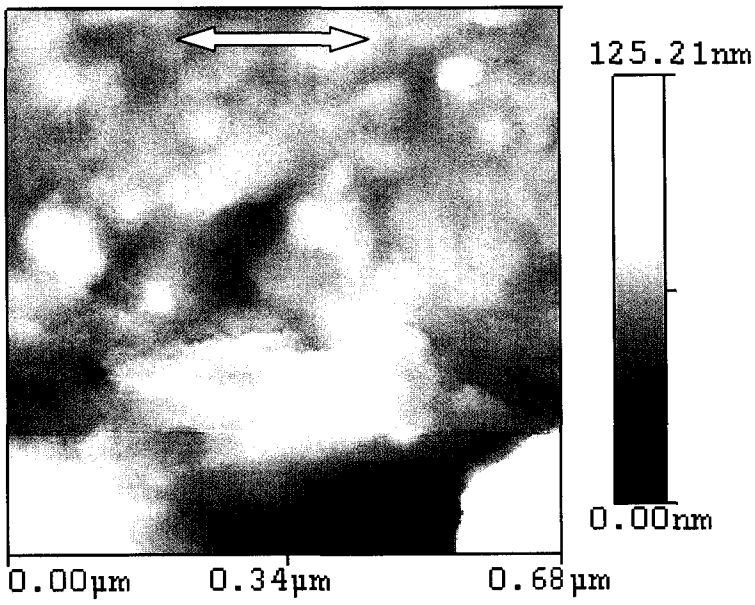

Figure 7.32: Nanometer length scale wear of boronized niobium. An arrow indicates the sliding direction.

7.4.2.3 Wear Behavior of Boronized Tantalum

7.4.2.3.1 Tribological Properties of Boronized Tantalum

The coefficient of friction between the boronized tantalum and the steel ball in the presence of SBF fluid is given in Table 7.3. The initial break-in period was different from that in dry conditions. The highest value of the coefficient of friction was achieved in this period. After the initial break-in period, the friction was stabilized (Figure 7.25). The value of the coefficient of friction is much lower than that in dry conditions.

7.4.2.3.2 Wear Mechanism of Boronized Tantalum

Similar to previous materials, boronized tantalum worn in SBF shows totally different wear behavior compared to that in dry conditions. The presence of SBF and its interactions with the sliding surfaces is responsible. Our previous investigations of the effects of SBF on polymers, ceramics, and metals have shown the strong effects of SBF [17]. At the micrometer length scale, clear abrasive grooves were observed on the wear track; as shown in Figure 7.26. The detached particles of tantalum boride further deteriorated the surface.

Further analysis using an AFM at the nanometer length scale was conducted. Results reveal more insight into the wear mechanisms of boronized tantalum that were not observed otherwise at higher length scales. The nanofracture and nanocracks on the surface which are shown in Figure 7.34 were observed. The cracks on the surface were

perpendicular to the sliding direction. The arrow indicates the sliding direction. Intergranular fracture was observed within the grains and was in a wide range of sizes.

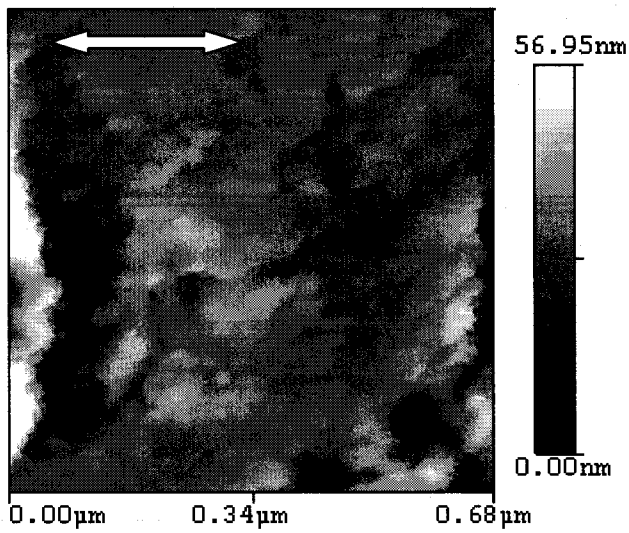

Figure 7.33: Nanometer length scale wear of boronized tantalum.

The results obtained show that simulated body fluid has a strong effect on wear mechanisms of different coatings. Future study is recommended on this subject, as summarized in Chapter 9 of this dissertation.

7.5 References

1 H. P. Jost, "Tribology – the past, the present and the future" 10th International Colloquium 1996.

2 H. Matsuno, A. Yokoyama, F. Watari, M. Uo, T. Kawasaki, "Biocompatibility and osteogenesis of refractory metal implants, titanium, hafnium, niobium tantalum and rhenium" Biomaterials 22 2001 p1253-1262.

3 K. G. Anthymidis, N. Maragoudakis, G. Stergioudis, O. Haidar, D. N. Tsipas, "A comparative study of boride coatings obtained by pack cementation method and by fluidized bed technology" Materials Letters 57 (16-17) 2003 p2399-2403.

4 C. H. Xu, W. Gao, Y.-L Yang, "Superplastic boronizing of a low alloy steel - microstructural aspects" Journal of Materials Processing Technology 108(3) 2001 p349-355.

5 G. Palombarini, G. Sambogna, M. Carbucicchio, "Role of oxygen in iron boriding using boron carbide" Journal of Materials Science Letters 12(10) 1993 p741-742.

6 G. Palombarini, M. Carbucicchio, "Growth of boride coatings on iron" Journal of Materials Science Letters 6(4) 1987 p415-16.

7 R. Qunli, W. Haowei, F. Xiaolan, Z. Yaohe, "AFM analysis on the surface of electroless Ni-B coating" Xiyou Jinshu Cailiao Yu Gongcheng 32(6) 2003 p420-423.

8 I. Ozebek, H. Akbkulut, S. Zeytin, C. Bindal, A. Hikmet Ucisik, "The characterization of borided 99.5% purity nickel" Surface & Coatings Technology 126 2000 p166-170.

9 A. Erdemir, C. Bindal, "Formation and self-lubricating mechanisms of boric acid on borided steel surfaces" Surface & Coatings Technology, 76-77, 1995 p443-449.

10 C. Bindal, A. Erdemir, "Ultralow friction behavior of borided steel surface after flash annealing" Applied Physics Letters 68 7 1996 p923.

11 S. Mirmiran, V. Tsukruk, A. Erdemir, "Nano-tribilogical and wear behavior of boric acid solid lubricant" Tribology Transactions 42(1) 1999 p180-185.

12 A. Erdemir, C. Bindal, C. Zuiker, E. Savrun, "Tribology of naturally occurring boric acid films on boron carbide" Surface & Coatings Technology 86-87 1996 p507.

13 A. Erdemir, C. Bindal, G. R. Fenske, "Formation of ultralow friction surface films on boron carbide" Applied Physics Letters 68(12) 1996 p1637-1639.

14 C. Martini, G. Palombarini, G. Poli, D. Prandstraller, "Sliding and abrasive wear behaviour of boride coatings" Wear 256(6) 2004 p608-613.

15 D. A. Rigney, P. G. Shewmon, "Wear and Erosion of Metals" Review Paper as Part of Treatise Set, U. S. Delegation to China, Nov., 1981, ASM/AIME/CSM, The Metallurgical Society of AIME, Warrendale, Pa., 1981.

16 J. Wang, P. Layrolle, M. Stigter, K. de Groot, "Biomimetic and electrolytic calcium phosphate coatings on titanium alloy: physicochemical characteristics and cell attachment" Biomaterials, 25 4 2004 p583-592.

17 B. Shi, "Tribological Comparison of Materials" Ph.D. Dissertation, University of Alaska, Fairbanks, USA, 2005.

Chapter 8

Conclusions

This research focused on three areas of investigation: wear mechanisms of surface coatings (boride), friction-induced phase transformation, and nanotribology using an atomic force microscope (AFM). New wear modes at different length scales were proposed. Stress-induced phase transformation and material hardening were discovered. The applications of this research lie in the biological arena, involving artificial joints.

An experimental investigation was successful in detecting amorphous debris through friction-induced phase transformations in boronized chromium. It showed that sliding could be a controlled process to effectively generate the amorphous phases. The amorphous debris formed is not desirable for artificial joints applications. This study provides a useful basis for biomaterials design and processing.

Boronized tantalum surfaces revealed changing friction during sliding. Different phases were found after sliding that caused the friction change.

After severe sliding of an Al-Cu system, the sample went through different phase transformations, and part of it formed amorphous alumina. A new sliding model was proposed to explain this behavior. An AFM study of the surface modification and material transfer on the Cu surface during sliding showed different frictional behavior.

During sliding of Cu on Cu, a friction variation on the surface was observed in the friction force microscope (FFM) image. The complex surface and subsurface deformation were responsible for this friction variation. It is observed that the FFM is a powerful tool to study the surface friction from the micrometer length scale to the atomic length scale.

The boronized refractory metals showed different friction behavior in dry conditions and in simulated body fluid. Their wear mechanisms were different at the micrometer length scale and the nanometer length scale. Wear mechanisms at the nanometer length scale provided the explanation for different modes of formation of debris.

Based on this study, it is quite evident that if the surface roughness of boronized tungsten could be reduced, it will have potential as an implant material. Boronized tungsten showed the lowest coefficient of friction and unchanged wear mechanisms in simulated body fluid at micrometer and nanometer length scales.

Although the coefficients of friction in wet tests were lower than those in dry conditions, other boronized materials (NbB, TaB) showed deteriorating wear in simulated body fluid at a nanometer length scale. For practical use, the wear resistance should be further increased.

In surface characterization of indented surfaces, it was the first time the friction force microscope was used to investigate severely deformed ductile materials.

Chapter 9

Scope of Future Work

The main focus of this research was the topological study of sliding surfaces. Several new phenomena were discovered; and new mechanisms were proposed. This research opened new windows for exploration and areas of future investigation.

Amorphous debris was found in two sliding systems with boride coatings. The generation of amorphous particles is of great interest in nanomaterials research. In order to have wide commercial applications, including biological applications, future tribochemical investigation is recommended.

The utilization of the friction force microscope revealed a new theory of materials hardening under indents. The chemical analysis of the frictional fringes formed on the Cu surface during severe sliding of Al-Cu would be a powerful approach to gain an understanding of engineering materials.

Utilization of an atomic force microscope to study wear mechanisms at different length scales brings a completely new view of tribomaterials.

Simulated body fluid significantly affected the tribological performance of the investigated materials. Future investigation of tribochemical properties and lubrication behavior is recommended.

In the study of frictional properties on an indent of ductile materials, friction associated with surface modification, materials hardening, and plastic flow were reported for the first time using a friction force microscope. Future investigation is recommended to study the cross section and subsurface using a high-resolution transmission electron microscope (HR TEM). In such a study, atomistic behavior could be linked to surface bulk materials.